

AN INVESTIGATION OF THE THREE-BODY REACTION
 $\text{He}^3(\text{He}^3, 2p)\text{He}^4$

Thesis by
Andrew Dow Bacher

In Partial Fulfillment of the Requirements
For the Degree of
Doctor of Philosophy

California Institute of Technology
Pasadena, California
1967
(Submitted December 2 , 1966)

ACKNOWLEDGMENTS

It is a sincere pleasure for the author to acknowledge his gratitude to the faculty, staff and students of the Kellogg Radiation Laboratory, who have made this work a unique and fruitful experience. I am grateful to Professor William A. Fowler whose lectures aroused my curiosity about this reaction and who has given the work his continued support and encouragement; to Professor W. Whaling who introduced me to experimental work in Kellogg; and to Professors T. Lauritsen, C. A. Barnes and R. W. Kavanagh for their suggestions and interest.

I am particularly indebted to Professor T. A. Tombrello, both for his active participation and guidance in all phases of this work and for the spirited and exciting qualities that have characterized this and our other mutual efforts.

The author is grateful to Mr. Robert J. Spiger for his assistance in many phases of the experimental work and for his noteworthy industry. In addition, I wish to thank M. R. Dwarakanath for his help with the experimental runs, Dr. P. D. Parker for his aid in the early phases of this project, Dr. P. A. Seeger and Mrs. Barbara Zimmerman for their assistance with computing techniques, and D. Papanastassiou, G. Godfrey, R. Moore and M. Cooper for their aid with data reduction.

Last, but foremost, I am grateful to my wife, Fran, for her patience and confidence and to my parents who are a continual source of inspiration and encouragement.

The author acknowledges the financial support of the National Science Foundation and the California Institute of Technology in the form of fellowships, assistantships and tuition scholarships. The research project has been supported by the Office of Naval Research.

ABSTRACT

Reactions produced by the He^3 bombardment of He^3 have been investigated for bombarding energies from 1 to 20 MeV using a tandem Van de Graaff accelerator. Proton spectra from the three-body reaction $\text{He}^3(\text{He}^3, 2\text{p})\text{He}^4$ have been measured with a counter telescope at 13 angles for 9 bombarding energies between 3 and 18 MeV. The results are compared with a model for the reaction which includes a strong p- He^4 final-state interaction. Alpha-particle spectra have been obtained at 12 and 18 MeV for forward angles with a magnetic spectrometer. These spectra indicate a strongly forward-peaked mechanism involving the $^1\text{S}_0$ p-p interaction in addition to the p- He^4 interaction. Measurements of p- He^4 and p-p coincidence spectra at 10 MeV confirm these features of the reaction mechanism. Deuteron spectra from the reaction $\text{He}^3(\text{He}^3, \text{d})\text{pHe}^3$ have been measured at 18 MeV. A triton spectrum from the reaction $\text{He}^3(\text{He}^3, \text{t})3\text{p}$ at 20 MeV and 4^0 is interpreted in terms of a sequential decay through an excited state of the alpha particle at 20.0 MeV. No effects are observed which would indicate an interaction in the residual (3p) system. Below 3 MeV the $\text{He}^3(\text{He}^3, 2\text{p})\text{He}^4$ reaction mechanism is observed to be changing and further measurements are suggested in view of the importance of this reaction in stellar interiors.

TABLE OF CONTENTS

<u>PART</u>	<u>TITLE</u>	<u>PAGE</u>
I.	INTRODUCTION	1
II.	EXPERIMENTAL APPARATUS	5
	A. He ³ Beams	5
	B. Gas Scattering Chamber	6
	1. The Gas Target	6
	2. Particle Detection	9
	3. High Pressure Gas Cell	14
	4. Measurement of Absolute Cross Sections	16
	C. Gas Target for the 61-cm Magnetic Spectrometer	20
III.	PROTON SPECTRA	23
	A. Experimental Procedure and Results	23
	B. Final-State Enhancements	26
	C. Li ⁵ Ground State Model	30
	1. Spectrum Calculation	30
	2. Comparison with Experimental Spectra	33
	3. Angular Distributions	39
	D. Cross Section Determinations	41
	1. Li ⁵ Ground State Model	41
	2. Integrated Charge 1 Measurements	42
	3. Comparison of Cross Sections	44
IV.	MAGNETIC SPECTROMETER MEASUREMENTS	46
	A. Experimental Procedure	46
	B. Alpha-Particle Spectra at 12 and 18 MeV	47
	C. Deuteron Spectra at 18 MeV	53
	D. Triton Spectrum at 20 MeV	54

<u>PART</u>	<u>TITLE</u>	<u>PAGE</u>
V.	COINCIDENCE MEASUREMENTS	57
	A. Experimental Procedure	57
	B. Summary of Results at 10 MeV	59
VI.	LOW ENERGY MEASUREMENTS	61
	A. Experimental Procedure and Results	61
	B. Astrophysical Significance	63
VII.	DISCUSSION OF RESULTS	66
APPENDIX A.	SPECTRUM CALCULATIONS FOR MULTI- PARTICLE FINAL STATES	71
	1. Phase-Space Distributions	71
	2. Spectrum of the Non-Interacting Particle	75
	3. Recoil Breakup Spectrum in Sequential Reactions	78
REFERENCES		83
TABLES		87
FIGURES		95

I. INTRODUCTION

The fact that particles in the final state of a nuclear reaction may interact with one another to strongly modify the observed spectra has been long established. In nuclear physics this was first apparent in beta decay where the Coulomb interaction distorts the spectra of electrons and positrons from that expected on the basis of simple phase-space arguments. More recently, it has been recognized that the effects of strong final-state interactions can be used to investigate certain aspects of the intermediate state. As a result, the study of nuclear reactions leading to final states consisting of more than two particles has attracted considerable interest (see, for example, the proceedings of the 1964 APS Topical Conference on "Correlations of Particles Emitted in Nuclear Reactions", Goodman, 1965). As a tool for nuclear spectroscopy, reactions with more than two particles in the final state might be used to study the production or decay properties of particle-unstable nuclear states that are inaccessible to a two-body scattering experiment. Alternatively, given quantitative information about the two-body interactions that are present, this type of reaction might be used to investigate a model for the reaction mechanism. Such a model would be subject to direct experimental test through predictions of the effects of these two-body interactions on the angle and energy distributions of particles in the final state.

The present work describes an investigation of the multi-particle final states produced by the He^3 bombardment of He^3 . Its motivations have been twofold: to study the nature of the reaction mechanism for a particularly simple final state over a wide range of bombarding energy and to investigate the use of a model for the

reaction mechanism in determining the total reaction cross section. The existence of such a model would simplify measurements of the cross section at very low bombarding energies where its value is of considerable astrophysical importance.

Below a He^3 bombarding energy of 20 MeV the following final states become available.

Final State	Q-Value (MeV)	Threshold (MeV)
$\text{He}^4 + 2p$	+12.860	none
$\text{He}^3 + d + p$	- 5.49	10.98
$t + 3p$	- 6.95	13.90
$\text{He}^3 + n + 2p$	- 7.72	15.44

This information is summarized in Figure 1 where the relevant structure in Li^5 and in the compound nucleus Be^6 is also indicated. Below 11 MeV the reaction is characterized by a single reaction channel leading to a final state of an alpha particle and two protons. With the development of the tandem Van de Graaff accelerator it has become possible to investigate the nature of this reaction mechanism with high resolution over a wide range of bombarding energies. This range covers the region with the single reaction channel and extends above it into an energy range in which new reaction channels open and additional two-particle interactions are expected to become important.

At the opposite extreme of very low bombarding energies, the total cross section for the $\text{He}^3(\text{He}^3, 2p)\text{He}^4$ reaction is of astrophysical interest, since it represents one of the ways of

terminating the proton-proton chain in stars (C. C. Lauritsen - as quoted by Fowler, 1951 - and Schatzman, 1951). This reaction is the only practical way to get to He^4 from pure H^1 and in the presence of He^4 it competes with the reaction $\text{He}^3(\alpha, \gamma)\text{Be}^7$ in determining the path of completion for the p-p chain (Parker, 1963 and Parker et al., 1964). The value of the cross section at energies relevant in stellar interiors is important in determining energy generation rates, in establishing the distribution of He^3 in a stellar model and in determining the solar high energy neutrino flux.

Previous work on the $\text{He}^3(\text{He}^3, 2\text{p})\text{He}^4$ reaction below 20 MeV was concerned with total cross section measurements between 100 keV and 800 keV (Good et al., 1954). Uncertainties in the extrapolation of these results to low energy (see Figure 49) led to the present interest in extending total cross section measurements to low bombarding energies. Concurrent with reports of the present work (Bacher, 1963, Tombrello and Bacher, 1965 and Bacher and Tombrello, 1965a) there have been observations of p-p and p- He^4 coincidence spectra at 5 MeV (Aldridge et al., 1965) and 15 MeV (Zurmühle, 1965) and p-p coincidence spectra at 1 MeV and 5 MeV (Blackmore and Warren, 1966) which have indicated the presence of p- He^4 and p-p final state interactions.

The present work includes a systematic study of the nature of the reaction mechanism from below 1 MeV up to 20 MeV in an effort to obtain a more consistent picture of its dependence on the interactions of various pairs of particles in the final state. In Part II the experimental apparatus is described.

Part III describes the measurements of single-counter proton spectra for bombarding energies from 3 to 18 MeV and their comparison with a model for the reaction based on a strong p- He^4

final-state interaction. Measurements of alpha-particle, deuteron and triton spectra at forward angles with a double-focusing magnetic spectrometer are presented in Part IV. In Part V the results of p-He⁴ and p-p coincidence measurements at 10 MeV are given and in Part VI measurements of the 90° energy spectra down to 0.28 MeV are described. A summary and discussion of these results is presented in Part VII and an appendix describes spectrum calculations for multi-particle final states.

II. EXPERIMENTAL APPARATUS

A. He³ Beams

The He³ beams used in the course of this investigation covered the energy range from 1 to 20 MeV and were obtained from the ONR-CIT tandem Van de Graaff accelerator. Beams with an energy up to 12 MeV were produced with the standard JN injector system (Rose *et al.*, 1961). Singly charged helium ions are pre-accelerated to an energy of 500 to 900 keV, neutralized on passing through a helium exchange canal, and then ionized at the center of the high voltage terminal to produce singly and doubly charged particle beams. The energy of the appropriate charge state (singly charged for energies below 6 MeV) was determined by analysis with a 90° uniform field magnet. Analyzed He³ beam currents varied from 1.0 to 1.5 μa for the singly charged beam and from 0.5 to 1.0 μa for the doubly charged beam. Variations in the beam current depended mainly on the ion source condition and alignment, the accelerator vacuum conditions, and the transmission characteristics of the accelerator for different terminal voltages. The beam intensities measured in the gas scattering chamber were considerably lower than the above figures due to scattering of the beam by the thin entrance foil and the severe beam collimation requirements for the gas target (see Section B). Target beam currents varied from 0.06 μa at 3 MeV to 0.16 μa at 12 MeV.

He³ beams in the energy range from 12 to 20 MeV were obtained by injecting into the tandem accelerator the low intensity 80-90 keV negative helium ion output of the duo-plasmatron negative ion source. This negative beam is accelerated to the central

terminal where a substantial fraction of it is stripped of three electrons, producing a doubly charged helium beam with an energy corresponding to three times the potential difference between the accelerator terminal and ground. Under normal operating conditions a negative helium beam of $0.060 \mu\text{a}$ was injected. This resulted in an analyzed beam of doubly charged helium varying from a maximum of $0.025 \mu\text{a}$ at 12 MeV to a minimum of $0.008 \mu\text{a}$ at 18 MeV. Target beam currents for the experimental runs were typically 0.004 to $0.008 \mu\text{a}$. For the experimental runs using the gas target in the 61-cm magnetic spectrometer these conditions were somewhat improved. From an injected beam of $0.100 \mu\text{a}$ a target beam current of $0.030 \mu\text{a}$ was obtained at a He^3 beam energy of 20 MeV.

B. Gas Scattering Chamber

1. The Gas Target

The problem of maintaining a gas target of accurately known thickness that is accessible to a beam of well-defined energy has yielded to several experimental approaches. In one, the beam is introduced into the target through a series of differentially pumped apertures which both collimate the beam and maintain a pressure gradient between the gas target and the high vacuum of the beam pipe. Alternatively, the beam may enter the target chamber through a thin foil which isolates the gas target from the high vacuum region. The first method is inherently more precise since the use of an entrance foil introduces energy straggling and scattering effects in the definition of the incident beam. In a differentially pumped chamber the resulting gas flow can be

accurately compensated by an automatic pressure regulator, thus maintaining a constant target thickness. However, if the supply of target gas is limited, recirculation and purification techniques are required to minimize gas losses and contamination. Practical considerations, such as the expense of high speed pumping facilities and the cost of an adequate supply of high purity target gas, often make the second approach of foil containment more attractive, particularly in a range of bombarding energies where the choice of a thin entrance window can reduce the effects of the foil on the beam.

In the present work the high cost of He^3 (\$150/liter STP at the time of the experiment) and the availability of existing apparatus decided the issue in favor of foil containment. A majority of the experimental results was obtained using, as basic equipment, the 30-cm gas scattering chamber designed and constructed by Lionel Senhouse. This equipment has been described in detail elsewhere (Tombrello and Senhouse, 1963; Senhouse, 1964) and only the pertinent features of its operation will be reviewed.

Figure 2 shows the basic target configuration. The thin entrance foil is followed by a beam collimator consisting of two defining slits (1.3 mm in diameter and spaced 17.5 cm apart) and three anti-scattering slits (1.6 mm in diameter). After passing through the exit foil, the beam is collected in an insulated Faraday cup (angular acceptance $\pm 2^\circ$) that is connected directly to the high vacuum side of the chamber. Collimation of the beam after the entrance foil helps to reduce spreading of the beam in the gas target and thereby insures a good geometry experiment over a wide range of bombarding energies. The disadvantages are the sharp decrease in beam current at the low bombarding energies and the limit placed

on the maximum forward detector angle by the protrusion of the collimator into the chamber.

Nickel foils (obtained commercially from Chromium Corporation of America, Waterbury, Connecticut) were employed for both the entrance and exit windows of the gas target. The entrance window consisted of a $1000\text{-}\overset{\circ}{\text{A}}$ nickel foil mounted with epoxy cement over a smoothly beveled $1/8$ " diameter aperture to allow the foil to deform slightly under the pressure of the target gas. The exit window, $6250\text{-}\overset{\circ}{\text{A}}$ in thickness, was mounted in a similar fashion over a $1/2$ " diameter hole leading to the Faraday cup. To assure a constant target pressure considerable care was taken to select hole-free windows. The $6250\text{-}\overset{\circ}{\text{A}}$ nickel was supplied in the form of self-supporting foils and hole-free regions could be selected before mounting. The $1000\text{-}\overset{\circ}{\text{A}}$ foils, which were electroplated on a thin copper backing, had to be mounted and the copper etched off before inspection. The success rate of $\sim 5\%$ for hole-free foils appeared to be limited predominately by production techniques of the manufacturer.

The He^3 target gas (Mound Laboratory, Miamisburg, Ohio) was supplied with an analyzed purity of 99.36%. The principle contaminant consisted of 0.43% He^4 with the remaining 0.21% being divided approximately equally among hydrogen, water, and nitrogen. The effect of these latter contaminants was held to a minimum with an activated charcoal trap that was cooled to liquid nitrogen temperatures. The absolute gas pressure was measured with an oil manometer that was connected between the target chamber and high vacuum and was filled with n-butyl sebacate (density 0.927 ± 0.003 g/ml). Readings were made with a cathetometer to ± 0.015 cm for typical target pressures between 20 and 40 cm of oil ($1/50$ to $1/25$

atm). The temperature of the gas was monitored by measuring the temperature of the target chamber to $\pm 0.05^{\circ}\text{C}$ with a mercury thermometer.

To insure accurate beam collection the Faraday cup was provided with both electric and magnetic suppression of electrons produced by the beam at the collimating slits and the exit foil. A standard electrostatic suppression ring was held at -200 V and a small annular permanent magnet provided magnetic suppression. The insulated cup was held slightly positive ($+67\frac{1}{2}\text{ V}$) to prevent loss of electrons produced on stopping the beam. The beam current was integrated with an Eldorado model CI-110 current integrator that was calibrated for each run with a precision current source. The overall accuracy of the beam integration was dependent mainly on the stability of the integrator electronics. Since the reproducibility in the calibrations was better than 0.3% , a conservative error of 0.5% was assigned to this measurement.

2. Particle Detection

In a gas target scattering and reactions occur at every point along the path defined by the beam in the chamber. As a result the particle detector must be accompanied by a pair of collimating slits which accurately define the length of beam, and hence the target thickness, seen by the detector. A third anti-scattering slit is usually included to minimize the detection of particles scattered from the walls of the target chamber and from the inside surfaces of the collimator assembly. The precision with which this detector collimator is constructed and aligned is of primary importance in determining the accuracy of experimental

measurements. The geometrical configuration is indicated in Figure 5.

The "G factor", which is the product of the target thickness observed and the detector solid angle, has been calculated to fourth order by Silverstein (1959), including effects due to finite beam size and the variation of the cross section over the angular range of the collimator. Ignoring the last two effects which are small for the purposes of the present experiment, this factor is given to second order in the slit parameters by

$$G = \frac{4b_1 b_2 \ell}{R_0 h \sin \theta} \left(1 + \frac{b_2^2}{3R_0^2} \cot^2 \theta - \frac{b_1^2 + b_2^2}{2h^2} - \frac{\ell^2}{8R_0^2} \right),$$

where (see Figure 5)

$2b_1$ = width of front slit,

$2b_2$ = width of rear slit,

ℓ = height of rear slit,

h = separation of the two slits,

R_0 = distance from rear slit to axis of rotation,

θ = laboratory angle with respect to the beam.

In the design of the detector collimator for this experiment, the parameters were chosen to minimize the effects of the second-order terms in the above expression. For convenience,

the widths of the front and rear slits were chosen to be nominally equal. The results of measurements of these parameters for several collimators are presented in Table I. They show that the maximum correction due to the second order terms is less than the cumulative error in determining the first order value

$$G_0 = \frac{4b_1 b_2 \ell}{R_0 h} .$$

The extreme angles seen when the detector is set at an angle θ are given by

$$\theta_{\pm} = \theta \pm \tan^{-1} (2b/h) ,$$

where $2b$ is the mean width of the front and rear slits. For these extreme angles the detector has zero detection efficiency. A more convenient description is in terms of the beam length for various reaction angles $\bar{\theta}$ (close to θ) observed by the detector at a fixed angle θ . This is a maximum for $\bar{\theta}$ equal to θ , but its behavior for values differing from θ is unsymmetric if θ is not 90° (see Figure 5b). This indicates how at forward angles the collimator geometry tends to weight angles more forward than θ slightly. This tendency is exactly reversed for the backward angles. The full width at half maximum gives a reasonable value for the angular resolution of the collimator and this is, typically,

$$\theta_{1/2} = 2 \tan^{-1} (b/h) .$$

A detailed view of the detector collimator built for use with the counter telescope is shown in Figure 2, positioned at 0° . Because of the high energy of the protons produced in this reaction (22 MeV at 20° for a bombarding energy of 12 MeV) slits of 0.040" thick brass, capable of stopping 22 MeV protons, were required to define the observed beam length. The vertical slits were cut using a slitting saw with the brass blank positioned in a dividing head. Following the first cut the piece was rotated by 180° and recut, giving an accurately centered slit of the desired width. Steel inserts were ground to a thickness of 0.040" and cut with a slitting saw. The edges were then precision ground and the horizontal slit was defined by press fitting these inserts into the vertical slit body, using a jig to determine the proper slit spacing.

The slit dimensions were then accurately measured with a traveling microscope. The slits were clamped in the collimator body in the proper relative orientation and the collimator was optically aligned with respect to its axis of rotation (the center of the chamber) and the beam collimator. With these precautions the detector angles could be determined reproducibly to an accuracy of better than $\pm 0.1^\circ$. The same techniques of fabrication and alignment were used when a second collimator, attached to the lucite center of the chamber top (see Figure 3), was added for coincidence investigations. Both collimators had an angular resolution (fwhm) of $\theta_{1/2} = 3.6^\circ$ and could reach a forward angle of 12° . The large angular acceptance was dictated by the small cross section of the $\text{He}^3(\text{He}^3, 2p)\text{He}^4$ reaction and the low gas target pressures required by the choice of a thin entrance foil. The parameters for these collimators and their associated errors are summarized in Table I.

The first attempts of this investigation were limited by problems associated with the detection of protons with energies in excess of 20 MeV. Since their range corresponds to about 3 mm in silicon, the possibility of using a standard surface-barrier counter was virtually eliminated. The first results were obtained with a CsI(Tl) crystal mounted on a phototube face and fixed at a laboratory angle of 90° . Later measurements used a 1 mm deep counter tilted to a 30° angle to double its thickness. By late 1963 lithium-drifted silicon detectors with depletion depths of 3 mm or more were available commercially (Technical Measurement Corporation, Mountain View, California). Concurrent with this development of thick solid state detectors was the gradual improvement in resolution and uniformity of very thin transmission detectors ($< 50 \mu$). These counters could be employed for particle identification since particles that are not stopped in the counter produce a pulse roughly proportional to dE/dx for that particle.

For the results presented here a counter telescope was used that contained a 48μ surface-barrier transmission counter followed by a 3 mm thick lithium-drifted silicon detector. Since the types of scattered and reaction particles in this work were limited to protons, elastically scattered He^3 's and alpha particles; the telescope was able to separate protons ($Z = 1$) from the remaining particles ($Z = 2$) down to an energy corresponding to the thickness of the thin counter to protons. For the 48μ counter this limit was 2.1 MeV. The work at bombarding energies in excess of 12 MeV required the use of a 5 mm deep detector to stop the energetic protons at the most forward angles. A schematic diagram of the electronics associated with the counter telescope is given in Figure 6.

For a large portion of the work the detectors in the counter telescope were operated successfully in the He^3 target gas despite the rather substantial amount of ionization produced by the beam, particularly at low bombarding energies. Since the thick counter required a bias of 300 to 400 V to assure rapid charge collection of the electron-hole pairs, careful shielding of the counter lead was important to prevent breakdown in the gas. This was eventually achieved by sealing the Microdot connectors with small O-rings.

3. High Pressure Gas Cell

The portions of this investigation that required use of the negative helium beam or the detection of two of the three final-state particles in coincidence suffered from a sharp reduction in counting rate. This loss was partially balanced by confining the gas target to a small cell at the center of the chamber, in which considerably higher target pressures could be maintained. One of these configurations is shown in Figure 3a. In this case slots $3/8''$ in height were cut in the cell wall as indicated. These openings were covered with 0.1 mil (2.26 mg/cm^2) Havar foil and were positioned to allow the beam to pass through the cell and the reaction particles to escape from it at the angles of interest. Part b of Figure 3 shows the collimator that was positioned in the top of the chamber to allow coincidence measurements to be made.

For the coincidence work and the proton spectra at 13.81 and 15.55 MeV the gas cell was operated at a nominal pressure of $1/2$ atm, as indicated on a 4" Marshalltown gauge. This position could be reproduced accurately and was later calibrated to $\pm 0.5\%$

with a mercury manometer. For the proton spectra at 18 MeV the target pressure was nominally 150 mm (1/5 atm) and was monitored continuously by an aneroid gauge (Wallace and Tiernan Inc., Belleville, New Jersey) with an accuracy of ± 0.5 mm. In all cases the entrance window in front of the beam collimator was removed and the rest of the target chamber, including the detection apparatus, was maintained at high vacuum.

Accurate integration of the small beam required considerable care. For the proton spectra at 13.81 and 15.55 MeV the Eldorado model CI-110 current integrator was employed. The internal integrator leakage current which had been carefully minimized, was recorded before and after each integration (\sim every 15 minutes). This leakage current for each run was then taken into account in the calibration, giving an overall accuracy in the beam current integration of $\pm 1.5\%$. For the angular distribution at 18 MeV a high precision current integrator, accurate to $\pm 0.2\%$ was used. This equipment was based on that described by Rodgers (1963) and was constructed for use with small beam currents by M. Dwarakanath.

As a result of the high gas pressure and thick entrance and exit windows, various effects which increase the experimental uncertainty of the measurements were enhanced. Corrections were made for the distortion of the spectral shapes due to energy loss in the foils and the gas, using the proton stopping cross section curves of Whaling (1958) and Demirlioglu and Whaling (1962). The scattering of the beam out of the Faraday cup aperture was small (see Section 4) but was corrected for by normalizing the yield of elastically scattered He^3 's to more accurate measurements (Bacher and Tombrello, 1965). The effects of foil and wall scattering in the

smaller cell were considerably enhanced but were confined to the elastically scattered particles ($Z = 2$) which could be separated from the proton spectra by particle identification with the counter telescope.

4. Measurement of Absolute Cross Sections

As one aim of this investigation involves developing a consistent method for determining the total cross section for the reaction $\text{He}^3(\text{He}^3, 2\text{p})\text{He}^4$, it is important to consider the magnitude of the systematic errors involved in the determination of the experimental yield, prior to its interpretation in terms of any particular model. For a gas target the yield for a particular particle in the final state as a function of laboratory angle θ and the particle energy E is given by

$$Y(E, \theta) = \epsilon \cdot N_b \cdot N_t \cdot \left(\frac{d^2\sigma}{dE d\Omega} \right)_{av} \cdot \Delta\Omega \cdot \Delta E$$

where

- ϵ = the particle detection efficiency,
- N_b = the number of incident particles,
- N_t = the number of target nuclei per cm^3 ,
- $\left(\frac{d^2\sigma}{dE d\Omega} \right)_{av}$ = the differential cross section per unit energy averaged over the energy and angular resolution factors for the experimental configuration,

$\lambda\Delta\Omega$ = the target thickness times the solid angle,

and ΔE = the energy resolution of the multichannel analyzer.

The energy of the bombarding particles was determined by analysis with a 34-inch radius 90° uniform field magnet, the defining slits of which were placed at the conjugate focal points of the magnet (Pearson, 1963). For this configuration the fractional uncertainty in the beam energy is

$$\frac{\Delta E}{E} = \frac{S_1 + S_2}{2R}$$

which, with typical full slit widths S_1 and S_2 of 0.150", gives

$$\frac{\Delta E}{E} = 0.44\% .$$

The experimental uncertainty in the energy represents an improvement over this limit for several reasons. The process of maximizing the beam current tends to select a particular reproducible path through the analyzing magnet. In addition, under normal operating conditions the beam profile is such that a large fraction of the beam is confined to a width considerably less than that of the defining slits. The energy quoted for each measurement refers to the beam energy at the center of the gas target after correcting for energy loss in the entrance foil and the target gas. For all of the angular distributions the uncertainty in this quantity is better than 0.3%. This includes the data taken with the high pressure gas cell with thicker entrance and exit windows and it also includes a possible

error in the thickness of the nickel foils of $\pm 20\%$ (Parker, 1963 and direct measurements of foil thicknesses).

For a solid state detector the efficiency is usually taken to be unity. This continues to hold for a counter telescope, provided the active areas of the counters are defined so that particles multiply - scattered on passing through the front counter are stopped in an active region of the rear counter. The importance of geometrical factors for a gas target has been emphasized in a previous section and the results of measurements are presented in Table I. The cumulative error in G is 0.23%. Angle-dependent effects which have not been included are the second order corrections to G (maximum error 0.22%) and the uncertainty of $\pm 0.1^\circ$ in the laboratory angle (the maximum error in $\sin\theta$ is 0.7% at 15°). Corrections arising from the finite size of the beam and the variation of the cross section with angle can each produce a maximum error of only 0.05%.

The errors associated with beam collection, integration, and the determination of the number of incident particles have been discussed previously and range from a typical value of 0.5% to 1.5% for some of the results obtained with the negative helium beam. In several instances the accuracy of the beam integration was verified with a fixed monitor counter determining the number of elastically scattered He^3 particles. The results at low bombarding energies were corrected for the equilibrium fraction of singly charged He^3 in the integrated beam current.

The determination of the number of target nuclei per cubic centimeter depends on measurements of the gas target pressure and temperature. In those cases where a charcoal trap cooled to liquid nitrogen temperatures was used to remove

contaminants, a correction amounting to about 1% was made to allow for a gradual pressure change due to the slight adsorption of helium by the cooled charcoal. The temperature of the gas was measured by assuming it to be in equilibrium with the target chamber. Effects due to localized heating of the gas by the beam (Robertson et al., 1961) are expected to be small for such low beam currents in the target.

The chance that a significant amount of the He^3 beam might be scattered out of the angular aperture of the Faraday cup ($\pm 2^\circ$) by the target gas is small as may be seen from the root-mean-square scattering angle for a typical target pressure;

$$\langle \theta_{\text{He}^3}^2 \rangle^{1/2} = 0.9^\circ / E_{\text{He}^3} \text{ (MeV)} .$$

In addition, any effects due to multiple scattering of the beam at the forward angles are expected to be small even in the high pressure gas cells because of the small cross section for the reaction. Scattering of the reaction products on passing out of these cells is also small. For the 0.1 mil Havar foil the rms scattering angle is given by

$$\langle \theta_p^2 \rangle^{1/2} = 5.2^\circ / E_p \text{ (MeV)} \quad \text{for protons}$$

and

$$\langle \theta_\alpha^2 \rangle^{1/2} = 10.5^\circ / E_\alpha \text{ (MeV)} \quad \text{for alpha particles,}$$

while the angular resolution of the detector collimators was $\pm 1.8^\circ$. A summary of the systematic errors is presented in Table II.

C. Gas Target for the 61-cm Magnetic Spectrometer

In order to investigate in detail the spectral shape of alpha particles from the $\text{He}^3(\text{He}^3, 2p)\text{He}^4$ reaction, as well as deuterons and tritons from final states available at the higher He^3 bombarding energies, a gas target (designed by T. A. Tombrello) was positioned in the target chamber of the 61-cm magnetic spectrometer. A side view of this apparatus is presented in Figure 4. The target gas is contained in a 3 1/2" diameter brass can that is centered in the spectrometer target chamber with a lucite top. On rotation, this chamber remains fixed with respect to the spectrometer.

A 1/4" slot, cut through an angular range of 160° and covered with a 0.1 mil Havar foil, serves as an entrance window for the beam. The exit window leading to the spectrometer is provided by a 1/2" diameter hole which centers a small collimator with a 1/16" vertical front slit. This hole is sealed with a foil holder which also serves as an anti-scattering slit. The exit window normally consisted of a 10,000- \AA nickel foil. The rear slits of this collimator are defined by the variable entrance slits of the spectrometer, located 14.5" from the center of the target chamber. The proper alignment of the gas chamber with respect to the spectrometer was established optically prior to each experimental run. With the magnet set at 90° , an optical axis was defined by the beam entrance hole and the center of the 90° port in the spectrometer target chamber. The gas target was then positioned in the spectrometer chamber with a reference line on the target cell located exactly 90° from the exit slit. This alignment procedure was found to be

reproducible to $\pm 0.1^\circ$, the precision with which the spectrometer angle can be set.

The lucite top of the gas cell contained connections to a cold trap for the target gas and a gas manifold with provision for several target gases. Contaminants in the gas (with the exception of 0.43% He^4) were held to a minimum with an activated charcoal cold trap maintained at liquid nitrogen temperatures. The target pressure, as read on a 2" Marshalltown gauge, was nominally 1/5 atm and could be held constant to better than $\pm 3\%$ by frequent filling of the cold trap dewar. Integration of the beam current was provided by stopping the beam in the insulated gas cell (held at +300 V) and integrating the resulting current with the Eldorado current integrator. While only a relative consistency between points in the spectrometer scan was required to study the shapes of the alpha particle spectra, an absolute scale (good to $\sim 20\%$) was provided for the measurements at 12 MeV by scanning the elastic He^3 peak at 15° under similar conditions and normalizing the results to the known elastic cross sections (Tombrello and Bacher, 1963).

The alpha particles were detected with the 16-counter array of surface-barrier detectors positioned along the focal plane of the spectrometer, and their energy was determined by field measurements with a nuclear magnetic resonance probe. Alpha particles were separated from protons of the same energy over the range 7 to 20 MeV by varying the counter bias so that the protons were never fully stopped in the active volume of the counter. The counts from each detector were corrected for their different effective solid angles with correction factors determined by requiring agreement with a previously determined shape in the scan

across a thick target yield spectrum (Cocke, 1965). A limit was placed on the variation of these factors due to the extended nature of the source in a gas target. With the magnet at a fixed frequency, the width of the entrance slit of the magnet (and hence the length of target seen in the gas cell) was varied by a factor of 4. The number of counts observed in each counter scaled appropriately within the statistical errors ($\sim 5\%$). Measurements were made with the center detector of the counter array for magnetic field settings below that of the scattered beam to avoid routing problems associated with high counting rates.

III. PROTON SPECTRA

A. Experimental Procedure and Results

The present section describes single-counter measurements of proton spectra resulting from the He^3 bombardment of He^3 over an energy range from 3 to 18 MeV. The measurements were made with a solid-state counter telescope positioned in a 30-cm diameter gas scattering chamber (see Part II, B and Figure 2) and are in the form of angular distributions at thirteen laboratory angles from 15° to 160° for nine bombarding energies.

The counter telescope consisted of a 48μ surface-barrier ΔE counter and either a 3 mm or 5 mm deep lithium-drifted E counter. A block diagram of the electronics is given in Figure 6a. The pulses from each detector were fed into a low-noise, charge-integrating preamp (Tennelec Model 100A), summed to form a pulse proportional to $(E + \Delta E)$ and fed into one of two 200-channel sections of a RIDL 400-channel analyzer. The routing of the analyzer was determined by the size of the pulse in the ΔE counter. All pulses corresponding to an energy greater than ~ 2 MeV (the thickness of the ΔE detector to protons) were routed into a "charge 2" spectrum. All pulses below the 2 MeV level which fired a lower level discriminator (set close to the noise level in the ΔE counter) were stored in the "charge 1" spectrum. This latter condition satisfied the logic requirements of the analyzer and also allowed one to eliminate some of the neutron background produced at the higher bombarding energies by (n, α) and (n, p) nuclear reactions in the active volume of the E detector.

For each experimental run the gains of the ΔE and E pre-amplifiers were balanced to 0.5% using a high energy proton group from the reaction $D(\text{He}^3, p)\text{He}^4$ ($Q = +18.354$ MeV). The channel-to-energy conversion of the analyzer was determined by using the angular variation of the energies of both charge 1 and charge 2 particles from the same reaction. The energy calibration of the charge 1 portion of the analyzer is shown in Figure 7 for the experimental run at 9.94 MeV. For proton energies above 14 MeV the response of the detector was found to be non-linear. This necessitated fitting the energy-channel curve in several regions in order to handle the departure from a linear response function.

As described in Part II, B.4 only a few additional quantities were required in order to relate the yield at each angle to a differential cross section. The target pressure and temperature were monitored hourly and the current integrator was calibrated several times for each running day. Corrections made at the extreme forward angles for the analyzer dead time were always less than 20%. The absolute normalization at each energy was verified by comparing the $\text{He}^3 + \text{He}^3$ elastic cross section at $\theta_L = 30^\circ$ to more accurate measurements (Tombrello and Bacher, 1963 and Bacher and Tombrello, 1965). Several of the high energy points were corrected by $\sim 10\%$ on this basis.

Angular distributions of separated charge 1 particle spectra were obtained at 2.81, 4.35, 5.92, 7.95, 9.94, 11.93, 13.81, 15.55 and 18.01 MeV. As indicated in the Introduction, below 10.98 MeV protons are the only charge 1 particles available in the final state. Above this energy the reaction $\text{He}^3(\text{He}^3, d)\text{pHe}^3$ becomes energetically allowed and it is possible to observe deuterons in the charge 1 spectra. Above 13.90 MeV tritons can be produced in the $\text{He}^3(\text{He}^3,$

t)3p reaction but their presence in these spectra can be ignored since the cross section for their production is down by at least an order of magnitude from that for the production of deuterons (see Part IV, D).

Figure 8 shows a sequence of the charge 1 energy spectra at a laboratory angle of 20° for five of the bombarding energies. The spectra have been unfolded from smooth curves drawn through the original measurements in order to illustrate how the reaction mechanism develops over a wide range of bombarding energy. At low bombarding energies the spectrum shape is characterized by a peak at the high energy end which represents the remaining $(p + \text{He}^4)$ system being left at an excitation corresponding to the Li^5 ground state. The dashed line under this peak traces the position of the Li^5 ground state peak in the spectra shown for the higher bombarding energies. The height of the ground state peak gives a rough indication of how the cross section for the Li^5 reaction mode increases with increasing energy. The dashed lines spanning a region in the spectra at lower particle energies indicate the range of energies expected for protons from the breakup in flight of the recoiling Li^5 's. It is apparent that above the threshold for the formation of deuterons, additional structure is present in the lower energy region of the spectra, implying that other processes are beginning to contribute substantially to the reaction mechanism.

Samples of the actual spectra can be seen for the measurements at 2.81 MeV in Figure 16 and at 18.01 MeV in Figure 17. The behavior of the proton spectra at 7.95 MeV as a function of angle is indicated in Figures 12 - 15 for angles from 20° to 140° in 20° steps. In these cases the actual spectra are shown and an energy scale has been provided at the top of each figure. The point corre-

sponding to the minimum separation energy of the counter telescope is indicated in each case by an arrow near an energy of 2 MeV.

B. Final-State Enhancements

The prominence of the Li^5 ground state group in the observed proton spectra leads one to investigate models for the reaction mechanism which include the presence of a single strong interaction between a pair of particles in the final state. In these models the first particle (in our case, a proton) is assumed to experience no interaction with the strongly interacting pair (the recoiling Li^5). This is equivalent to a factorization of the wave function into two parts; one depending on the coordinates of the first particle and the other depending separately on the motion of the center-of-mass and on the relative coordinates of the interacting pair. The phase-space energy distribution that arises from the assumption of a constant matrix element for the transition from the initial to the final state can be expressed in this factored form as;

$$\partial^2 N / \partial E_3 \partial \Omega_3 \propto k_3 \cdot k_{45} .$$

The particles in the reaction are labeled by the convention

$$1 + 2 \rightarrow 3 + 4 + 5 ,$$

k_3 is the wave number of particle 3 and k_{45} is the wave number corresponding to the relative motion in the (4-5) system. Departures from this distribution are termed enhancements and several

formalisms are available for treating the case where the enhancement is produced by an interaction between a single pair of particles.

As was pointed out by Fermi (1951) the appropriate enhancement factor is just the modulus squared of the wave function for the interacting pair evaluated at the limit of small spatial separation. (For further discussion of this and succeeding points see Gillespie, 1964). In certain instances (i. e., short-range, attractive interactions) this may be approximated by the scattering cross section for the interacting pair as indicated by Watson (1952) and Migdal (1955). We have

$$\frac{\partial^2 \sigma}{\partial E_3 \partial \Omega_3} \propto k_3 \cdot k_{45} \cdot |\varphi(k_{45}, r)|_{r=0}^2, \quad (\text{Fermi})$$

and

$$\approx k_3 \cdot k_{45} \cdot \sigma_{45}(k_{45}). \quad (\text{Watson-Migdal})$$

In the Watson-Migdal form the scattering cross section may be represented by an effective-range parametrization (see Appendix A, 2) or it may be attributed to the variation of the phase shift for a particular orbital angular momentum ℓ and total angular momentum j . In the latter case it may be ascribed to a single level that has been parametrized by a Breit-Wigner single-level formula (Lane and Thomas, 1958, pages 334-336). From the R-matrix formalism we have,

$$\frac{\partial^2 \sigma}{\partial E_3 \partial \Omega_3} \approx k_3 \cdot \frac{\sin^2 \beta_\ell^j}{\text{Penetration Factor}} \quad (\text{R-matrix})$$

$$\approx k_3 \cdot \frac{A_\ell^2}{\rho_{45}} \cdot \frac{(\Gamma_j/2)^2}{(E_j + \Delta_j - E_{45})^2 + (\Gamma_j/2)^2},$$

where $\beta_\ell^j = \delta_\ell^j + \varphi_\ell$ is the resonant phase shift, the penetration factor is ρ_{45}/A_ℓ^2 , $A_\ell^2 = F_\ell^2 + G_\ell^2$, F_ℓ and G_ℓ are the regular and irregular Coulomb functions evaluated at $(k_{45}R)$, $\varphi_\ell = \tan^{-1}(F_\ell/G_\ell)$, $\Gamma_j/2 = \gamma_j^2 \rho_{45}/A_\ell^2$, E_j is the characteristic energy of the level, Δ_j is the level shift, γ_j^2 is the reduced width and R is the radius. The factor k_{45} has been absorbed into the second term.

The enhancement factor described by Fermi (1951) can be shown to be equivalent to the spectral measure function, $1/|f_\ell^j(k)|^2$, that arises from an S-matrix treatment of the scattering formalism (Gel'fand and Levitan, 1951 and Newton, 1960). The Jost function, $f_\ell^j(k)$, can be described either in terms of the scattering phase shift or in terms of the potential producing the interaction. In terms of the scattering phase shift for a particular partial wave, we have

$$f_\ell^j(k) = \exp \left[\frac{2}{\pi} \int_{0+i\epsilon}^{\infty+i\epsilon} \frac{x \delta_\ell^j(x) dx}{x^2 - k^2} \right],$$

where δ_ℓ^j is the complete phase shift,

$$\delta_{\ell}^j = \delta_{\ell, \text{nuc}}^j + \delta_{\ell, \text{Coulomb}}^j ,$$

composed of both nuclear and Coulomb terms and $k \equiv k_{45}$. Treating these Coulomb terms explicitly (Tombrello, 1964 and 1965) one obtains for the spectral measure function,

$$\begin{aligned} \frac{1}{|f_{\ell}^j(k)|^2} &= k^{2\ell} \cdot \left[\frac{2\pi\eta}{\exp(2\pi\eta)-1} \right] \cdot \prod_{t=1}^{\ell} \left(1 + \frac{\eta^2}{t^2} \right) \cdot \frac{1}{|f_{\ell, \text{nuc}}^j|^2} , \\ &\equiv W(k, \eta, \ell) / |f_{\ell, \text{nuc}}^j|^2 , \end{aligned}$$

where $\eta = \mu_{45} Z_4 Z_5 e^2 / \hbar^2 k$ and the latter equation is used to define the function $W(k, \eta, \ell)$ containing the Coulomb effects. The spectral measure function prediction (hereafter abbreviated SMF) for the enhancement is given by,

$$\frac{\partial^2 \sigma}{\partial E_3 \partial \Omega_3} \propto k_3 \cdot k \cdot W(k, \eta, \ell) \cdot \frac{1}{|f_{\ell, \text{nuc}}^j|^2} , \text{ (SMF)}$$

where

$$f_{\ell, \text{nuc}}^j = \exp \left[\frac{2}{\pi} \int_{0+i\epsilon}^{\infty+i\epsilon} \frac{x \delta_{\ell, \text{nuc}}^j(x) dx}{x^2 - k^2} \right] .$$

By analogy with the form of the Coulomb factor $W(k, \eta, \ell)$, one can also generalize the above to include effects due to the Coulomb interaction of particle 3 with the strongly interacting (4-5) system (Tombrello and Bacher, 1965). With this inclusion we have

$$\frac{\partial^2 \sigma}{\partial E_3 \partial \Omega_3} \propto k_3 \cdot k \cdot W(\tilde{k}_3, \tilde{\eta}_3, \ell_3) \cdot W(k, \eta, \ell) \cdot \frac{1}{|f_{\ell, \text{nuc}}^j(k)|^2},$$

where \tilde{k}_3 , $\tilde{\eta}_3$ and ℓ_3 are defined for the relative motion of particle 3 with respect to the (4-5) system.

Determination of the Jost function, $f_{\ell, \text{nuc}}^j(k)$, is possible only for a few two-particle systems where a phase shift analysis of scattering measurements is available over a wide range of bombarding energies. In spite of this limitation, the advantage of the SMF formalism over the R-matrix single-level description is that it approaches the appropriate Coulomb-modified phase space expressions in the limit of no nuclear interaction, whereas the R-matrix expression approaches zero in the limit that β_{ℓ}^j becomes small.

C. Li^5 Ground State Model

1. Spectrum Calculation

In the present model the energy spectra of protons from the reaction $\text{He}^3(\text{He}^3, 2p)\text{He}^4$ are calculated assuming that the first proton leaves a recoiling $(p + \text{He}^4)$ system with which it has had no interaction (other than Coulomb). Predictions of the spectrum shapes are made using density functions that describe the relative

populations of the various excitations in the $(p + \text{He}^4)$ system. These have been determined for both the R-matrix and the SMF formalisms described in the previous section. Figure 9 shows the behavior of these two density functions as a function of the excitation in the $(p + \text{He}^4)$ system. The R-matrix curve has been calculated from parameters for the $3/2^- \text{Li}^5$ ground state,

$$E_{3/2^-} = 4.79 \text{ MeV}, \quad \gamma_{3/2^-}^2 = 8.23 \text{ MeV} \quad \text{and} \quad R = 3.0 \text{ fm.},$$

which were obtained from a single-level fit to the results of a phase shift analysis of the scattering of protons from He^4 (Barnard et al., 1964). The $\delta_1^{3/2}$ phase shift from the same analysis was used to evaluate the SMF curve. The two density functions are similar in the region close to the Li^5 ground state, but at higher excitations in the $(p + \text{He}^4)$ system the SMF curve remains considerably above that obtained from the R-matrix expression.

From a knowledge of the density function it is a straightforward procedure to calculate a spectrum shape for the first proton. For computational purposes it is convenient to first determine the energy spectrum in the center-of-mass system where it is independent of angle.

$$\widetilde{\frac{\partial^2 \sigma}{\partial E_3 \partial \Omega_3}} \propto \widetilde{k}_3 \cdot W(\widetilde{k}_3, \widetilde{\eta}_3, \ell_3) \cdot P(k, \eta, \ell).$$

The $\widetilde{}$ sign refers to quantities in the center-of-mass system (of 3-45 in this case), W is the modification to include Coulomb effects of the first particle and $P(k, \eta, \ell)$ is the density function of either

kind. The spectrum shape is transformed to the corresponding shape at a fixed laboratory angle by using the relativistic invariant (Williams, 1961)

$$\frac{1}{\tilde{P}} \left(\frac{\partial^2 \sigma}{\partial E \partial \Omega} \right) = \frac{1}{P} \left(\frac{\partial^2 \sigma}{\partial E \partial \Omega} \right) .$$

The result is a spectrum prediction for the shape of the high energy proton peak that can be used to extract cross sections for the Li^5 ground state mechanism (Bacher, 1963 and Bacher and Tombrello, 1965a). However, in order to allow comparisons to be made with the shape of the entire spectrum, it is useful to push the model to its logical extremes and also use it to predict the spectrum shape of the low energy protons that results from the decay in flight of the recoiling Li^5 . This is a slightly more cumbersome calculation in that it requires taking into account contributions from a wide range of center-of-mass angles at each excitation in the Li^5 system. The spectrum calculation must also proceed in an iterative fashion (which converges rapidly) since the recoil contribution depends not only on the angular orientation of the Li^5 breakup but also on the angular distribution of the first stage yielding the high energy proton. (See Appendix A. 3 for a more detailed account of the recoil spectrum calculation.)

The problem of combining these two spectra has been treated here in the classical approximation by directly adding the two calculated shapes to obtain the total spectrum. In the proper quantum mechanical treatment the fact that the two spectra represent identical particles would have to be included and allowance would have to be made for the possibility of interference.

The total spectrum is modified by folding various resolution functions into it to allow a direct comparison with the data. A triangular resolution function with $\text{fwhm} = 3.6^\circ$ was used to include the effect on the energy spectrum of the angular resolution of the detector system (see Figure 5). To relate this $\Delta\theta$ to an energy uncertainty $\Delta E = (\partial E/\partial\theta)\Delta\theta$, the value of $(\partial E/\partial\theta)$ at the center of the high energy proton peak was used. The value of $(\partial E/\partial\theta)$ did not change rapidly over the region of this peak and this same value of $(\partial E/\partial\theta)$ was found to adequately represent the shift with angle of the leading edge of the low energy recoil spectrum. The resolution of the counter telescope was folded into the spectrum as a Gaussian shape with a width determined from the peaks observed in the energy calibration of the analyzer. For the forward angle spectra at bombarding energies above 10 MeV, it was necessary to allow for a poorer resolution of the detectors for high energy protons ($E_p > 20$ MeV). In converting the predicted shapes to the analyzer-channel scale it was necessary to allow for a compression of the spectrum due to the non-linear response of the detectors to high energy particles (see Figure 7).

The final result is a prediction of the spectrum shape, including all of the experimental uncertainties, that can be compared directly to the observed spectra.

2. Comparison with Experimental Spectra

In Figure 10 the results of calculations using several different density functions are compared with the spectrum measured at a He^3 bombarding energy of 7.95 MeV and a laboratory angle of 20° . In the top half of the figure the spectrum obtained using the

SMF density function and including an $\ell_3 = 1$ Coulomb interaction for the first proton is compared with the observed spectrum. The dashed lines indicate the portions of the total spectrum that are due to the high energy proton leaving Li^5 and to the breakup of the recoiling Li^5 . For the recoil spectrum the angular distribution of the first stage has been included (see the next section), but the breakup of the Li^5 has been taken to be isotropic.

In the bottom half of Figure 10 the predicted shapes for several different density functions are compared. Curve A (solid line) repeats the SMF prediction with $\ell_3 = 1$ that was indicated in the upper figure. Curve B shows the spectrum obtained from the R-matrix density function with no Coulomb interaction for the first proton. This agrees closely with Curve A, but it should be noted that the corresponding R-matrix curve with $\ell_3 = 1$ would fall considerably below Curve A. Curve C indicates the shape expected for a contribution from the first excited state of Li^5 ($J^\pi = 1/2^-$) as determined from the R-matrix density function with no Coulomb interaction for the first proton. The fact that this does not differ substantially from the shape of the phase space prediction given by Curve D is not surprising, considering the ~ 4 MeV width of the broad first excited state (see Figure 1).

It is clear that the inclusion of the recoil spectrum in the calculation allows us to make more reasonable comparisons between the predicted shapes and the observed spectra. The comparisons of Figure 10 are representative of the relative sizes of the predicted shapes, independent of energy and angle. Since $\ell_3 = 1$ is the outgoing orbital angular momentum that would be required for the first proton by an s-wave interaction in the incoming channel ($\text{He}^3 + \text{He}^3$), and since it is difficult to imagine a mechanism by which the Coulomb

interaction of the first proton would be screened, it seems reasonable to use the SMF weighting with $\ell_3 = 1$ for the further comparisons of the predicted shapes with the observations. It is worth noting, however, that the cross sections derived from SMF ($\ell_3 = 1$) and R-matrix (no interaction) agree to within 3% for the fits at 7.95 MeV, while the difference between SMF ($\ell_3 = 1$) and SMF (no interaction) is about 25%.

Figure 11 indicates for the case of 9.94 MeV and 20^0 the technique used to normalize the predicted spectrum to the experimental one and thereby extract a cross section for the Li^5 ground state transition. Taking the peak position at X_P , the normalization of the predicted spectrum was determined by matching the area under the curve above X_A (a point $\sim 2/3$ down from the peak height) to the number of counts observed in the corresponding region of the experimental spectrum. A "best fit" to the experimental spectrum was then obtained by varying the peak position X_P slightly ($\sim \pm 0.5$ channels) and determining the value of X_P which minimized the mean-square deviation of the two curves,

$$\Delta^2 (X_P) = \frac{1}{n} \sum_{i=1}^n \frac{(N_i^{\text{exp}} - N_i^{\text{th}}(X_P))^2}{N_i^{\text{exp}}}$$

Here, N_i^{exp} and $N_i^{\text{th}}(X_P)$ are the experimental and theoretical curves, respectively, and n is the number of channels with counts in the experimental spectrum above X_A . A new calculation was made for this "best value" of X_P (see the inset of Figure 11) and the total yield for the spectrum was then taken to be the area under the dashed curve, corresponding to that portion of the spectrum due to the first proton.

In this manner a consistent set of fitted spectra was obtained for the angular distributions at each of the nine bombarding energies. Our attention can now be turned to the quality of the fits and to the angular and energy dependence of the yield obtained for the Li^5 ground state transition.

The most stringent test of the Li^5 ground state model for the reaction mechanism is to look at the quality of the fits as a function of angle for a fixed bombarding energy, particularly in the region away from the high energy peak. Figures 12 - 15 give this comparison at angles in 20° steps from 20° to 160° for the measurements at a bombarding energy of 7.95 MeV (below the threshold for the formation of deuterons). The calculated spectra all include an angular distribution for the first proton of $(1 - 0.24 \cos^2 \tilde{\theta})$, the average of the measurements below 10 MeV (see Table III). Two fitted curves are shown for each angle. The solid curve assumes that the recoiling Li^5 breaks up isotropically in its own center-of-mass system and the dashed curve indicates the effect of an oriented breakup $(1 - 0.875 \cos \theta_R)$ for the protons with respect to the recoil direction. This latter distribution is suggested by the shape of the alpha-particle spectrum for forward angles at 12 MeV (see Part IV, B and Figures 37 and 38). While it is expected to be good for the far forward angles, the correct orientation appears to diminish rapidly with increasing angle. The same form is included in the present curves only to indicate the sensitivity of the spectrum calculation to this parameter at the backward angles.

The inclusion of the oriented breakup improves the agreement with the observed shape at the forward angles and gives a more reasonable description of the number of counts in the low energy part of the spectrum. However, it is not clear why it should improve

the fit at 20° , 60° and 80° , but not do as well at 40° (see Figures 12 and 13). For the spectra at angles greater than 80° (see Figures 14 and 15) the rapid rise in the spectrum near the arrow (which represents the separation threshold of the counter telescope) is suggestive of a background contribution from neutrons. This eliminates the lower energy region for the purpose of these comparisons. For the spectra at 140° and 160° (see Figure 15) there appears to be a significant number of excess counts in addition to this background component. From the alpha-particle measurements described in Part IV, B one discovers that there is a sharply forward-peaked component of the reaction mechanism that involves the 1S_0 p-p interaction. The forward alpha-particle angles for this mechanism at 7.95 MeV produce protons in the energy range 1 - 5 MeV for the spectra at 140° and 160° . It would appear that the inclusion of this effect would remove some of the discrepancy in the number of counts observed at the extreme backward angles. In the spectrum at 20° (see Figure 12), protons from the p-p mechanism would be spread over the energy range from 6.6 - 12.8 MeV and would be due to alpha particles with a laboratory angle of 120° ($\sim 160^\circ$ in the He^4_+ (2p) center-of-mass system).

In Figure 16 the observed spectra and similar calculated shapes are shown for 40° and 90° at a bombarding energy of 2.81 MeV. The nature of these fits is quite similar to those at 7.95 MeV, with the exception that a slight excess appears in the middle region of the spectrum for the lower bombarding energy (see Part VI for further details). In the 40° curve at each of these bombarding energies, the data deviate markedly from the high recoil spectrum peak given by the oriented breakup prediction for the spectrum shape.

The spectrum at 20° for 18.01 MeV (see Figure 17) shows how the complexity of this reaction increases as additional channels open. For the Li^5 mode, the angular distribution of the first stage is now given by $(1 + 0.5 \cos^2 \tilde{\theta})$ and the two curves shown are for an isotropic breakup of the Li^5 (solid line) and an oriented breakup (dashed line) given by $(1 - 0.5 \cos \theta_R)$. The extreme non-linearity of the detector response has greatly accentuated the height of the high energy proton group relative to the contribution from the recoil breakup. This low energy component is buried by additional peaks which can be seen in Figure 8 to dominate the low energy portion of the forward angle spectra for bombarding energies above 12 MeV. The windows shown indicate possible explanations for these prominent features.

The higher energy peak appears to be due to protons from the $\text{He}^4 + (2p)$ mode with the associated alpha particle at a laboratory angle of 90° . The fact that this corresponds to a center-of-mass angle of $\sim 160^\circ$ helps to explain the large size of the peak, since this process is known to be strongly forward-peaked and the presence of identical particles in the initial state requires symmetry about $\tilde{\theta} = 90^\circ$ (assuming no φ -dependence). It is not understood why this mechanism becomes so much more prominent at the higher bombarding energies, although it does appear to occur in a region of the compound nucleus, Be^6 , where strong $\ell = 3$ effects are observed in the elastic scattering (see Figure 1).

The lower peak appears to arise from protons produced in the mechanism $d + (p - \text{He}^3)$. Observations of the deuteron spectrum at forward angles (see Part IV, C and Figure 41) indicate a peak at a $p - \text{He}^3$ relative energy between 1 and 2 MeV. The deuterons from the same mechanism also fall in this energy region,

so it is quite likely that this lower peak consists of both protons and deuterons. This would help somewhat to explain its width.

3. Angular Distributions

As a result of the decision to keep the observed spectra intact and to fit the calculated shapes in the laboratory system, differential cross sections for the Li^5 ground state transition were extracted from the fitted spectra at each laboratory angle, as described in the previous section (see Figure 11). This yields values of

$$\frac{d\sigma}{d\Omega_3} = \int_0^{E_{3, \text{Max}}} \left(\frac{\partial^2 \sigma}{\partial E_3 \partial \Omega_3} \right) dE_3$$

as a function of the laboratory angle. Figure 18 gives a comparison of the laboratory angular distributions obtained from the measurements below 8 MeV. Over this region the cross section is increasing rapidly and the peaking at forward angles is primarily due to the increased center-of-mass motion. The cross sections in the laboratory system were transformed to the center-of-mass system by assuming a two-body transformation

$$\left(\frac{d\sigma}{d\tilde{\Omega}} \right) = \left(\frac{d\sigma}{d\Omega} \right) \frac{\sin^2 \theta \cos(\tilde{\theta} - \theta)}{\sin^2 \tilde{\theta}} .$$

This approximation is reasonable in the present case since at a given laboratory angle θ , the corresponding center-of-mass angle $\tilde{\theta}$ changes by an amount less than the angular resolution of the detectors down to a very low energy in the calculated high energy proton curve.

The angular distributions obtained from the Li^5 ground state model are presented in Figures 19 - 22. Solid dots represent the laboratory cross sections and open circles give the center-of-mass cross sections at the corresponding center-of-mass angle. The center-of-mass angular distributions appear to be roughly symmetric about $\tilde{\theta} = 90^\circ$, although the points at the forward angles appear to be somewhat higher than those at the relevant backward angles. This may be indicative of an additional mechanism interfering with the fitting procedure at the forward angles, but it should also be remembered that strict symmetry about $\tilde{\theta} = 90^\circ$ is required only if the reaction mechanism has no φ -dependence.

The solid curves indicated on Figures 19 - 21 for the bombarding energies below 12 MeV represent a least-squares fitting of the function $a_0 + a_2 P_2(\cos\tilde{\theta})$ to the center-of-mass results for $\tilde{\theta} \geq 90^\circ$ (to avoid the problems at forward angles). It is clear that at the higher energies higher powers of $\cos^2\tilde{\theta}$ are required to fit the observed distributions, but there are not enough points at the backward angles to make such a fit meaningful. The shape of these distributions changes at the higher bombarding energies as one approaches the region in Be^6 where a broad anomaly is observed in the elastic scattering channel (Bacher and Tombrello, 1965). The parameters a_2/a_0 from these fits are given in Table III and the energy dependence of this ratio is indicated in Figure 23. Below 10 MeV the values of a_2/a_0 show a reasonable scatter about their

average value $\overline{(a_2/a_0)} = -0.175$. In terms of powers of $\cos\tilde{\theta}$ this corresponds to a distribution $(1 - 0.24 \cos^2\tilde{\theta})$.

D. Cross Section Determinations

1. Li^5 Ground State Model

Cross sections for that portion of the reaction which proceeds through the Li^5 ground state were obtained by determining the area under each of the angular distributions indicated in Figures 19 - 22. The measurements for all of the center-of-mass angles were fitted by a least-squares technique to a Legendre polynomial expansion of the form,

$$\sum_{l=0}^{l_{\max}} a_l P_l(\cos\tilde{\theta}) \quad (l \text{ even}) ,$$

using the smallest value of l_{\max} (typically 4 or 6) which gave an adequate fit to the differential cross sections. The total cross section for the Li^5 ground state mechanism was then taken to be

$$\sigma_{\text{Li}^5} = 4\pi a_0 ,$$

and the error assigned to this quantity was the resultant error in a_0 arising from the relative errors assigned to each of the differential cross sections in a given angular distribution.

The results are given in Table IV and in Figure 24 they are plotted as a function of the He^3 bombarding energy. Also plotted on this figure are results obtained from a series of measurements of

unseparated spectra. The agreement between these two sets of measurements is seen to be very good.

The various contributions to the relative errors of each point of an angular distribution are discussed in Part II, B.4 and have been summarized in Table II. The error assigned to each point included the systematic errors, the statistical uncertainty in the total number of counts above X_A (see Figure 11), and an uncertainty assigned to the energy calibration of the multi-channel analyzer. This latter contribution was typically 0.4 to 0.7%, but at the forward angles for the higher bombarding energies (where the response of the detector was non-linear) it was as large as 2%.

Apart from these relative errors, the absolute value including the normalization to the $\text{He}^3 + \text{He}^3$ elastic scattering is good to 5% below 12 MeV and to 10% for the higher energy measurements. The uncertainties due to the spectrum calculation are difficult to estimate but they are probably of the order of 10%.

2. Integrated Charge 1 Measurements

As a check on the applicability of the Li^5 ground state model, total cross sections for the reaction were obtained by determining the total yield of charge 1 particles seen at each angle. Since the counter telescope only allowed measurements of separated spectra down to ~ 2 MeV, the major uncertainty in these cross sections involved the extrapolation of the spectrum to zero energy. An additional uncertainty in the shape of the low energy region was introduced by the possibility of a background contribution at the higher bombarding energies due to neutron induced events in the active volume of the detectors.

Figure 25 illustrates the technique that was used to make these low energy extrapolations and to assign them errors. The spectra at 2.81 MeV and 4.35 MeV were observed to have less background down to the routing threshold of the counter telescope. They were used to establish a ratio,

$$(\text{extrapolated height})/(\text{high energy peak height}) ,$$

at each angle that could be employed to determine the height of the extrapolation for the spectra at the higher bombarding energies. In case the low energy spectrum was actually observed to turn over and head toward zero (as in Figure 17 for 18 MeV and 20°), this slope was continued. The uncertainty assigned to the total yield at each angle was one half of the extrapolated yield, as indicated by the shaded area in Figure 25.

The results of these determinations of "integrated charge 1 yield" are indicated in Figures 26 - 28 as angular distributions in the laboratory system. The typical errors are again a cumulative error involving the systematic errors, the statistical error on the total yield (now very small), and the error determined by the amount of extrapolated yield. The latter is the dominant contribution at all angles. The shapes of these distributions are all strongly forward-peaked indicating that there are a large number of low energy particles that are carried forward by the center-of-mass motion. This forward-peaking is further enhanced at bombarding energies above the threshold for the formation of deuterons in the final state.

Total cross sections were obtained from these angular distributions by least-squares fitting a Legendre polynomial expansion

(this time for all ℓ -values) to the observed differential cross sections. The total cross section is then

$$\sigma_T = \frac{1}{2} (4\pi a_0) ,$$

since all of the three-body reaction channels open in this energy region produce two charge 1 particles in the final state. (The reaction $\text{He}^3(\text{He}^3, t)3p$ is shown in Part IV to have a relatively small cross section when it is compared to the cross sections for the other open channels.)

The values of the total cross section obtained in this manner are given in Table IV and the energy dependence is illustrated in Figure 29. Above the threshold for the reaction $\text{He}^3(\text{He}^3, d)p\text{He}^3$ the cross section increases rapidly. The errors in the total cross section vary from 3 - 5% and are derived from the errors assigned to each point. These are determined mainly by the uncertainty in the extrapolation of each spectrum to zero energy and in all cases the estimate of the error is extremely conservative. This would tend to reduce the sensitivity of the final result to any systematic error in the extrapolation technique although the possibility of such an effect (< 10%) is still present. The uncertainty of the normalization to the elastic scattering measurements is still applicable to the absolute value of these cross sections.

3. Comparison of Cross Sections

Figure 30 shows the value of the ratio of the total cross section for the production of charge 1 particles to the cross section

derived from the Li^5 ground state model. The values of these ratios are also given in Table V. For the points between 3 and 12 MeV the values of this ratio are consistent with the average value 1.19. This indicates that the Li^5 ground state model comes close to predicting the total number of particles correctly over a rather wide range of bombarding energies. Above 12 MeV the presence of other open reaction channels rapidly becomes important.

In Figure 31 a comparison of the shapes of the laboratory angular distributions is made for the two cross section measurements at a bombarding energy of 2.81 MeV. The factor of 2 has been removed to facilitate the comparison and the distributions have been plotted as a function of $\cos\theta_{\text{LAB}}$ to illustrate how well the measurements cover the physical region. The difference between the two techniques for extracting a cross section is most apparent at the forward angles where there is also the largest uncertainty in the extrapolation technique.

The comparisons of the shapes of the proton spectra with shapes calculated from the Li^5 ground state model have indicated that between 3 and 12 MeV a considerable fraction of the observed spectra can be explained in terms of a strong p - He^4 final state interaction. In the following section we will see how effects due to a p-p interaction can be detected in measurements of the alpha-particle spectra at forward angles.

IV. MAGNETIC SPECTROMETER MEASUREMENTS

A. Experimental Procedure

Concurrent with the measurements of the charge 1 particle spectra described in Part III, energy spectra were also obtained for the charge 2 particles. These spectra were dominated by the elastically scattered He^3 's and exhibited a poor energy resolution as a result of the slow rise times of the pulses from charge 2 particles in the E counter (3 mm, lithium-drifted silicon detector). At forward angles where the alpha particles had enough energy to lie significantly higher in energy than the elastic He^3 group, there was an indication of structure near the end point of the spectrum.

In order to obtain alpha-particle spectra with improved resolution and to avoid the high count rates from the elastically scattered He^3 's, a gas target was used with the 61-cm magnetic spectrometer. This has been described in Part II, C and only the points pertinent to the individual measurements will be given here. For the alpha-particle and deuteron measurements the 16-counter array was employed. The adjacent scans were overlapped by 50% to average out uncertainties due to the counter correction factors. The energy resolution $\Delta E/E$ corresponded to $1/360$ and the angular aperture was $\Delta\theta = \pm 1^\circ$ and $\Delta\phi = \pm 2^\circ$. The alpha-particle and deuteron energies were determined from the frequency of an NMR probe. These energies were corrected for the energy loss in the target gas and in the exit foil (10,000-Å Ni) to obtain the corresponding particle energy at the center of the gas target.

For the observation of tritons from the reaction $\text{He}^3(\text{He}^3, t)^3\text{p}$, it was necessary to use a He^3 bombarding energy of 20 MeV

in order to obtain a sufficiently high counting rate to determine the shape of the energy spectrum. The exit slit of the gas cell was redesigned to allow measurements to be made as far forward as 4° . At 18 MeV the counting rate at the peak of the triton spectrum doubled in going from 6° to 4° and tripled in going from a bombarding energy of 18 MeV to 20 MeV. For the experimental runs at 20 MeV and 4° , the counting rate at the peak of the triton energy spectrum was ~ 25 counts/min. A single counter was used with exit slits on the spectrometer giving an energy resolution of $1/90$. At 20 MeV and 4° the maximum triton energy was in excess of 11 MeV and considerably above the highest magnetic field at which the NMR probe could be operated (49.5 Mc/sec or 9.5 MeV tritons). It was therefore necessary to set the magnet current with a precision helipot which was later calibrated by observing singly charged He^3 's scattered from a gold foil. During the experimental run foils (1 - 3 mil Al) were used to separate the tritons from singly charged He^3 's which filtered through the magnet in relatively large numbers ($10^5 \text{ He}^3 : 1t$).

B. Alpha-Particle Spectra at 12 and 18 MeV

Measurements of the momentum spectrum of alpha particles were made at a He^3 bombarding energy of 11.96 MeV for laboratory angles of 10° , 15° and 30° and are presented in Figures 32, 33 and 34, respectively. Particular features of the individual spectra are identified in the figure captions, but they are all characterized by a broad peak or shoulder due to the Li^5 ground state and by a strongly forward-peaked component that appears near the three-body end point, well above the arrows which indicate the extent of the Li^5 ground state

group. From an examination of the position of this peak with respect to the scales showing the excitation in the 2p system, it appears to be due to an interaction in the p-p system (Tombrello and Bacher, 1965). The preliminary spectrum calculation shown in Figure 32 uses the Watson-Migdal formalism and the effective-range parametrization for the 1S_0 p-p interaction (see Appendix A. 2). This reproduces the shape of the leading edge and peaks properly at a 2p excitation of about 800 keV.

In spite of the elaborate precautions taken with a cold trap to reduce the effects of contaminants, several sharp peaks are seen at the forward angles. These are due to recoil alpha particles from a slight He^4 contaminant and to alpha particles from the reaction $\text{O}^{16}(\text{He}^3, \alpha)\text{O}^{15}$ to the ground and 6.16 MeV states of O^{15} .

Energy spectra were obtained by transforming smooth curves through the original momentum spectra and adjusting the normalization to allow for the different target thicknesses seen at each angle. These are presented together in Figure 35 and show the strongly forward-peaked nature of the p-p contribution, as well as a considerable change in the shape of the back edge of the broad group due to the Li^5 ground state.

Measurements of the alpha-particle spectrum were also made at a bombarding energy of 17.87 MeV for 6° and 15° . The momentum spectrum obtained at 6° is shown in Figure 36. The sharp peak due to the p-p interaction is now comparable in size to the broad group arising from the Li^5 ground state, and a preliminary spectrum calculation of the same type reproduces its general features. It should be noted that the alpha particle, being the residual mass, gives the best signature of the p-p interaction in the same way that the high energy proton peak studied in Part III reflects the Li^5 ground state interaction of the p- He^4 system.

In an attempt to understand the spectrum shape of the alpha particles and the relative importance of the p-He⁴ and the p-p final-state interactions, calculations of these spectrum shapes were made using the following simple model. The alpha-particle spectrum is considered to be produced by two non-interfering reaction mechanisms, He⁴ + (2p) and Li⁵ + p. The alpha-particle spectrum from the Li⁵ reaction mode, $f(E, \theta)$, is calculated from the recoil breakup formalism (see Appendix A, 3) using the spectral measure function to weight excitations in the Li⁵ system. This calculation is not particularly sensitive to the form of the density function used, but it does depend on the angular distributions associated with each stage of the sequential decay. Angular distribution parameters for the first stage were derived in the analysis of the proton spectra in Part III (see Table III). In the second stage one must include the possibility of an orientation of the breakup of the Li⁵ with respect to its recoil direction. The importance of this second angular distribution will soon be apparent.

The alpha-particle spectrum resulting from the (2p) reaction mode, $g(E, \theta)$, is calculated using the Watson-Migdal approximation with the p-p scattering cross section parametrized by the effective-range formalism (see Appendix A, 2). These two spectrum shapes are then added incoherently to produce an alpha-particle spectrum, $h(E, \theta)$, at a laboratory angle θ .

$$h(E, \theta) = A(\theta) f(E, \theta) + B(\theta) g(E, \theta) .$$

The values of $A(\theta)$ and $B(\theta)$ are determined by requiring that the calculated spectrum match the experimental distribution at the two

peaks in the spectrum corresponding to the Li^5 mode (E_{Li^5}) and the (2p) mode (E_{2p}).

In Figure 37 the result of this sequential decay model is illustrated for the alpha-particle spectrum at 11.96 MeV and 10° . The experimental distribution is represented by the heavy line with error bars giving the order of the statistical uncertainties in individual points of the momentum distribution (Figure 32). The light line labeled (0.875) represents the calculated spectrum, and the components due to the Li^5 and (2p) reaction modes are indicated. The contribution to the spectrum from each final-state interaction was determined by requiring the total spectrum to fit the experimental distribution at the two peaks. In the Li^5 mode the angular distribution for the first stage was $(1 - 0.14 \cos^2 \tilde{\theta})$, as determined from the proton measurements. The orientation of the Li^5 breakup required to reproduce the steep slope of the trailing edge was $(1 + 0.875 \cos \theta_R)$ for the distribution of the alpha particles with respect to the recoil direction. The dashed curves labeled 0.75 and 1.0 show the sensitivity of this trailing edge to the orientation of the recoil breakup. The higher energy portion of the spectrum is essentially unchanged by this variation. The slight upturn at low energy can be reproduced by including a small term proportional to $\cos^2 \theta_R$. The effects of the angular resolution $\Delta\theta = \pm 1^\circ$ have not been folded into the individual spectrum calculations, but the shapes of these spectra do not change rapidly enough with angle for the inclusion of this uncertainty to be important.

Figure 38 shows the results of spectrum calculations for the more backward angles, 15° and 30° , at the same energy. The calculated spectra are to be compared with the heavy line representing the experimental results. The same parameters were used for the

first stage angular distribution. At 15° a recoil orientation $(1 + 0.7 \cos\theta_R)$ is required, while at 30° the experimental distribution is best reproduced by an almost isotropic breakup in flight of the Li^5 . At these more backward angles the contribution from the (2p) reaction mode is considerably reduced.

The alpha-particle energy spectra measured at 17.87 MeV for 6° and 15° are indicated by the solid lines in Figure 39. The dashed lines give the best curves obtained by a coarse sampling of the shapes produced by various recoil orientations. The angular distribution determined for the first stage was $(1 + 0.57 \cos^2\theta)$. For the 6° spectrum the best agreement was obtained with a Li^5 breakup given by $(1 + 0.875 \cos\theta_R + 0.3 \cos^2\theta_R)$, while for the 15° spectrum the distribution giving the best shape was $(1 + 0.2 \cos\theta_R)$. For the spectrum measurements at 18 MeV, the measurements were continued with a single counter below the frequency corresponding to the He^3 scattered beam. This allowed the break in the spectrum at the lower end of the window for alpha particles from the Li^5 ground state to be observed, and this is also reproduced by the calculated shapes near an alpha-particle energy of 12 MeV. The (2p) mode of the reaction again appears very strongly forward-peaked.

In order to determine quantitatively the relative importance of the Li^5 and (2p) reaction mechanisms, several ratios are plotted in Figure 40 as a function of laboratory angle. In (a) the ratios of the heights of the individual spectra at their corresponding peak positions are given.

$$R_a(\theta) = B(\theta) g(E_{2p}, \theta) / A(\theta) f(E_{\text{Li}^5}, \theta) .$$

In (b) the ratio of the number of counts due to each mechanism is given as a function of laboratory angle.

$$R_p(\theta) = B(\theta) \int g(E, \theta) dE / A(\theta) \int f(E, \theta) dE .$$

These plots both indicate the forward-peaked nature of the (2p) reaction mechanism; the differences in the actual numbers in the two cases merely reflect the fact that the (2p) spectrum has a more prominent peak for a given area than the spectrum produced by the Li^5 mode.

The observation of the p-p final state interaction in the alpha-particle spectra at forward angles allows one to study the competition between these two reaction mechanisms in detail. Because it is so strongly forward-peaked it probably does not contribute sizeably to the total cross section measurements in the energy region between 3 and 12 MeV. (The results described in Figure 30 put a limit of 20% on the additional contributions of all other processes.) At higher energies its effects may be more important, as indicated by the low energy peaks in the proton spectrum at 18 MeV (Figure 17). At very low energies its relative importance will depend on how the various reaction mechanisms are affected by penetration factors in the incoming channel.

The change in the recoil breakup orientation with angle is not surprising, since any polarization of the recoiling Li^5 system would certainly vary with angle. The presence of the $\cos\theta_R$ term (if it indeed exists) is of considerable importance to an understanding of the reaction mechanism. Since a state of pure parity can break up

with an orientation described only by even powers of $\cos\theta_R$, the presence of an odd term would require interference with a background phase shift of the opposite parity.

C. Deuteron Spectra at 18 MeV

Above a bombarding energy of 11 MeV it is possible to produce deuterons in the final state by the reaction $\text{He}^3(\text{He}^3, d)p\text{He}^3$. An initial attempt was made at a bombarding of 12 MeV, to see if deuterons could be detected from the breakup of the 16.64 state in Li^5 . This sequential reaction has a slightly higher threshold energy (11.5 MeV) and it is not surprising that deuterons were not observed so close to threshold. When the deuteron spectrum was observed at a He^3 bombarding energy of 18 MeV, however, there was still no sign of a sequential mechanism involving the higher excited states of Li^5 . Instead the deuteron spectrum seemed to reflect a broad p-wave interaction in the residual $(p + \text{He}^3)$ system.

The momentum spectrum of deuterons is given in Figure 41 for the measurements at 17.87 MeV and laboratory angles of 6° and 15° . The spectrum at 6° rises rapidly from the three-body end point and peaks at an excitation of 1.2 MeV in the $(p + \text{He}^3)$ system, while the spectrum observed at 15° (reduced by 1/4 in the figure) has no such rapid variation. The results of several spectrum calculations which refer to the 6° curve are also given. The dashed line representing the phase space prediction bears no resemblance to the observed shape. The solid line is the result of a Watson-Migdal calculation (see Part III, B) using $(\sin^2\beta)/(\text{Penetration factor})$, where β was taken to be the "resonant" part of an unsplit, p-wave scattering phase shift from an analysis of proton- He^3 scattering (Tombrello,

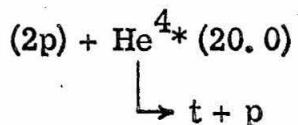
1962). This peaks about 2 MeV too high in the $(p\text{-He}^3)$ system but it can be improved (see dash-dot line) by arbitrarily including an additional $\epsilon_3 = 2$ interaction between the deuteron and the $(p\text{-He}^3)$ system. This reproduces the position of the peak and the shape of the front edge, but falls off too fast at lower deuteron energies. In any case enough parameters have been included to lead one to suspect that any agreement seen is fortuitous. The $(p + \text{He}^3)$ interaction does not appear to explain the deuteron spectrum at 18 MeV so it seems likely that the $(d + p)$ and $(d + \text{He}^3)$ interactions are also producing strong effects in this particular final state. The broad shape for the deuterons at 15° does not invalidate the suggestion that one of the peaks seen in the charge 1 spectrum at 18 MeV and 20° (see Figure 17) is due to a combination of protons and deuterons from this mechanism. The difference between an energy scale and a momentum scale can be deceiving in comparing the two figures.

D. Triton Spectrum at 20 MeV

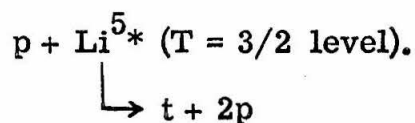
The triton spectrum from the reaction $\text{He}^3(\text{He}^3, t)3p$ was originally investigated to look for effects involving an interaction among the three protons in the final state. The possibility that this interaction might produce a prominent effect was suggested by a weak proton peak corresponding to the possible existence of a bound trineutron in the reaction $\text{H}^3(n, p)3n$ at 14.1 MeV (Ajdačić et al., 1965). This interpretation has since been questioned by observations which have set considerably smaller upper limits on the cross section for the charge symmetric reaction $\text{He}^3(p, n)3p$ (Anderson et al., 1965 and Cookson, 1966). In the present work

a triton spectrum which also probes the (3p) system is observed and its interpretation is consistent with no (3p) final-state interaction, although the region of interest is somewhat masked by a strong p-t interaction. Recent measurements of the $\text{He}^3(\text{He}^3, t)3\text{p}$ reaction at 44.1 MeV (Tombrello, 1966) also fail to see any enhancement due to a (3p) interaction. The $\text{H}^3(n, p)3n$ reaction has been examined (Thornton et al., 1966) at 20.8 MeV and no evidence is found for the existence of the trineutron.

Figure 42 shows the triton energy spectrum obtained at a He^3 bombarding energy of 19.60 MeV and a laboratory angle of 4° . The data are a combination of two experimental runs that were normalized by matching the front and back edges of each spectrum. In the top part of the figure the dashed curve represents the appropriate four-body phase space distribution (see Appendix A. 1). The triton energy spectrum rises more rapidly and peaks sharply at a triton energy of 8 MeV as opposed to 5.5 MeV for the phase space curve. The well-defined leading edge of this spectrum which extrapolates to zero 700 keV above the four-body end point is suggestive of a sequential process. Two possible candidates are:



and



In order to produce the proper end point in the later reaction the $T = 3/2$ level would have to lie between an excitation of 18.55 MeV and 18.85 MeV in Li^5 . However, taking the $t + 2n$ threshold as a lower bound for H^5 , Coulomb corrections indicate that 19.3 MeV would be a lower bound for the position of the analogue $T = 3/2$ state in Li^5 . This tends to discount the latter reaction as a possibility. The position of the upper end of the triton window shown in Figure 42 for the first reaction looks encouraging and the bottom part of the figure shows several spectrum calculations based on this reaction. The calculation of the triton spectrum from the breakup of the $\text{He}^{4*}(20.0)$ excited state can be handled easily by the recoil breakup formalism for a sharp state (see Appendix A.3). The remaining variable is the weight assigned to the various He^{4*} recoil velocities. The dashed curve weights these recoil velocities by the three-particle phase space relation. An improved spectrum shape is given by the solid curve which weights the He^{4*} recoil velocities according to the singlet p-p interaction. This curve also includes a 140 keV width for the 20.0 MeV state in the alpha particle (Parker et al., 1965). The angular resolution $\Delta\theta = \pm 1^\circ$ has not been folded into the calculations since spectrum calculations for 3° and 5° indicate that this does not change the shape significantly.

The unfortunate problem with these calculations of the triton spectrum is that, as soon as Coulomb effects are included between the He^{4*} and the (2p) system (as they must be), the spectrum drops sharply on the low energy side of the peak and only the front edge of the calculated shape remains close to the observed shape. This suggests that there are indeed more complicated effects to be considered in this spectrum calculation.

V. COINCIDENCE MEASUREMENTS

A. Experimental Procedure

In addition to the single particle measurements described in Parts III and IV, measurements of p-p and p-He⁴ coincidence spectra were made at a He³ bombarding energy of 10 MeV. In spite of the fact that these measurements have not added to our understanding of the reaction mechanism, they have been included because they confirm some aspects of it and they illustrate an alternate means for investigating reactions with more than two particles in the final state.

For a reaction with three particles in the final state there are nine independent variables required to describe the magnitude and direction of the three momenta. The four equations required by the conservation of energy and momentum reduce this to five independent variables. When two particles are measured in coincidence, three angles are specified. If the beam direction is taken as the z-axis, these are the polar angles of the two counters (θ_1 and θ_2) and the magnitude of the difference between their azimuthal angles ($|\varphi_1 - \varphi_2|$). The remaining two independent variables describe a curve giving the location of kinematically allowed events in the energy plane (E_3, E_4). A sample of this curve is given in Figure 43 for p-He⁴ coincidences. The dashed lines indicate the spread that can be expected from the angular resolution of the detectors. Points along this curve correspond to particular excitations between any two particles in the final state. In this way angles can be selected which will enhance particular final state interaction effects. If each counter measures the energies of the

particles in coincidence, the problem is overdetermined and some of the effects due to random coincidences may be eliminated. In practice, however, these are measured directly by inserting a time delay between the two counters so that only random events are recorded.

In the present measurements a small high pressure gas cell containing 1/5 to 1/2 atm. of gas was used to offset the sharp drop in counting rate produced by the coincidence requirement. This gas cell is described in Part II, B and the detector collimator that was mounted in the lucite top of the chamber to provide a second counter is shown in Figure 3. A block diagram of the electronics used is given in Figure 6b. A standard Hammner coincidence unit with a resolving time of 225 nsec was used to gate a 64×64 Nuclear Data two-dimensional analyzer. The inputs to the coincidence unit were supplied by discriminator outputs from two double-delay-line amplifiers. For p-He⁴ measurements a coincidence was required between the single counter and the ΔE counter of the counter telescope. For p-p measurements a coincidence was required between the two E counters. Since only the lower detector had a ΔE counter, the p-p measurements also include a single p-He⁴ coincidence band. The random coincidence spectrum was determined directly in each case by inserting an additional delay of 400 nsec into one side and repeating the measurements. The true coincidence counting rate for the spectrum shown in Figure 44 was approximately one count per second.

B. Summary of Results at 10 MeV

Three of the coincidence spectra obtained at 9.87 MeV are shown in Figures 44, 45 and 46. The raw coincidence counts are indicated by symbols that roughly correspond to logarithmic intervals. Arrows along the axes indicate the positions of random coincidence loci due to high He^3 counting rates in the forward detector from elastic scattering by the gas and by the gas cell foil. The kinematically allowed energies are indicated by a solid curve. The sum spectra projected onto each axis include the counts along this curve less the number of random coincidences that lay in the same region. In all cases the number of random counts that had to be subtracted was less than 10%.

Figure 44 shows the p- He^4 coincidence spectrum for $\theta_p = +100^\circ$ and $\theta_\alpha = -30^\circ$. This particular set of angles was chosen because it gave a high coincidence counting efficiency for the excitation in the (p + He^4) system corresponding to the Li^5 ground state. The prominence of this interaction is apparent both in the raw spectrum and in the sum spectra that have been projected onto the proton and alpha-particle axes.

In Figure 45 p- He^4 coincidences for $\theta_p = +90^\circ$ and $\theta_\alpha = -40^\circ$ also show the prominence of the Li^5 ground state group. In addition, the relative energy in the (2p) system remains below 100 keV on the upper branch of the allowed curve between proton energies of 3.5 and 6.0 MeV. The result is a sharp dip in the total proton yield and there is also a suggestion of peaking at 2.4 and 8.0 MeV where the p-p relative energy passes through 800 keV. (This is the p-p excitation energy corresponding to the sharp peaks in the forward angle alpha-particle spectra.) This implies that there are small

effects due to the p-p interaction even at these more backward alpha-particle angles. In the total yield projection onto the alpha-particle axis an additional peak at the high energy end illustrates the misleading effects that are produced when the allowed curve becomes perpendicular to one axis.

The results of a p-p coincidence run for symmetric angles of $\pm 45^\circ$ are shown in Figure 46. The peaking at the two ends of the p-p curve correspond to the Li^5 ground state. The number of coincidence counts is enhanced where the p- He^4 curve, produced by the single counter, intersects the p-p curve. The number of random coincidences is less than 10% in this region of the spectrum. There is little of interest occurring along the rest of the p-p curve where the excitation in the (2p) system remains fairly constant at about 11 MeV.

In the $\text{He}^3(\text{He}^3, 2p)\text{He}^4$ reaction the large energy release produces a considerable kinematic separation between the several stages of a sequential decay. This allows one to profit from single-counter spectrum measurements in studying the nature of the reaction mechanism. The measurement of coincidence spectra allows one to concentrate on a particular interaction by choosing pairs of angles at which the detection of the corresponding two-particle excitation is enhanced. However, care must be taken not to generalize about the overall importance of a particular interaction from measurements at a limited set of pairs of angles. Coincidence measurements may be a useful tool in regions of excitation where several interactions appear to overlap and exhibit interference effects, but they seem to offer no clear advantage when a particular reaction mode predominates.

VI. LOW ENERGY MEASUREMENTS

A. Experimental Procedure and Results

In an effort to extend spectrum calculation techniques to the low energy region where the value of the total reaction cross section is of astrophysical interest, energy spectra were measured at a fixed laboratory angle of 90° for He^3 bombarding energies from 5.70 MeV down to 0.28 MeV. The measurements were made in a small volume gas cell with an entrance foil of 5000- \AA Ni^0 and a He^3 gas pressure of 1/10 atm. A 2 mm surface-barrier detector was positioned at 90° behind circular defining slits which had an angular resolution (fwhm) of 13° and which viewed a 1/2 inch path length of beam. The entrance of the cell was equipped with a suppressor ring held at -300 V and the entire target body was biased at +45 V, so that consistent integrations could be made. No attempt was made to measure absolute cross sections. The thickness of the entrance foil was determined to be $(7240 \pm 750)\text{\AA}^0$ by measuring the shift in energy of the 1.07 MeV resonance in $\text{He}^4(d, d)\text{He}^4$. A knowledge of this thickness was important in determining the proper He^3 bombarding energy since the foil produced a sizeable energy loss in the incident beam (380 keV at 2 MeV).

The spectrum obtained at 0.98 MeV is shown in Figure 47. The high energy proton peak corresponding to the Li^5 ground state is still evident, but the spectrum shape has changed considerably from that shown in Figure 16 for a bombarding energy of 2.81 MeV. At this lower energy where the cross section of the $\text{He}^3 + \text{He}^3$ reaction is considerably reduced, the proton and alpha-particle groups from the reaction $\text{D}(\text{He}^3, p)\text{He}^4$ with a slight deuterium

contaminant are more pronounced. (This high energy proton group is seen above the Li^5 ground state peak and the alpha-particle group dominates the lower end of the spectrum.)

Spectrum shapes were calculated and fitted to the high energy proton peak as described in Part III, C. 2. It is evident that there is a considerable excess of counts in the mid-energy range. This excess cannot be accounted for by protons or alpha particles from the recoil breakup (as indicated by the windows in Figure 47) or by alpha particles from the contaminant reaction. The discrepancy between the observed spectrum and the predicted shape increases as one goes to lower bombarding energies, until the high energy proton peak is barely discernible. This would explain the almost smooth shape of the spectrum observed by Good *et al.*, (1954) at a bombarding energy of 0.36 MeV. A similar change in the shape of the spectrum at low bombarding energies is also observed by Dwarakanath and Winkler (1966).

The deviation of the calculated shape from the data at the midpoint of the spectrum is indicated in Figure 48 as a function of the He^3 bombarding energy. It increases rapidly below a bombarding energy of about 3 MeV, until the ratio of the observed height to the calculated height is 3.7 at 0.64 MeV, the lowest bombarding energy at which enough counts were obtained to allow a meaningful comparison. This appears to indicate a change in the dominant reaction mechanism at the low bombarding energies and it emphasizes the need to determine the shape of the entire spectrum at several angles in order to extract a reliable total cross section for the reaction.

B. Astrophysical Significance

The importance of the cross section of the $\text{He}^3 + \text{He}^3$ reaction at low energies to astrophysics has been discussed in the Introduction. Although the present work does not add to our knowledge of the cross section in the relevant low energy region, it is worthwhile to review what is known and what additional measurements are needed. At low energies a cross-section factor $S(E)$ is defined which removes the Coulomb penetration factor from the energy dependence of the observed cross section.

$$S(E) = \sigma(E) \cdot E \cdot \exp(2\pi\eta) \quad ,$$

where E is the center-of-mass energy and $\eta = Z_1 Z_2 e^2 / \hbar v$.

The behavior of $S(E)$ as a function of E is indicated in Figure 49 for the present Li^5 ground state measurements, which extend down to a center-of-mass energy of 870 keV, and for the data of Good et al., (1954) which extend down to 50 keV. The sharp upturn of their curve at low energies may indicate certain practical limitations of that experiment (e. g., beam straggle or beam energy uncertainty) and it is important that these measurements be repeated. The results of the present 90° measurements are not indicated, but after they were normalized to the counter telescope measurements above 3 MeV (laboratory energy) they were not in disagreement with the value of $S(E)$ at the minimum of Good's curve. The errors on the two lowest points were quite large and they reflected the uncertainty in the beam energy due to the 10% uncertainty in the foil thickness. The importance of a careful beam energy calibration for measurements at low energy cannot be overemphasized.

Values of $S(E)$ have also been extracted from measurements of the $\text{He}^3 + \text{T}$ reaction (Youn et al., 1961) and the $\text{T} + \text{T}$ reaction (Jarmie and Allen, 1958 and Govorov et al., 1962). The $\text{He}^3 + \text{T}$ results exhibit the same suspicious upturn seen in the $\text{He}^3 + \text{He}^3$ data. This leads one to suspect that this upturn is due to uncertainties in the beam energy and target thickness, both of which can require sizeable corrections at very low bombarding energies. The currently accepted values of $S_0 \equiv S(E=0)$ for these reactions are given below.

Reaction	S_0 (keV-barns)	Ratio
$\text{T} + \text{T} \rightarrow \text{He}^4 + 2\text{n}$	160	$\equiv 1$
$\text{He}^3 + \text{T} \rightarrow \text{He}^4 + (\text{pn or d})$	950	5.9
$\text{He}^3 + \text{He}^3 \rightarrow \text{He}^4 + 2\text{p}$	1100	6.9

If we neglect the differences due to nuclear effects in the outgoing channels and if we assume that the forces are independent of spin, then at low energy for $\ell = 0$ we can relate the Mass 3 + Mass 3 reactions as follows (Fowler, 1966):

$$\sigma_{33} \propto (1 + \delta_{12}) \cdot (\text{stat. wt.}) \cdot \left(\frac{2\pi\eta(1/v)}{\exp(2\pi\eta) - 1} \right),$$

where the first term is due to identical particles, the second term is the statistical weight which allows for the inclusion of singlet and triplet initial states, and the latter term gives the energy dependence which includes the Coulomb penetration factor (proportional to $Z_1 Z_2$).

We have the following prediction for the relative values of S_0 :

Reaction	I. P.	S. W.	$Z_1 Z_2$	Product	S_0 Ratio
T + T	2	1	1	2	1
T + He ³	1	4	2	8	4
He ³ + He ³	2	1	4	8	4

The above comparisons indicate that the current values for S_0 are in approximately the predicted proportion. An examination of the behavior of $S(E)$ (see Figure 49), however, indicates that further measurements of the He³ + T and He³ + He³ reactions are required in order to obtain more reliable estimates of S_0 .

VII. DISCUSSION OF RESULTS

The previous sections have described an investigation of the multi-particle reactions that are produced by the He^3 bombardment of He^3 below 20 MeV. While the calculations of spectrum shapes have been reasonably successful at reproducing the general features of the observed spectra, the difficulties that are associated with a detailed interpretation of the three- and four-body final states are also apparent. Below a He^3 bombarding energy of 11 MeV, the reaction $\text{He}^3(\text{He}^3, 2p)\text{He}^4$ offers an unusually good opportunity to observe the effects of two well-known two-body interactions in a three-particle final state. The large energy release ($Q = +12.86$ MeV) produces a considerable kinematic separation between the features of the energy spectra that are indicative of these interactions.

The proton energy spectra have been compared with a model for the reaction based on a sequential decay through the Li^5 ground state. It is found that over a wide range of energies and angles the basic features of the observed spectra are reproduced. While the detailed fits in the region well below the prominent high energy proton peak are far from satisfactory, it is encouraging that the cross sections derived from the Li^5 ground state model agree with measurements of the total cross section to within 20%.

The portions of the spectra where agreement is lacking correspond to regions where one might expect contributions from other processes: the $p\text{-He}^4 \delta_1^{1/2}$ interaction corresponding to the broad first excited state of Li^5 , the singlet $p\text{-p}$ interaction associated with the $\text{He}^4 + (2p)$ reaction mechanism, and direct breakup with no final-state interactions. There is little doubt that the spectrum shapes could be more adequately reproduced by including arbitrary

amounts of the broad energy spectra produced by these interactions. However, this agreement would come at the expense of ignoring the three-body nature of the problem since these are also regions where three-body effects would produce a rearrangement of particles in the final state. While these are processes that the present model completely ignores, a simple consideration will indicate that their inclusion may be necessary.

The Li^5 ground state model assumes that the first proton has no interaction (other than Coulomb) with the residual ($p + \text{He}^4$) system. For this approximation to be valid the lifetime of the Li^5 must be long compared to the time it takes the first proton to traverse a distance corresponding to the radius of the Li^5 . In the center-of-mass system the velocity of the first proton leaving Li^5 in its ground state is given by

$$v_p \simeq [(10/6)(0.5 E_{\text{He}^3} + 10.89)]^{1/2} \times 10^9 \text{ cm/sec} ,$$

the radius of the Li^5 is ~ 3 fm., the width of the ground state is 1.5 MeV, and its lifetime is given by $\tau(\text{Li}^5) \simeq \hbar/\Delta E(\text{Li}^5)$. The approximation requires $t_p \ll \tau(\text{Li}^5)$ and, at a bombarding energy of 8 MeV, we have

$$t_p = \frac{R(\text{Li}^5)}{v_p} \simeq \frac{3 \times 10^{-13} \text{ cm}}{5 \times 10^9 \text{ cm/sec}} = 6 \times 10^{-23} \text{ sec}$$

and

$$\tau(\text{Li}^5) \simeq \frac{6.6 \times 10^{-22} \text{ MeV sec}}{1.5 \text{ MeV}} = 4.4 \times 10^{-22} \text{ sec}.$$

At the center of the Li^5 ground state the ratio $t_p/\tau(\text{Li}^5) \sim 1/7$. For higher excitations in Li^5 this ratio increases and the approximation of a long-lived intermediate state is even less rigorous. This suggests that an inclusion of certain three-body effects may lead to a better understanding of the reaction mechanism. The more obvious corrections of this type are the inclusion of interference between the two identical fermions and the possibility of the re-scattering of particles in the final state. It is conceivable that coincidence measurements, which have not yet contributed to our knowledge of the reaction mechanism, could now be used to differentiate between three-body effects and those which always appear at the same excitation in either the (2p) or the (p- He^4) system.

The development of the recoil spectrum calculations has also made it possible to interpret the prominent features of the alpha-particle spectra at forward angles. Again only a simple combination of the spectrum shapes from the p-p and p- He^4 interactions has been used and a more rigorous treatment of the spectrum calculation is required. However, the simplified treatment has made it possible to recognize the presence of an angular orientation associated with the breakup of the recoiling Li^5 . This could also be verified by further coincidence measurements.

At bombarding energies above 12 MeV the complexity of the observed spectra is increased by the presence of additional reaction channels. Attempts at calculating the details of the spectrum shapes for the deuteron and triton spectra have not been particularly

successful, presumably because there is no single pair of interacting particles that dominates either final state.

The measurements of the separated spectra have produced reliable values for the total cross section from 3 to 18 MeV. The cross sections obtained with the Li^5 ground state model agree to within 20% with these total cross sections between 3 and 12 MeV. However, the shapes of the energy spectra at 90° obtained at lower bombarding energies suggest that the reaction mechanism is changing. It is worth noting that the Li^5 ground state mechanism is a complicated two-step process involving the pickup of an s-wave neutron and a p-wave proton by one of the He^3 's. This is in contrast to the $\text{He}^4 + (2p)$ mechanism which involves only one step, the transfer of an s-wave neutron. The basic difference in the two mechanisms may be related to the observed changes in the reaction mechanism at low energy.

The uncertainties about the reaction mechanism at low energy make it imperative to measure proton spectra at several angles with as low a separation energy as possible in order to extract a reliable total cross section. Measurements of the alpha-particle spectra in the same low energy region would indicate whether or not the p-p interaction can explain this apparent change in the reaction mechanism.

In the final analysis, detailed measurements of both proton and alpha-particle spectra are required to obtain a more accurate picture of the $\text{He}^3(\text{He}^3, 2p)\text{He}^4$ reaction mechanism. The present investigation has partially met this need and has provided a general understanding of the important final-state interactions over a wide range of bombarding energies. It is clear, however, that a more detailed knowledge of the low energy portion of each spectrum is

important in evaluating the applicability of any more sophisticated model of the reaction mechanism. Equally apparent is the need for a theoretical model which goes beyond the basically kinematical features of the present attempt to include the dynamical effects present in a three-particle final state.

APPENDIX A. SPECTRUM CALCULATIONS FOR MULTI-PARTICLE FINAL STATES

This appendix is intended as a summary of expressions used to calculate spectrum shapes of particles from reactions with more than two particles in the final state. For a reaction with n particles in the final state, the particles are labeled

$$1 + 2 \rightarrow 3 + 4 + 5 + \dots + (n + 2) \quad ,$$

where "1" is the bombarding particle, "2" represents the target, and "3" is taken as the detected particle in a single-counter measurement. Quantities in the center-of-mass system are labeled by a \sim (as in \tilde{E}_3), vectors are distinguished by a $\vec{\sim}$ (as in \vec{p}_3), and multiple subscripts indicate a relative energy (E_{45}), a combined mass ($M_{45} = M_4 + M_5$), or a reduced mass ($\mu_{3,45} = M_3 \cdot M_{45}/M_{345}$).

1. Phase-Space Distributions

When the matrix element for a transition from the initial to the final state is a constant, the energy spectrum of each particle is proportional to a factor describing the number of states available to the particle per unit energy interval in the final state. Non-relativistic expressions for these phase-space distributions are described in the center-of-mass system where their simplicity is explicit.

For an n -particle final state the conservation of momentum and energy require that

$$\tilde{p}_3 + \tilde{p}_4 + \tilde{p}_5 + \dots + \tilde{p}_{n+2} = 0 ,$$

and

$$\tilde{E}_3 + \tilde{E}_4 + \tilde{E}_5 + \dots + \tilde{E}_{n+2} = E_T ,$$

where $E_T = M_2 E_1 / M_T + Q$ is the energy available in the center-of-mass system, E_1 is the laboratory bombarding energy, Q is the reaction Q -value and $M_T = M_1 + M_2$. The general form of the phase-space distribution for a measurement of the energy spectrum of a single particle is (Zupančič, 1964)

$$(d\tilde{N}) \propto d^3 \tilde{p}_3 \int \delta(E_T - \sum_3^{n+2} \tilde{E}_i) \delta^3(\sum_3^{n+2} \tilde{p}_i) \prod_4^{n+2} d^3 \tilde{p}_i .$$

For this general case we get

$$\left(\frac{\partial^2 \sigma}{\partial E_3 \partial \Omega_3} \right) \propto (\tilde{E}_3)^{1/2} \left(E_T - \frac{M_T}{M_T - M_3} \tilde{E}_3 \right)^{(3n/2 - 4)} ,$$

which gives for 3- and 4-particle final states, respectively,

$$\propto (\tilde{E}_3)^{1/2} \left(E_T - \frac{M_T}{M_T - M_3} \tilde{E}_3 \right)^{1/2}$$

and

$$\propto (\tilde{E}_3)^{1/2} \left(E_T - \frac{M_T}{M_T - M_3} \tilde{E}_3 \right)^2 .$$

The second term in these relations, $\left(E_T - \frac{M_T}{M_T - M_3} \tilde{E}_3 \right)$, is proportional to the relative energy of the undetected particles.

These expressions can be transformed to the laboratory system using the invariant quantity (Williams, 1961)

$$\frac{1}{\sqrt{\tilde{E}_3}} \left(\frac{\partial^2 \sigma}{\partial E_3 \partial \Omega_3} \right) = \frac{1}{\sqrt{E_3}} \left(\frac{\partial^2 \sigma}{\partial E_3 \partial \Omega_3} \right)$$

and the law of cosines to relate the velocity of particle 3 in the two systems. The latter gives the quadratic expression for the laboratory energy E_3 in terms of θ_3 and \tilde{E}_3 ,

$$E_3 - \frac{2 \cos \theta_3}{(M_1 + M_2)} (M_1 E_1 M_3 E_3)^{1/2} + \frac{M_1 M_3}{(M_1 + M_2)^2} E_1 - \tilde{E}_3 = 0 ,$$

which is double-valued when the center-of-mass motion is sufficient to carry all particles forward in the laboratory system. As was indicated in Part III, B, the phase-space factor can be modified to include a Coulomb interaction with relative orbital angular momentum ℓ_3 by replacing the factor $(\tilde{E}_3)^{1/2}$;

$$(\tilde{E}_3)^{1/2} \rightarrow (\tilde{E}_3)^{1/2} (\tilde{E}_3)^{l_3} \frac{2\pi\tilde{\eta}_3}{\exp(2\pi\tilde{\eta}_3)-1} \prod_{t=1}^{l_3} \left(1 + \frac{\tilde{\eta}_3^2}{t^2}\right),$$

where $\tilde{\eta}_3$ is the usual Coulomb parameter, $Z_1 Z_2 e^2 / \hbar \tilde{v}_3$, defined for the relative motion of particle 3 and the residual system.

For a reaction with three particles in the final state, the phase-space distribution for a measurement of two particles in coincidence has the same functional form in both systems,

$$\frac{\partial^4 \sigma}{\partial E_3 \partial \Omega_3 \partial E_4 \partial \Omega_4} \propto (E_3)^{1/2} (E_4)^{1/2},$$

where the allowed values of (E_3, E_4) are those which satisfy the equation (see Figure 43),

$$E_1 + Q = E_3 + E_4 + \frac{(p_1 - p_3 - p_4)^2}{2M_5}.$$

The phase-space population per unit length of the allowed curve is proportional to

$$\frac{(E_3)^{1/2} (E_4)^{1/2}}{\left[\left(1 - \frac{\tilde{v}_3 \cdot \tilde{v}_5}{v_3^2}\right)^2 + \left(1 - \frac{\tilde{v}_4 \cdot \tilde{v}_5}{v_4^2}\right)^2 \right]^{1/2}},$$

whereas, if the coincidence measurements are projected onto the E_4 axis, the phase-space distribution is given by

$$\frac{\partial^3 \sigma}{\partial E_3 \partial \Omega_3 \partial \Omega_4} \propto \frac{(E_3)^{1/2} (E_4)^{1/2}}{\left| 1 - \frac{v_4 \cdot v_5}{2v_4} \right|} .$$

This expression is singular at the turning point of the allowed distribution, but in practice this effect is washed out by the finite solid angles of the two detectors.

In the present investigation, the presence of strong two-body interactions in the final state cause the observed spectra to deviate markedly from the phase-space distribution. This is seen in curve D of Figure 10 for the proton spectrum from $\text{He}^3(\text{He}^3, 2p)\text{He}^4$, in Figure 41 for deuterons from $\text{He}^3(\text{He}^3, d)p\text{He}^3$, and in Figure 42 for the triton spectrum from $\text{He}^3(\text{He}^3, t)3p$.

2. Spectrum of the Non-Interacting Particle

A sequential decay is characterized by an enhanced counting rate at points in the energy spectra corresponding to a particular relative energy for a pair of particles. In a three-particle final state the most prominent indication of a two-particle interaction is in the energy spectrum of the other particle, "3", which is assumed to experience no interaction with the "4-5" system. If this interaction is specified by a weighting function $f(p_{45})$, then the center-of-mass energy spectrum of particle 3 is given by

$$\widetilde{\left(\frac{\partial^2 \sigma}{\partial E_3 \partial \Omega_3} \right)} \propto (\tilde{E}_3)^{1/2} \iint f(\underline{p}_{45}) \delta(\tilde{p}_3 + \tilde{p}_4 + \tilde{p}_5) \delta(E_T - \tilde{E}_3 - \tilde{E}_4 - \tilde{E}_5) d^3 \tilde{p}_4 d^3 \tilde{p}_5 .$$

Moreover, if $f(\underline{p}_{45})$ can be factored into the form

$$f(\underline{p}_{45}) = f(p_{45}) \cdot A(\tilde{\theta}_3) \cdot B(\theta_R) ,$$

where $A(\tilde{\theta}_3)$ gives the angular dependence of the center-of-mass cross section for particle 3 and $B(\theta_R)$ is the normalized angular orientation of the breakup of the (4-5) system; then the above integral simplifies and it can be shown quite generally that the energy spectrum of particle 3 is given by

$$\widetilde{\left(\frac{\partial^2 \sigma}{\partial E_3 \partial \Omega_3} \right)} \propto (\tilde{E}_3)^{1/2} \cdot A(\tilde{\theta}_3) \cdot f(p_{45}) .$$

This becomes, in the laboratory system,

$$\frac{\partial^2 \sigma}{\partial E_3 \partial \Omega_3} \propto (E_3)^{1/2} \cdot A(\tilde{\theta}_3(E_3, \theta_3)) \cdot f(p_{45}(E_3, \theta_3)) .$$

This is the factored form described in Part III, B where $f(p_{45})$ was given by the spectral measure function or was approximated in the Watson-Migdal formalism by the value of the scattering cross section for particles 4 and 5 at the appropriate relative momentum,

$$\frac{\partial^2 \sigma}{\partial E_3 \partial \Omega_3} \approx (E_3)^{1/2} \cdot (E_{45})^{1/2} \cdot \sigma_{45}(p_{45}) .$$

The form of this approximation has been given in Part III, B in terms of the dependence on a particular resonant phase shift or on a single-level parametrization. In the case of the p-p interaction a description in terms of the effective range formalism is more appropriate. In the laboratory system this has the form (Tombrello and Bacher, 1965),

$$\frac{\partial^2 \sigma}{\partial E_3 \partial \Omega_3} \approx \frac{(E_3)^{1/2} (E_{45})^{1/2} A(\tilde{\theta}_3(E_3, \theta_3)) C(\eta_{45})}{\left[-\frac{1}{a} + \frac{r_0 k_{45}^2}{2} - \frac{h(\eta_{45})}{R} - P r_0^3 k_{45}^4 \right]^2 + C^2(\eta_{45}) k_{45}^2} ,$$

where $C(\eta) = 2\pi\eta / (\exp(2\pi\eta) - 1)$,

$$h(\eta) = \eta^2 \sum_{n=1}^{\infty} \frac{1}{n(n^2 + \eta^2)} - \ln \eta - 0.57722 ,$$

and a , r_0 , P and R are the effective range parameters for the 1S_0 p-p phase shift. For the p-p spectrum calculations the function $A(\tilde{\theta}_3)$ was assumed constant since $\tilde{\theta}_3$ does not change significantly over the region of interest in E_3 . For the calculations of the proton spectra this variation of $A(\tilde{\theta}_3)$ at a fixed laboratory angle θ_3 was included.

The formalism for predicting the shape of the spectrum of the non-interacting particle has been applied to the high energy

proton group from the Li^5 ground state transition (see Figure 10), to the forward-angle alpha-particle spectra where the p-p interaction is evident (Figures 32 - 38) and with less success to the deuteron spectrum from $\text{He}^3(\text{He}^3, d)\text{pHe}^3$ (Figure 41).

3. Recoil Breakup Spectrum in Sequential Reactions

From the assumptions of a sequential decay, it is also possible to calculate the energy spectrum of one of the particles produced by the breakup of the interacting (4-5) system. As is indicated in Figure 50, contributions to the recoil spectrum at a fixed laboratory angle θ_L come from many center-of-mass angles both for the recoil direction θ_{CM} and for the breakup angle θ_R with respect to the recoil axis. For a sharp intermediate state (defined by Q_1 , the Q-value for the first stage) all combinations of angles must be summed over for which the vectors add to give a particle at the fixed angle θ_L .

$$\underline{V}_L(\theta_L) = \underline{V}_{CM} + \underline{V}_{REC}(Q_1, \theta_{CM}) + \underline{V}_{RB}(Q_2, \theta_R) .$$

Straightforward vector addition arguments give the maximum and minimum allowed values for \underline{V}_L .

The shape of the resulting spectrum has been given in closed form previously (Morinigo, 1963; pages 63-71) and the present generalization to a broad intermediate level is made by considering a weighted sum of the spectrum shapes produced by many sharp levels. The calculation of these shapes is reviewed in order to enumerate the assumptions implicit in the treatment.

For the determination of the recoil spectrum of particle 4 for a sharp intermediate state, we have;

Q_1 = the Q-value of the first stage,

Q_2 = the Q-value of the second stage,

Q = $Q_1 + Q_2$ = the Q-value for the final state,

E_T = $M_2 E_1 / M_T + Q_1$ = the energy available in the first center-of-mass system,

$V_{CM} = (2M_1 E_1 / M_T)^{1/2}$ = the center-of-mass velocity,

$V_{REC} = (2M_3 E_T / M_{45} M_T)^{1/2}$ = the velocity of the recoil particle,

and $V_{4R} = (2M_5 Q_2 / M_4 (M_4 + M_5))^{1/2}$ = the velocity of particle 4 with respect to the recoil particle.

We also assume that the angular distribution of the center-of-mass cross section for the first stage is given by,

$$W_1(\tilde{\theta}_3) = W_1(1 + \alpha \cos \tilde{\theta}_3 + \beta \cos^2 \tilde{\theta}_3 + \gamma \cos^3 \tilde{\theta}_3 + \dots) ,$$

where W_1 is the differential cross section; and that the normalized angular distribution for the recoil breakup is given by $W_2(\theta_R)$, where $W_2(\theta_R)$ is normalized to 1 over the entire sphere. $W_2(\theta_R)$ is assumed to be independent of φ (no spin polarization).

We have, for the recoil spectrum in the laboratory system from a sharp state (following Morinigo, 1963),

$$\frac{\partial^2 \sigma}{\partial E_4 \partial \Omega_4} = \frac{2\pi W_1}{M_4(-a)^{1/2}} \cdot W_2(y_0) \cdot \frac{V_4}{(V_{\text{REC}})(V_{4R})} [I_0 + I_1 \alpha + I_2 \beta + I_3 \gamma + \dots],$$

$$\equiv S(E_4, \theta_4, Q_1, Q_2)$$

where

$$a = -(V_4^2 + V_{\text{CM}}^2 - 2V_4 V_{\text{CM}} \cos \theta_4),$$

$$b = \left(\frac{V_4 \cos \theta_4 - V_{\text{CM}}}{V_{\text{REC}}} \right) (V_4^2 + V_{\text{CM}}^2 + V_{\text{REC}}^2 - V_{4R}^2 - 2V_4 V_{\text{CM}} \cos \theta_4),$$

$$c = V_{4R}^2 (1 - y_0^2) - (V_4 \cos \theta_4 - V_{\text{CM}})^2,$$

$$y_0 = \frac{1}{2V_{\text{REC}} V_{4R}} (V_4^2 + V_{\text{CM}}^2 - V_{\text{REC}}^2 - V_{4R}^2 - 2V_{\text{CM}} V_4 \cos \theta_4),$$

$$I_0 = 1, I_1 = \left(-\frac{b}{2a}\right), I_2 = \frac{(3b^2 - 4ac)}{8a^2},$$

$$I_3 = \left(\frac{3bc}{4a^2} - \frac{5b^3}{16a^3} \right),$$

and

$$I_n = -\frac{b(2n-1)}{2an} I_{n-1} - \frac{c(n-1)}{an} I_{n-2} .$$

In order to generalize this spectrum shape to include a broad level we must assume that the angular distributions, which are for a particular excitation in the (4-5) system, apply equally for any excitation; $W_1(\tilde{\theta}_3, Q_1) = W_1(\tilde{\theta}_3)$ and $W_2(\theta_R, Q_2) = W_2(\theta_R)$. If we represent the weighting function for excitations in the 4-5 system by $F(Q_2)(\tilde{E}_3)^{1/2}$, then the recoil spectrum for a broad level is given by,

$$\frac{\partial^2 \sigma}{\partial E_4 \partial \Omega_4} = \int S(E_4, \theta_4, Q_1, Q_2) F(Q_2)(\tilde{E}_3)^{1/2} dQ_2 ,$$

where

$$\int F(Q_2)(\tilde{E}_3)^{1/2} dQ_2 = 1$$

gives the normalization. In practice this is computed by choosing a value of Q_2 , determining what values of E_4 are allowed, stepping through the allowed E_4 values in a predetermined mesh size calculating the contribution to the spectrum for each step, and then incrementing Q_2 until all allowed excitations have been included.

The above approach is general in that any weighting function may be used for $F(Q_2)$. In the lower half of Figure 50 the recoil proton spectrum is indicated for 7.95 MeV and 20° . Both curves are for the spectral measure function and are included to indicate

the sensitivity of the recoil spectrum to the Coulomb interaction with $\ell_3 = 1$ for the first stage. The horizontal lines are included to illustrate how the regions of the spectrum at this fixed laboratory angle are composed of contributions from different excitations in the recoiling Li^5 system. For the calculations of the proton and alpha-particle recoil spectra, $W_1(\tilde{\theta}_3)$ has been determined by fitting the high energy proton peak corresponding to the Li^5 ground state reaction mode.

For the calculations of the triton spectrum in Figure 42 a slightly different procedure was used because of the four-particle final state. The triton energy spectrum was determined from the breakup in flight of the $\text{He}^{4*}(20.0)$ after the recoil velocities of the $\text{He}^{4*}(20.0)$ were weighted by 1) the three-particle phase-space distribution for $p + p + \text{He}^{4*}$ and 2) the 1S_0 p-p interaction representing the mechanism $(2p) + \text{He}^{4*}$. For the latter case the spectrum calculation also included an integration over a 140 keV width for the $\text{He}^{4*}(20.0)$ state to obtain the predicted shape.

REFERENCES

1. Ajdačić, V., Cerineo, M., Lalović, B., Paić, G., Šlaus, I. and Tomaš, P., Phys. Rev. Letters 12, 444 (1965).
2. Aldridge, J. P., Wildenthal, B. H. and Youngblood, D. H., Rev. Mod. Phys. 37, 430 (1965).
3. Andersen, J. D., Wong, C., McClure, J. W. and Pohl, B. A., Phys. Rev. Letters 15, 66 (1965).
4. Bacher, A. D., Bull. Am. Phys. Soc. 8, 597 (1963).
5. Bacher, A. D. and Tombrello, T. A., Bull. Am. Phys. Soc. 10, 423 (1965); Rev. Mod. Phys. 37, 433 (1965a).
6. Barnard, A.C.L., Jones, C. M. and Weil, J. L., Nucl. Phys. 50, 604 (1964).
7. Blackmore, E. W. and Warren, J. B., Phys. Rev. Letters 16, 520 (1966).
8. Cocke, C. L., private communication (1965).
9. Cookson, J. A., Phys. Letters 22, 612 (1966).
10. Demirlioglu, D. and Whaling, W., unpublished compilation of proton stopping cross sections (1962).
11. Dwarakanath, M. and Winkler, H., private communication (1966).
12. Fermi, E., Elementary Particles, Yale University Press, New Haven, Conn., pp. 58-64 (1951).
13. Fowler, W. A., Phys. Rev. 81, 655 (1951); private communication (1966).

14. Gel'fand, I. M. and Levitan, B. M., *Izv. Acad. Nauk SSSR, Math. Ser.* 15, 309 (1951).
15. Gillespie, J., Final-State Interactions, Holden-Day, Inc., San Francisco, Calif. (1964).
16. Good, W. M., Kunz, W. E. and Moak, C. D., *Phys. Rev.* 94, 87 (1954).
17. Goodman, C. D., editor, "Conference on Correlations of Particles Emitted in Nuclear Reactions", *Rev. Mod. Phys.* 37, 327 (1965).
18. Govorov, A. M., Ka-Yeng, Li, Osetinskii, G. M., Salatskii, V. I., and Sizov, I. V., *JETP* 15, 266 (1962).
19. Jarmie, N. and Allen, R. C., *Phys. Rev.* 111, 1121 (1958).
20. Lane, A. M. and Thomas, R. G., *Rev. Mod. Phys.* 30, 257 (1958).
21. Lauritsen, T. and Ajzenberg-Selove, F., *Nucl. Phys.* 78, 1 (1966).
22. Migdal, A. B., *JETP* 1, 2 (1955).
23. Morinigo, F. B., Ph.D. Thesis, California Institute of Technology (1963).
24. Newton, R. G., *J. Math. Phys.* 1, 319 (1960).
25. Parker, P.D.M., Ph.D. Thesis, California Institute of Technology (1963).
26. Parker, P.D., Bahcall, J. N. and Fowler, W. A., *Ap. J.* 139, 602 (1964).

27. Parker, P.D., Donovan, P.F., Kane, J.V. and Mollenauer, J. F., Phys. Rev. Letters 14, 15 (1965).
28. Pearson, J. D., Ph.D. Thesis, California Institute of Technology (1963).
29. Robertson, L.P., White, B.L. and Erdman, K.L., Rev. Sci. Inst. 32, 1405 (1961).
30. Rogers, E.J., Rev. Sci. Inst. 34, 660 (1963).
31. Rose, P.H., Wittkower, A.B., Bastide, R.B. and Gale, A.J., Rev. Sci. Instr. 32, 568 (1961).
32. Schatzman, E., Compt. rend. 232, 1740 (1951).
33. Senhouse, L.S., Ph.D. Thesis, California Institute of Technology, (1964).
34. Silverstein, E. A., Nucl. Inst. and Meth. 4, 53 (1959).
35. Thornton, S.T., Jones, C.M., Bair, J.K. and Willard, H.B., International Conference on Nuclear Physics, Gatlinburg, Tennessee, contributed paper 9.6 (1966).
36. Tombrello, T.A., Nucl. Phys. 39, 541 (1962).
Bull. Am. Phys. Soc. 9, 704 (1964).
Private communication (1965).
Private communication (1966).
37. Tombrello, T.A. and Bacher, A.D., Phys. Rev. 130, 1108 (1963); Phys. Letters 17, 37 (1965).
38. Tombrello, T.A. and Senhouse, L.S., Phys. Rev. 129, 2252 (1963).

39. Watson, K. M., Phys. Rev. 88, 1163 (1952).
40. Whaling, W., Handbuch der Physik 34, 193 (1958).
41. Williams, W. S. C., An Introduction to Elementary Particles, Academic Press, New York, N. Y., pp. 356-378 (1961).
42. Youn, Li Ga, Osetinskii, G. M., Sodnom, N., Govorov, A. M., Sizov, I. V. and Salatskii, V. I., JETP 12, 163 (1961).
43. Zupančič, Č., Hercegnovi Lectures, Volume II, pages 1-64 (1964).
44. Zurmühle, R. W., Nucl. Phys. 72, 225 (1965).

TABLE I
Detector Collimator Parameters

The measured values of the parameters describing the detector collimators used in conjunction with the 30-cm gas scattering chamber are presented. See Figure 5 for an explanation of the symbols. Since the front and rear slit widths are not precisely equal we use their mean width in determining

$$\theta_{1/2} = 2 \tan^{-1} \left(\frac{2b_1 + 2b_2}{4h} \right)$$

To lowest order the "G factor" is given by

$$G = G_0 / \sin \theta \text{ with } G_0 = \frac{4b_1 b_2 \ell}{R_0 h}$$

The quantity Δ gives the maximum percentage change in G_0 (for the angular range $15^\circ \leq \theta \leq 165^\circ$) for the second order terms described in the text. Note that its maximum effect is less than the error quoted in the determination of G_0 . For additional details see pages 9-12 and 18.

TABLE I

Detector Collimator Parameters

Parameter	Description	Two Counter Telescope	Top Counter Collimator
$2b_1$	front slit width	0.2524 ± 0.0004 cm	0.2570 ± 0.0005 cm
$2b_2$	rear slit width	0.2548 ± 0.0004 cm	0.2568 ± 0.0005 cm
l	rear slit height	0.7209 ± 0.0004 cm	0.7657 ± 0.001 cm
h	slit separation	4.061 ± 0.001 cm	4.0655 ± 0.0005 cm
R_0	rear slit to center of chamber	8.423 ± 0.001 cm	8.3736 ± 0.0012 cm ∞
$\theta_{1/2}$	angular resolution	3.57°	3.62°
G_0	first order "G factor"	1.356×10^{-3} cm $\pm 0.23\%$	1.484×10^{-3} cm $\pm 0.29\%$
Δ	effect of second order terms	0.22%	0.23%
	precision of θ	$\pm 0.1^\circ$	$\pm 0.15^\circ$
	size of anti-scattering slit 2.5 cm behind front slit	0.5 cm \times 0.7 cm	0.5 cm \times 0.7 cm

TABLE II
Systematic Errors (%)

The systematic errors associated with the experimental configuration are indicated. In general the cumulative effect of these errors is small compared with the statistical uncertainty in the yield of a given experimental spectrum.

Other errors listed separately include: the uncertainty in the channel-to-energy conversion (this varied for the different bombarding energies), the absolute normalization to the $\text{He}^3 + \text{He}^3$ elastic scattering and the uncertainty involved in fitting the spectrum with a shape calculated on the basis of a particular reaction mechanism.

For further discussion see pages 9, 14-19 and 42.

TABLE II

Systematic Errors (in %)

Quantity	30-cm Chamber	High Pressure Cell
Geometry	0.3	0.3
Beam integration	0.5	1.5, 0.5 (18 MeV)
Target pressure	0.4	1.0, 0.5 (18 MeV)
Absolute temperature	0.3	0.6
Gas impurities	0.4	< 1
Angle dependent quantities	< 1	< 1
Beam heating	-	< 1
Cumulative Error	< 1.3	< 2.6, < 2.0 (18 MeV)

Other Errors

Channel-to-energy conversion	0.4 - 1.0	0.5 - 2.0
Absolute normalization	5	10
Spectrum calculation	10	10

TABLE III

Angular Distribution Parameters

The ratio of Legendre polynomial coefficients a_2/a_0 is given for the data with separated proton spectra. The coefficients are derived from a least squares fitting of the function $a_0 + a_2 P_2(\cos\tilde{\theta})$ to the center-of-mass angular distributions for $\tilde{\theta} \geq 90^\circ$. The errors are the resultant of the relative errors assigned to each of the points of the angular distribution. The value of β is also given for the angular distribution expressed in powers of $\cos\tilde{\theta}$; $1 + \beta \cos^2\tilde{\theta}$. Below 10 MeV the average value of a_2/a_0 is -0.175 and of β is -0.24. For further details see pages 36, 40 and 49.

Energy (MeV)	a_2/a_0	β
2.81	-0.205 ± 0.022	-0.28 ± 0.03
4.35	-0.136 ± 0.022	-0.19 ± 0.03
5.92	-0.180 ± 0.021	-0.25 ± 0.03
7.95	-0.153 ± 0.032	-0.21 ± 0.04
9.94	-0.201 ± 0.035	-0.27 ± 0.05
11.93	-0.090 ± 0.037	-0.13 ± 0.06
13.81	-0.028 ± 0.040	-0.04 ± 0.06
15.55	$+0.026 \pm 0.048$	$+0.04 \pm 0.07$
18.01	$+0.320 \pm 0.079$	$+0.57 \pm 0.18$

TABLE IV
Total Cross Sections

The total cross sections are given for the measurements based on separated spectra and on unseparated spectra. These were obtained by making a least squares fit of a Legendre polynomial expansion to the measured angular distributions. The error assigned is determined from the relative errors of each of the points in the angular distribution. The uncertainty in the absolute normalization has not been included and the Li^5 ground state cross sections do not include the uncertainty in the spectrum calculation. In determining the total cross sections for producing charge 1 particles in the final state, the integrated yield has been divided by 2 (two charge 1 particles are produced in each reaction).

For further details see Figures 24 and 29 and pages 41 and 44.

TABLE IV
Total Cross Sections

A. Separated Spectra

Energy (MeV)	Cross Section (millibarns)		Separation Energy (MeV)
	Li ⁵ Ground State	Charge 1 Particles	
2.81	39.5 ± 0.5	48.8 ± 2.4	2.0
4.35	69.0 ± 0.5	79.1 ± 3.1	2.0
5.92	93.6 ± 1.0	103.9 ± 4.2	2.0
7.95	104.6 ± 0.9	120.3 ± 4.2	1.9
9.94	109.0 ± 1.0	138.2 ± 5.0	2.2
11.93	105.6 ± 1.0	128.1 ± 4.0	2.1
13.81	111.7 ± 1.2	147.3 ± 6.2	2.8
15.55	120.0 ± 1.3	169.1 ± 6.0	2.5
18.01	128.9 ± 2.4	315 ± 15	2.9

B. Unseparated Spectra

Energy (MeV)	Cross Section (millibarns)	
	Li ⁵ Gnd State	
1.75	16.1 ± 0.9	
1.85	20.2 ± 1.4	
2.81	40.0 ± 0.6	
3.83	62.7 ± 0.7	
4.91	75.9 ± 0.9	
5.88	93.6 ± 1.1	
7.91	108.4 ± 1.1	
9.93	110.2 ± 1.5	
11.93	108.8 ± 1.8	

TABLE V

Cross Section Ratios

The ratio of the total cross section for the production of charge 1 particles to the cross section derived from the Li^5 ground state model is given for the measurements where separated spectra were obtained. The errors given include only the relative errors of each measurement (as in Table IV). This is determined mainly by the uncertainties assigned to the extrapolations of the separated proton spectra to zero energy. The average value for the points below 12 MeV is 1.19. See Figure 30 and page 45.

Energy (MeV)	Ratio (Ch 1/ Li^5)
2.81	1.24 ± 0.06
4.35	1.15 ± 0.05
5.92	1.11 ± 0.05
7.95	1.15 ± 0.04
9.94	1.27 ± 0.05
11.93	1.21 ± 0.04
13.81	1.32 ± 0.06
15.55	1.43 ± 0.05
18.01	2.44 ± 0.13

FIGURE 1

Composite Energy Level Diagram

The energy levels of Li^5 and Be^6 are shown together to illustrate the scale of energies involved in the present work. The energies of excited states are given in MeV relative to the corresponding ground state. At the left the positions of the Li^5 and Be^6 ground states, as well as the positions of relevant reaction thresholds, are indicated in MeV relative to $(\text{He}^4 + 2p)$.

The $3/2^-$ ground state of Li^5 has a full width of about 1.5 MeV and the broad $1/2^-$ first excited state near 4 MeV excitation has a full width of about 4 MeV. The broad structure in Be^6 at about 24 MeV is observed as an anomaly in the $\text{He}^3 + \text{He}^3$ elastic scattering (Bacher and Tombrello, 1965) and appears to have a width exceeding 5 MeV.

The level positions are taken from the latest compilation of Lauritsen and Ajzenberg-Selove (1966). For further discussion see pages 2, 34 and 38.

FIGURE 2
30-cm Scattering Chamber

A side view of the 30-cm gas scattering chamber is shown with the collimator for the counter telescope positioned at 0° . Parts of interest include:

- A entrance foil holder
- B beam collimator
- C counter collimator
- D counter telescope
- E exit foil holder
- F Faraday Cup

For additional details see pages 7 and 12.

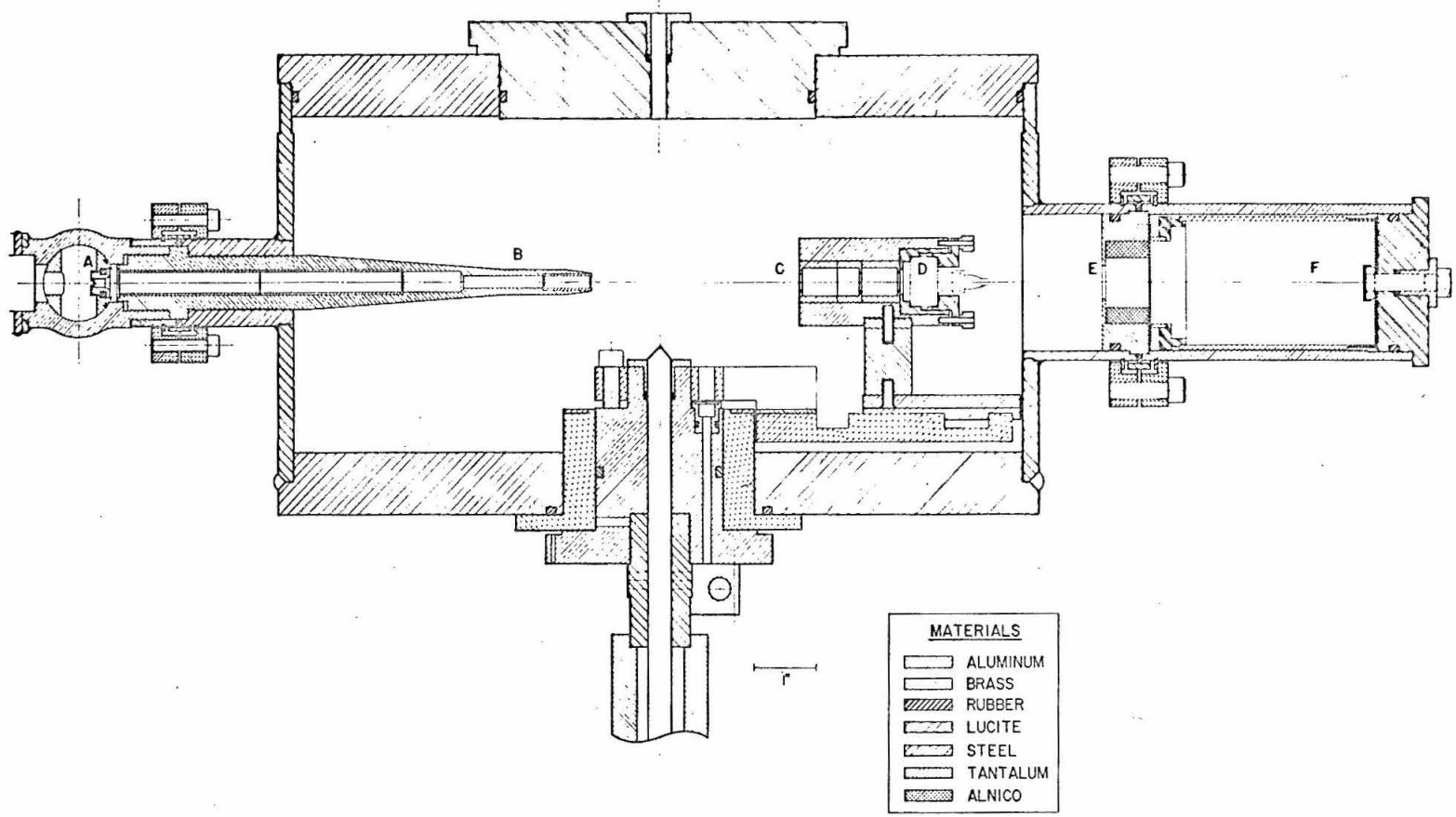
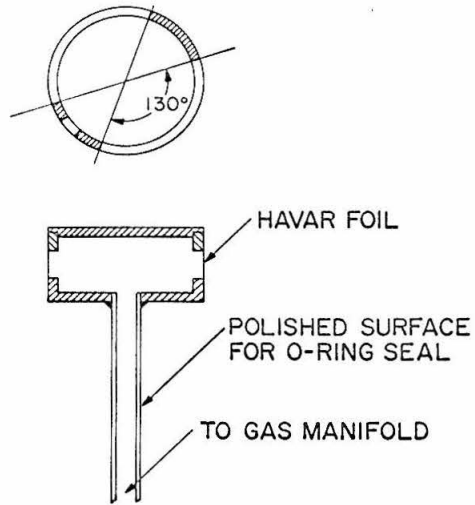


FIGURE 3
Gas Cell and Top Collimator

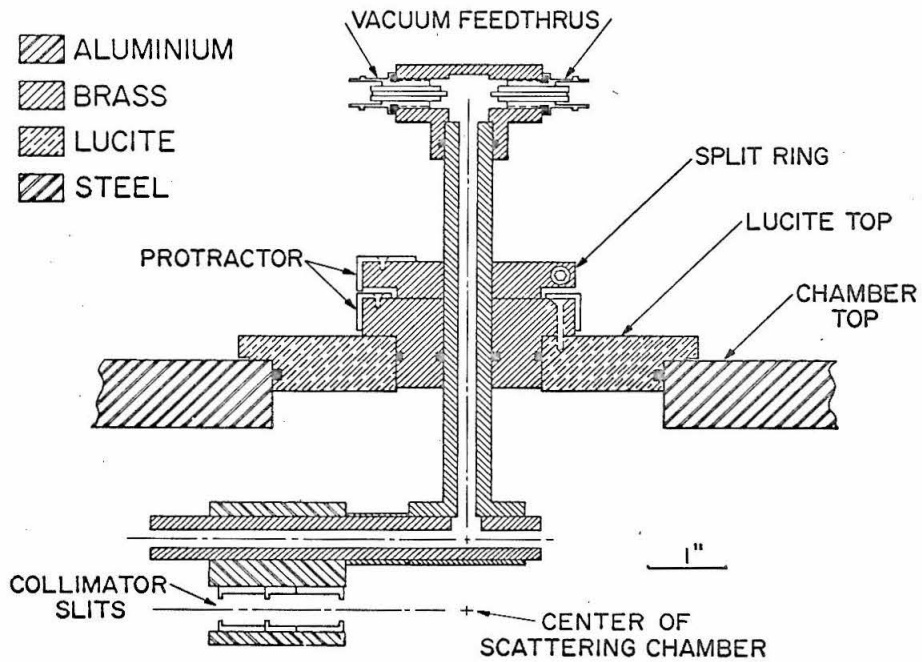
Part a) of this figure shows one of the gas cells used in the portions of this work that required a high pressure target. This particular gas cell had 0.1 mil Havar foils mounted with epoxy over the two 130° openings and 1/6 mil Mylar covering the small 1/4" hole. The cell was mounted in the bottom center-hole of the 30-cm scattering chamber and positioned so that the He^3 beam passed into and out of the cell through the Havar foils.

Part b) of this figure shows the top collimator mounted in the lucite plug in the top of the 30-cm scattering chamber. This was used in conjunction with the telescope collimator and a high pressure gas cell for the coincidence studies. The counter slit system was positioned for height and the protractor zero determined by establishing an optical axis between the last slit of the beam collimator and the center of the Faraday cup port with a surveyor's transit.

For further details see pages 12, 14 and 58.



(a) HIGH PRESSURE GAS CELL



(b) COLLIMATOR FOR TOP COUNTER

FIGURE 4

Gas Target For 61-cm Spectrometer

The gas target for use with the 61-cm magnetic spectrometer is shown in the spectrometer target chamber with the magnet positioned at 0° . Features indicated include; 1/4" slot for the beam entrance window, the gas target volume, the front slit of the exit collimator, and the exit window leading to the spectrometer. The spectrometer entrance slits define the rear aperture for the exit collimator. See text pages 20 and 21.

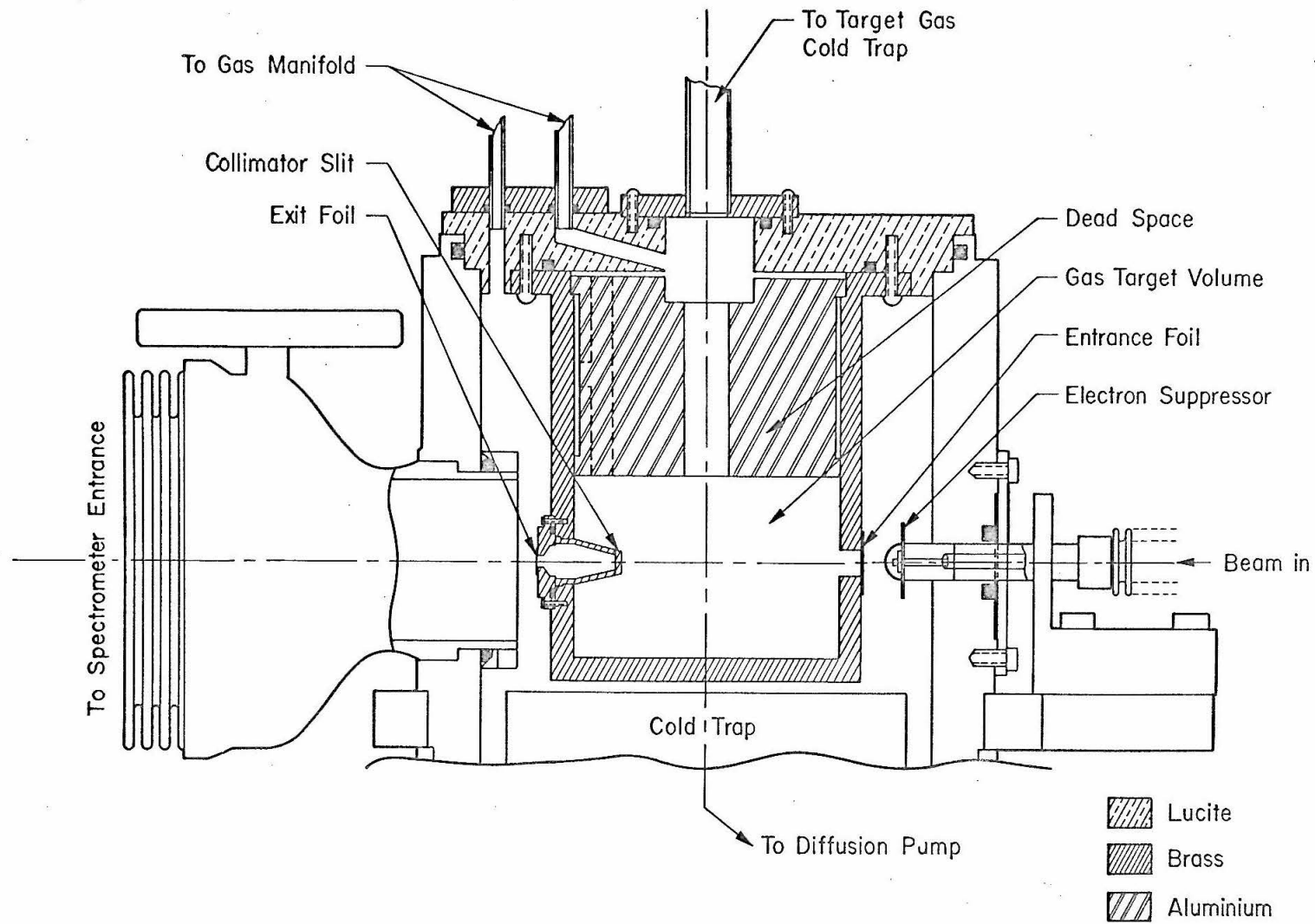


FIGURE 5
Gas Target Geometry

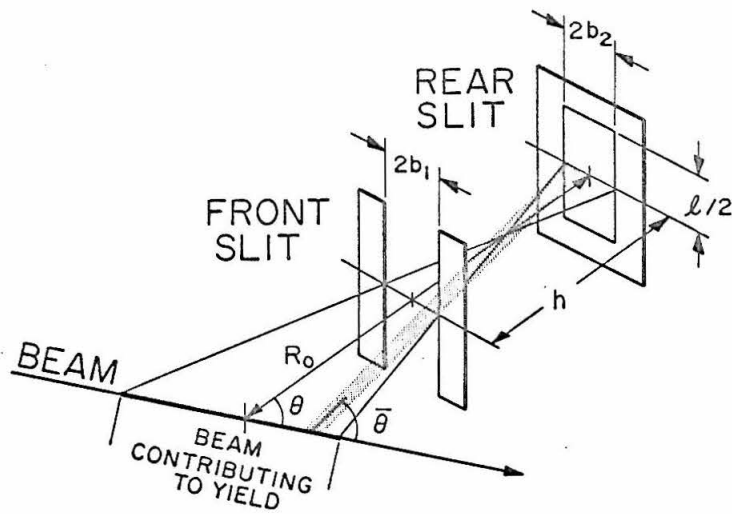
Part a) This diagram defines the slit geometry for the detector collimator in a gas target. The total length of beam contributing to the yield is indicated. The intersection of this length with the shaded region shows the length of beam seen for the reaction angle $\bar{\theta}$ (here $\bar{\theta} > \theta$).

Part b) At a given angle θ the particle detector actually sees events for a spread of reaction angles $\bar{\theta}$. For a collimator with equal slit widths ($2b = 2b_1 = 2b_2$) we can express the beam length detected by

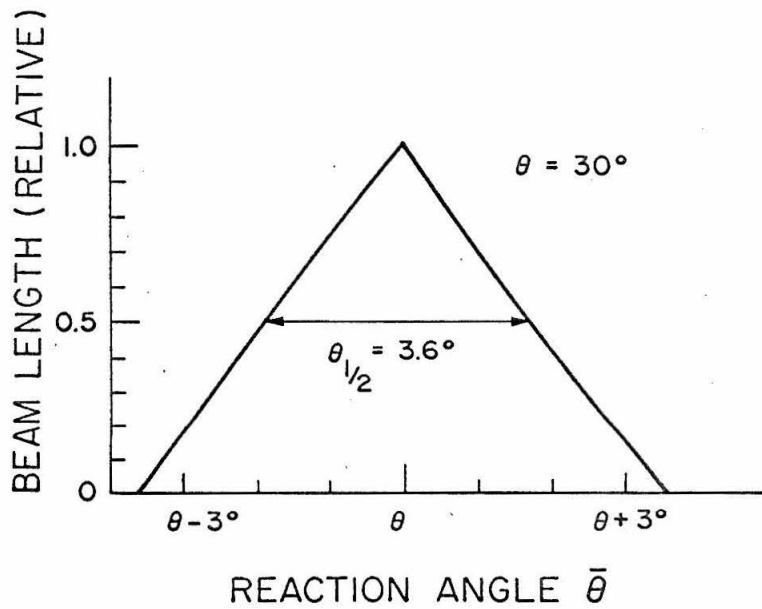
$$L(\bar{\theta}, \theta) = (2b - h \tan |\bar{\theta} - \theta|) \frac{\cos(\bar{\theta} - \theta)}{\sin \bar{\theta}} .$$

The curve shown is for $\theta = 30^\circ$, using the parameters for the telescope collimator (see Table I). For the case of unequal front and rear slit widths this curve has a flat top over a limited region close to $\bar{\theta} = \theta$.

For further discussion see pages 9, 11 and 33.



a) SLIT GEOMETRY FOR DETECTOR



b) ANGULAR RESOLUTION OF COLLIMATOR

FIGURE 6

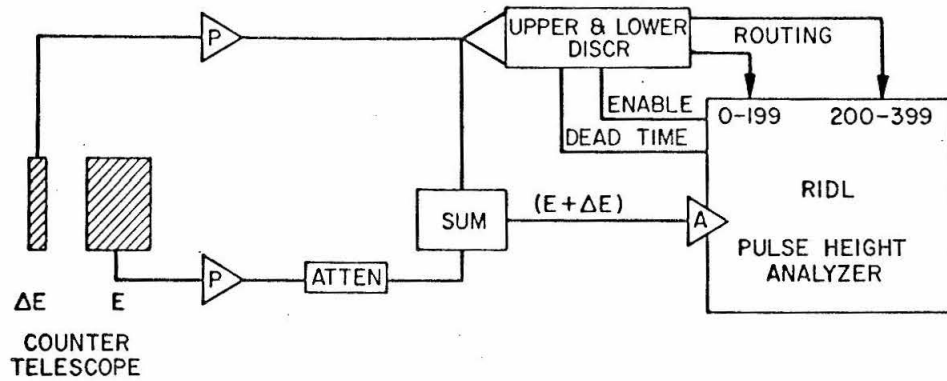
Block Diagram of Electronics

A block diagram of the electronics is shown in a) for the single particle spectra and in b) for the coincidence measurements.

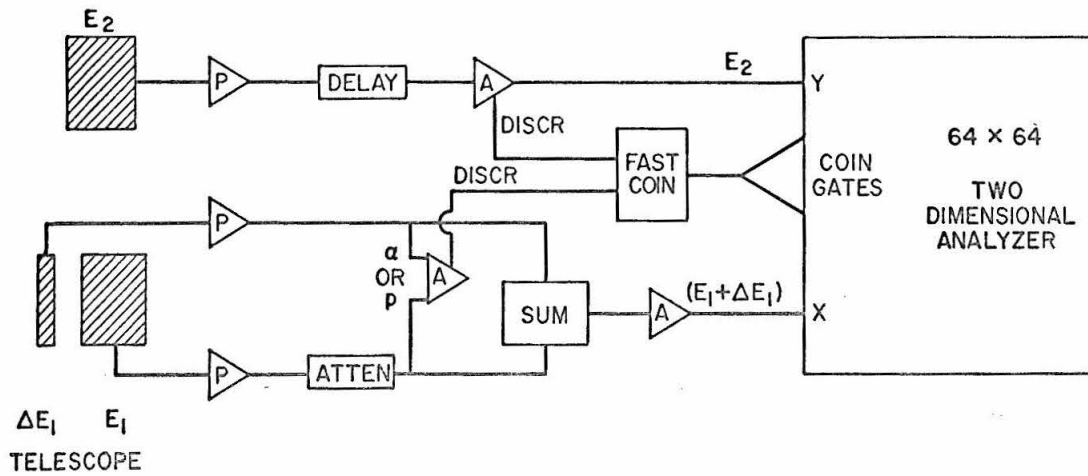
Part a) A counter telescope was used to separate particles with charge 1 from those with charge 2 by routing the pulse-height analyzer on the basis of the size of the energy lost in a thin surface-barrier detector ($\Delta E \propto dE/dx \propto MZ^2/E$). This enabled separation of protons from charge 2 particles down to an energy of ~ 2 MeV.

Part b) A counter telescope was employed at one angle for charge separation and was required to be in coincidence with a second single detector positioned at some other angle in the plane defined by the incoming beam and the counter telescope. Coincidence pulses were then stored in a 64×64 two-dimensional analyzer.

For further details see pages 13, 23 and 58.



a) CONFIGURATION FOR SINGLES SPECTRA



b) FOR COINCIDENCE SPECTRA

FIGURE 7
Sample Analyzer Calibration

The energy calibration of the charge 1 portion of the pulse-height analyzer is shown for the experimental run at $E_{\text{He}^3} = 9.94$ MeV. The energetic particles for this calibration were obtained by observing protons from the reaction $D(\text{He}^3, p)\text{He}^4$ ($Q = +18.353$) at various laboratory angles. The non-linear response of the detectors used is evident at the higher proton energies. This necessitated fitting the energy calibration in two regions; for $E \leq 14$ MeV using a linear expression relating energy to channel number and for $E > 14$ MeV using a quadratic expression. Along the bottom of the plot the approximate position of the proton peak corresponding to the Li^5 ground state is shown for various laboratory angles. For further details see pages 24 and 33.

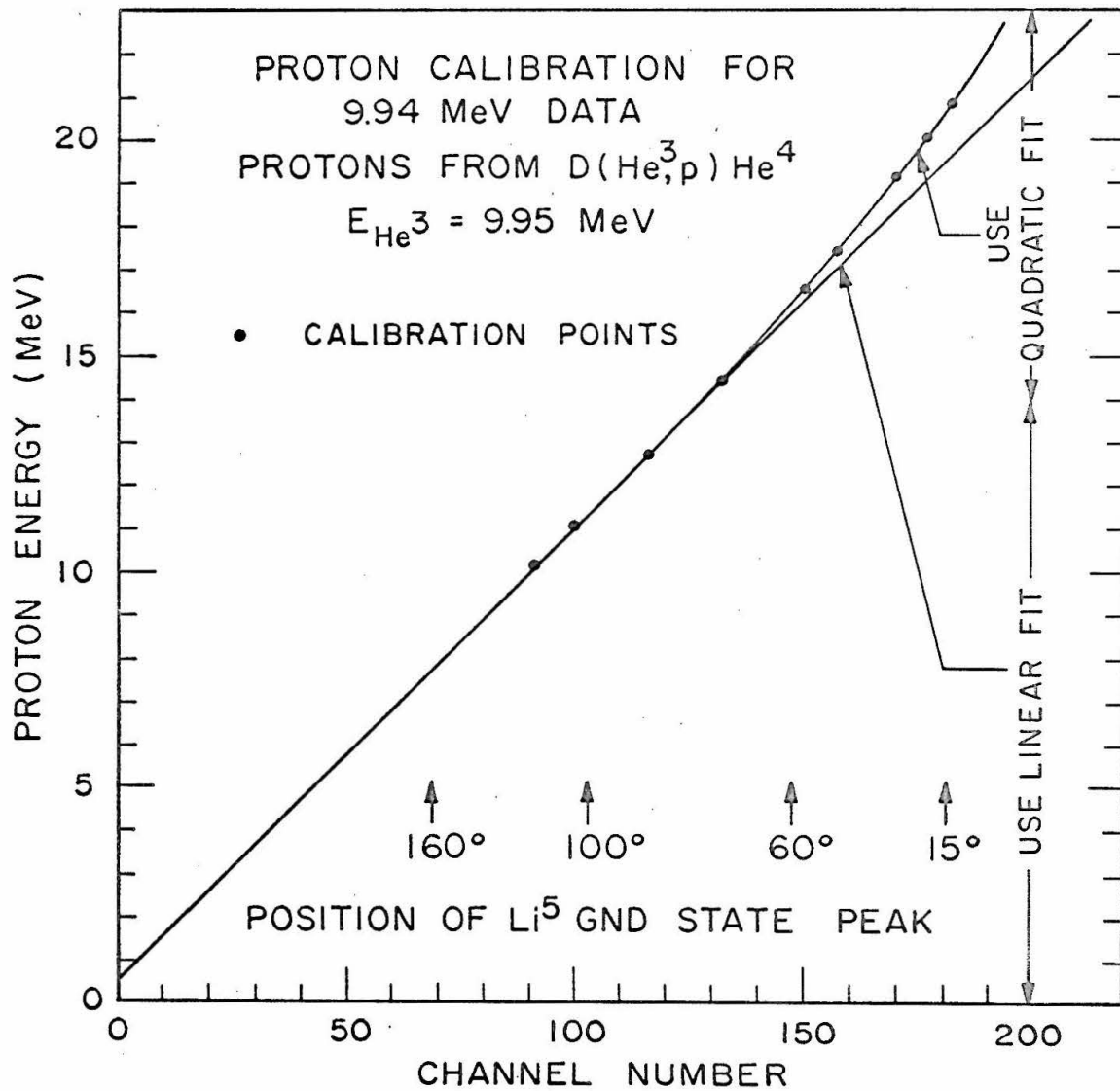


FIGURE 8
Spectrum Sequence at 20°

A sequence of the charge 1 particle spectra is shown at a laboratory angle of 20° for He^3 bombarding energies 2.81, 5.92, 9.94, 13.81, and 18.01 MeV. These energy spectra have been unfolded from smooth curves drawn through the original spectra (see Figure 17 for an example), taking into account the non-linear response of the counter for high energy particles.

The dashed curve at high energies traces the kinematic locus of protons leaving a Li^5 in its ground state. The two dashed lines spanning the lower energy region indicate the spread of proton energies that would result from the breakup of a Li^5 with an excitation corresponding to the center of the ground state. The height of the ground state group represents roughly how the extracted cross section increases as a function of bombarding energy. At this forward angle it is evident that above a bombarding energy of about 10 MeV, other processes contribute substantially to the lower energy region of the charge 1 particle spectrum.

For further discussion see pages 25 and 37.

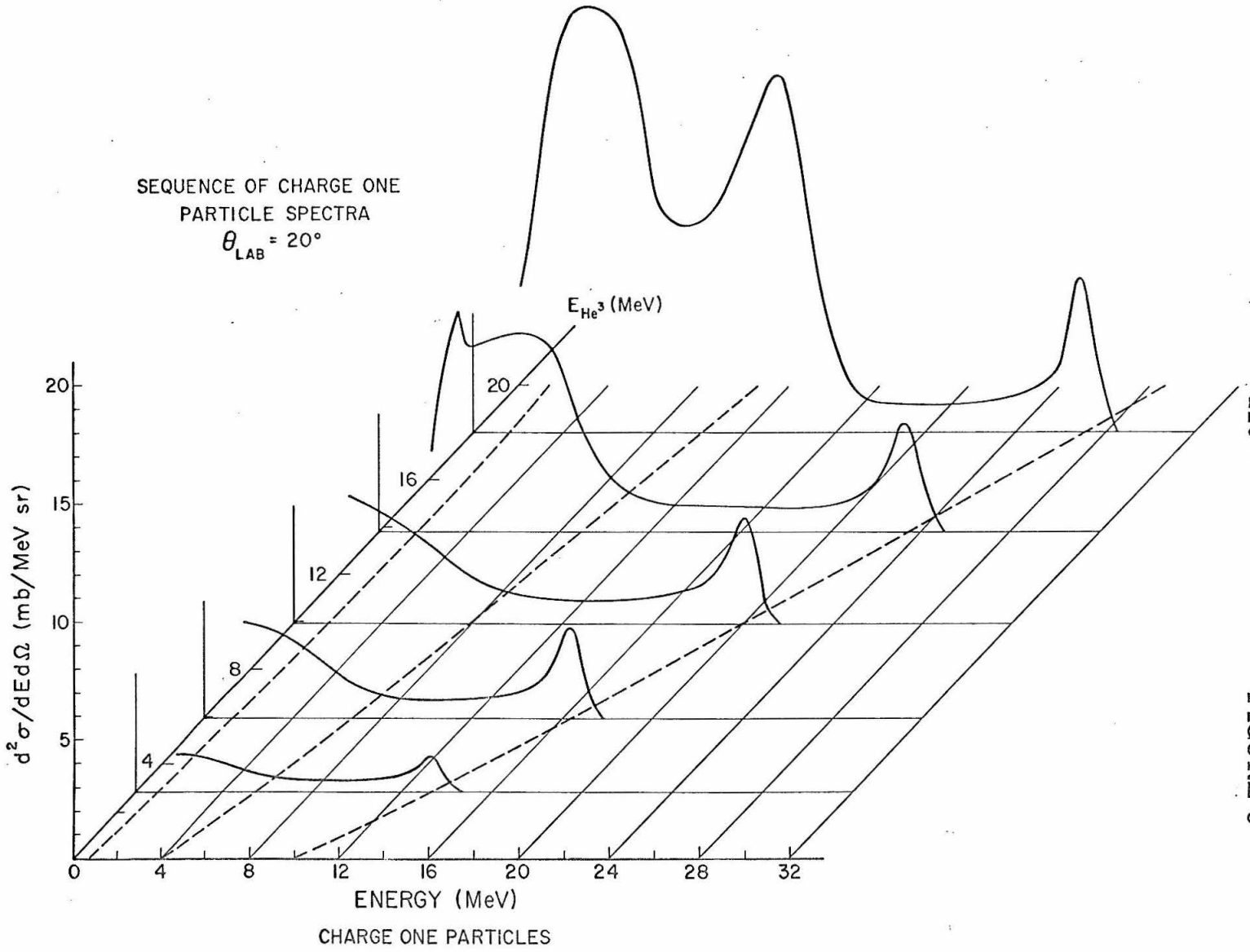


FIGURE 9
Density Functions for $(p + \text{He}^4)$

This figure shows the behavior of the two density functions used to represent the Li^5 ground state. The curves are plotted as a function of excitation in the $(p + \text{He}^4)$ system and have been normalized to the same peak height. The weighting function for the R-matrix formalism parametrizes the probability of forming the $(p + \text{He}^3)$ system at given excitations by a Breit-Wigner single-level description of the Li^5 ground state. The spectral measure function (SMF) formalism describes this weighting function more generally in terms of a dispersion integral over the scattering phase shift for a particular partial wave. In the present case the two forms exhibit a similar behavior over the region of the Li^5 ground state, but as one considers higher excitations in the $(p + \text{He}^4)$ system the SMF curve remains considerably above the R-matrix density function.

For further discussion see pages 30, 31, 34 and 35.

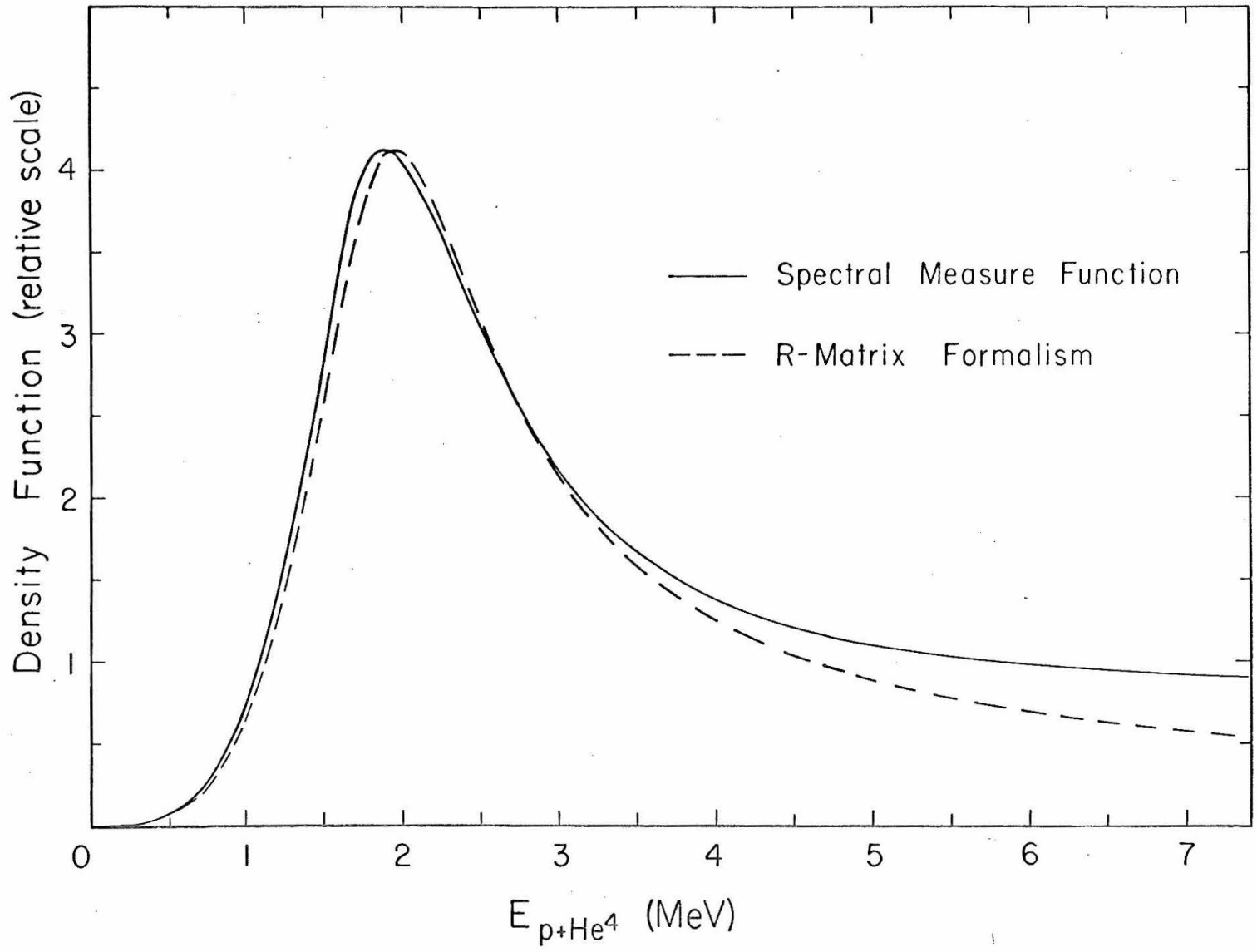


FIGURE 10

Comparison of Proton Spectrum Calculations

The results of several different spectral shape predictions are compared with the observed proton spectrum at a He^3 bombarding energy of 7.95 MeV and a laboratory angle of 20° . The upper portion of the figure shows the fitted spectrum (solid line) obtained using the spectral measure function weighting for the Li^5 ground state interaction ($\delta_1^{3/2}$) and including a Coulomb interaction with $\ell_3 = 1$ between the first proton and the recoiling Li^5 system. The dashed lines indicate that portion of the calculated spectrum due to the high energy proton group leaving Li^5 and that due to the isotropic breakup in flight of the Li^5 . The arrow indicates the lower limit for the particle separation in the counter telescope.

The lower portion of the figure compares the spectral shapes obtained for the following conditions:

- A SMF for Li^5 ground state and Coulomb interaction with $\ell_3 = 1$ for first proton.
- B R-matrix for Li^5 ground state and no interaction for the first proton.
- C R-matrix for Li^5 first excited state and no interaction for the first proton.
- D Phase space prediction.

For further details see pages 33, 34, 75 and 78.

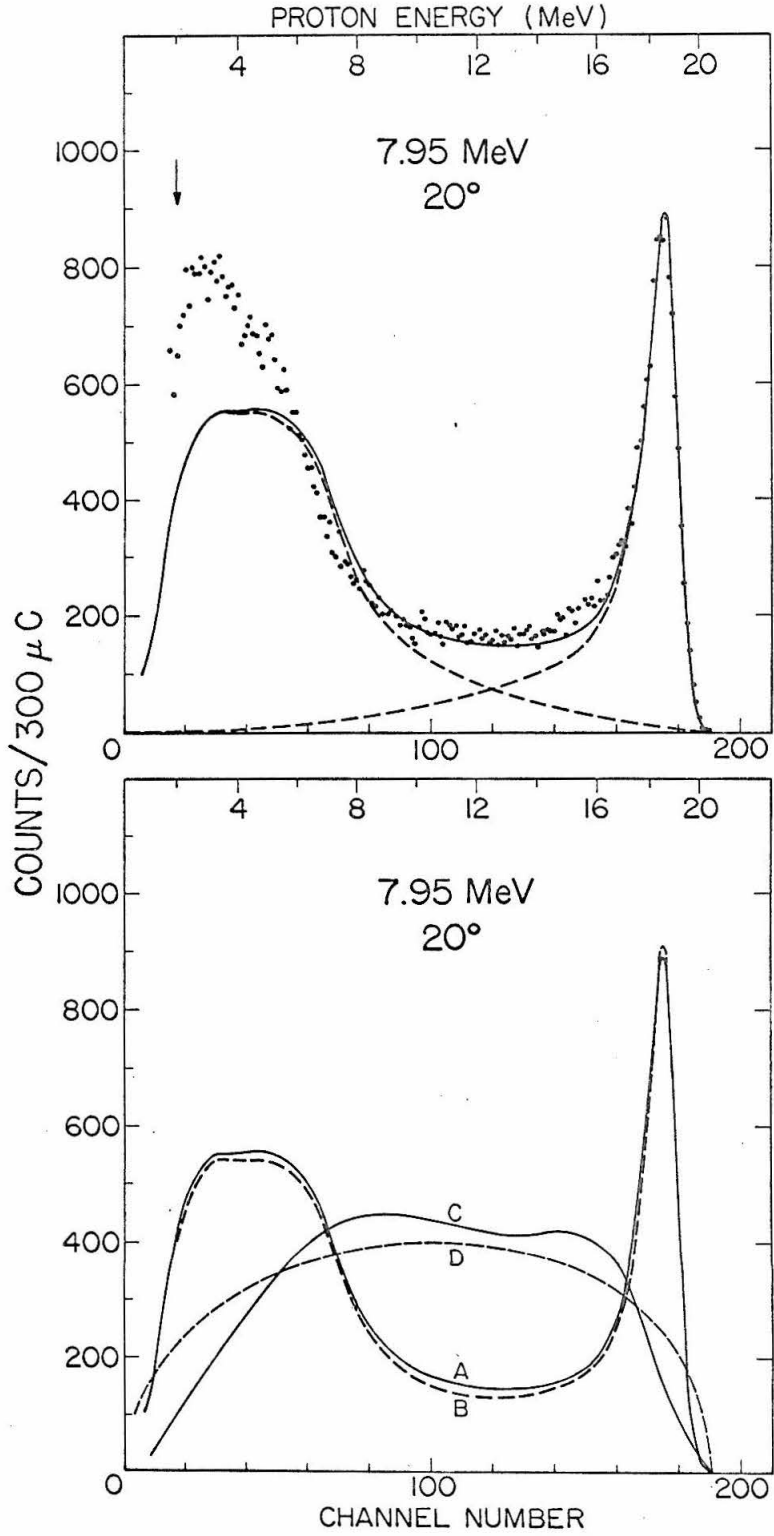


FIGURE 11

Fitting Procedures for Li^5 Ground State

The spectrum obtained at a laboratory angle of 20° and a He^3 bombarding energy of 9.94 MeV is shown to illustrate the method of extracting a cross section for the Li^5 ground state mode. The solid dots represent the observed 200-channel spectrum. An energy scale is provided at the top.

For a given peak position X_P the normalization of the theoretical spectrum was determined by matching the area under the curve above X_A to the number of counts observed in the corresponding region of the experimental spectrum. A "best fit" to the experimental spectrum was then obtained by varying the peak position X_P slightly ($\sim \pm 0.5$ channels) to determine the value of X_P which minimized Δ^2 (as shown in the inset). Here

$$\Delta^2(X_P) = \frac{1}{n} \sum_{i=1}^n \frac{(N_i^{\text{exp}} - N_i^{\text{th}}(X_P))^2}{N_i^{\text{exp}}}$$

and n is the number of experimental points in the peak above X_A .

The total yield for this particular angle is then the area under the theoretical shape for the first proton. This is represented by the dashed curve away from the peak. The additional contribution to the solid curve comes from the breakup in flight of the Li^5 ground state. This recoil spectrum was calculated using an angular distribution $(1 - 0.24 \cos^2 \tilde{\theta})$ for the first proton (see Table III) and an oriented breakup $(1 - 0.875 \cos \theta_R)$ for the second proton with respect to the recoil direction. While the first proton curve corresponds to a rather narrow angular range in the center-of-mass system, the latter includes contributions from many center-of-mass angles.

See Appendix A and pages 35, 39 and 42.

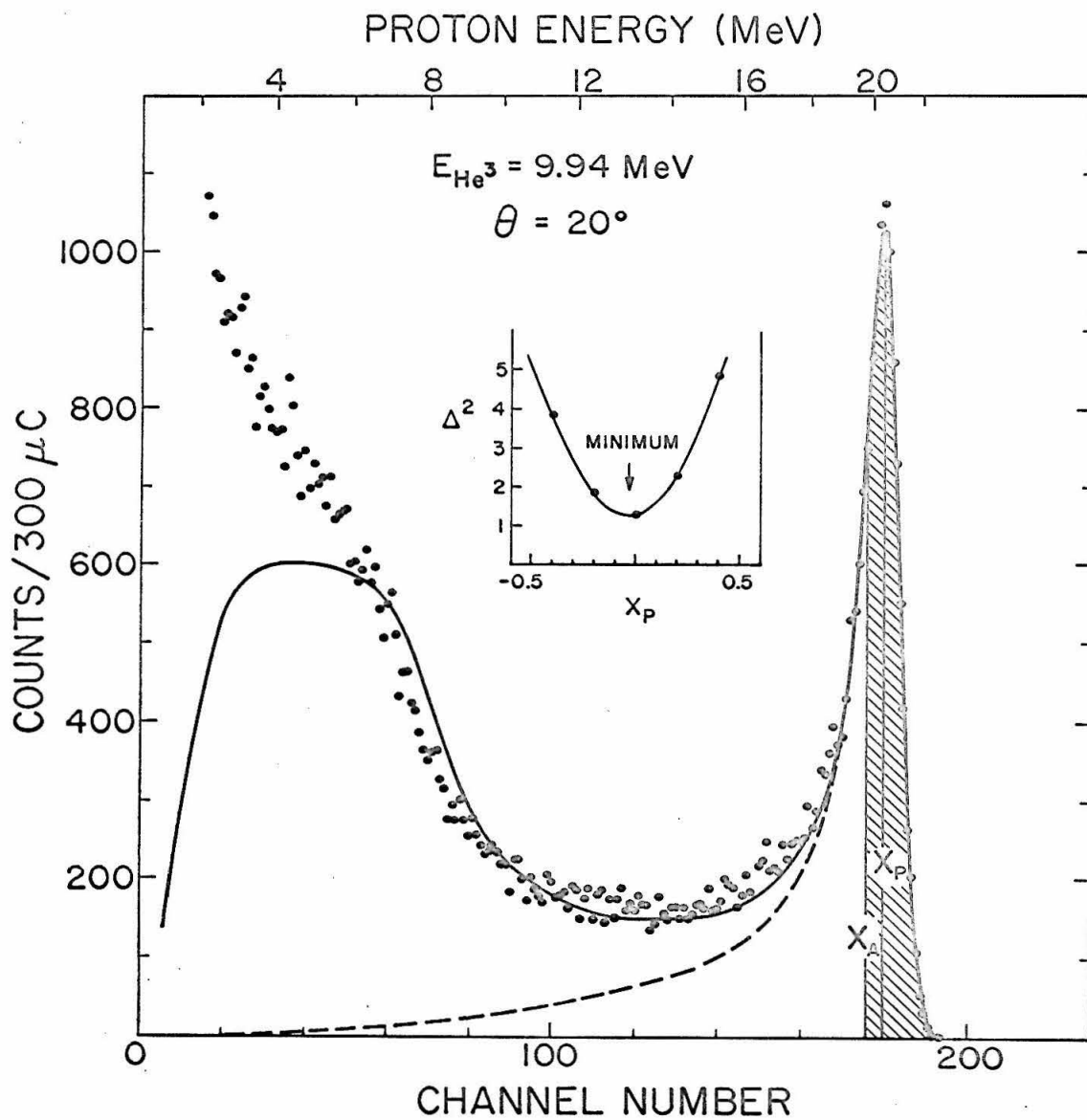


FIGURE 12
8 MeV Spectra, 20° and 40°

The observed proton spectra (solid dots) and the fitted spectral shapes are shown for 7.95 MeV at laboratory angles of 20° and 40° . An energy scale is provided at the top of each spectrum. The arrow at a proton energy of 2 MeV represents the minimum separation energy of the counter telescope.

The fitted curves represent a sum of the high energy proton peak leaving Li^5 in its ground state and the predominately lower energy protons from the subsequent breakup of the recoiling Li^5 (see Appendix A). For the solid curve the recoil calculation includes the angular distribution of the high energy protons ($1-0.24 \cos^2 \tilde{\theta}$; see Figure 23), but allows the recoiling Li^5 to breakup isotropically in its own center-of-mass system. The dashed curve indicates the effect of an oriented recoil breakup ($1-0.875 \cos \theta_R$) for the protons with respect to the direction of the recoiling Li^5 (as suggested by the alpha-particle measurements in Part IV, B). The two curves merge and exhibit the same form over the region of the high energy peak.

For additional details see Figures 23 and 37, Table III, and pages 25, 36 and 37.

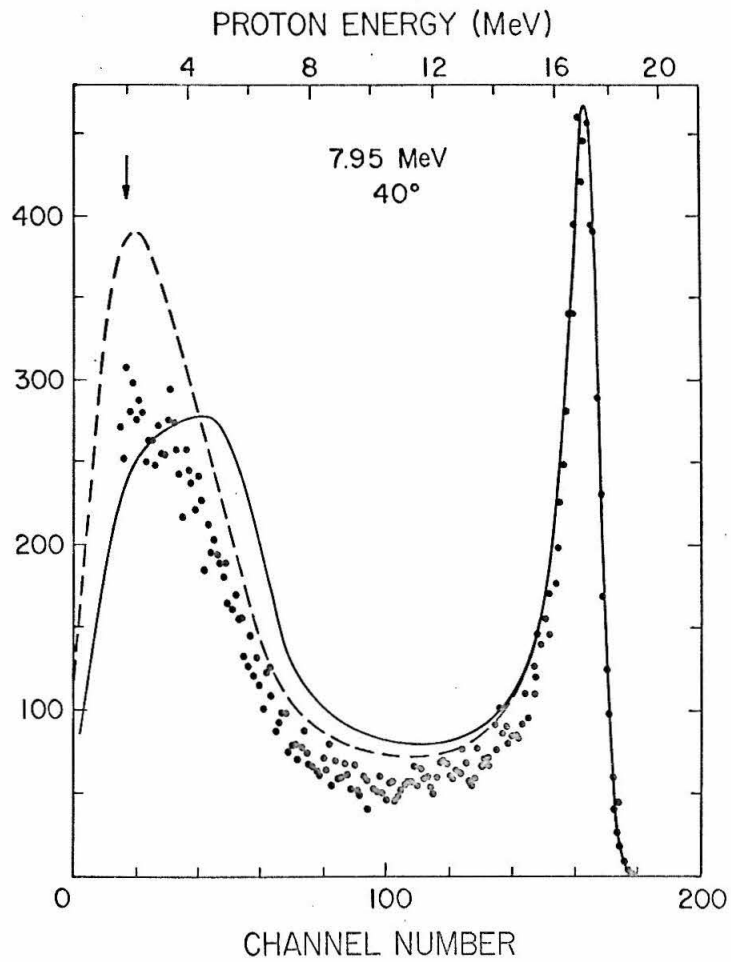
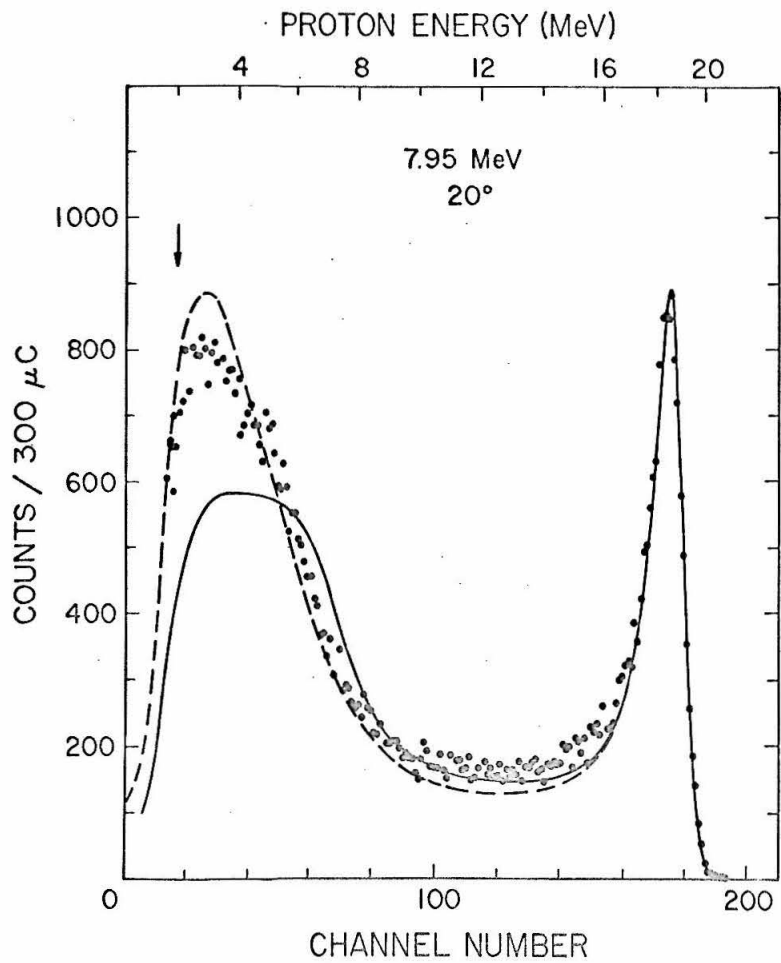


FIGURE 13
8 MeV Spectra, 60° and 80°

Proton spectra and the fitted spectral shapes are shown for 7.95 MeV at 60° and 80° . As in Figure 12 the solid curve is for an isotropic breakup of the recoiling Li^5 . The dashed curve is for a breakup $(1 - 0.875 \cos \theta_R)$ where θ_R is measured from the recoil axis. See the caption for Figure 12 and pages 25, 36 and 37.

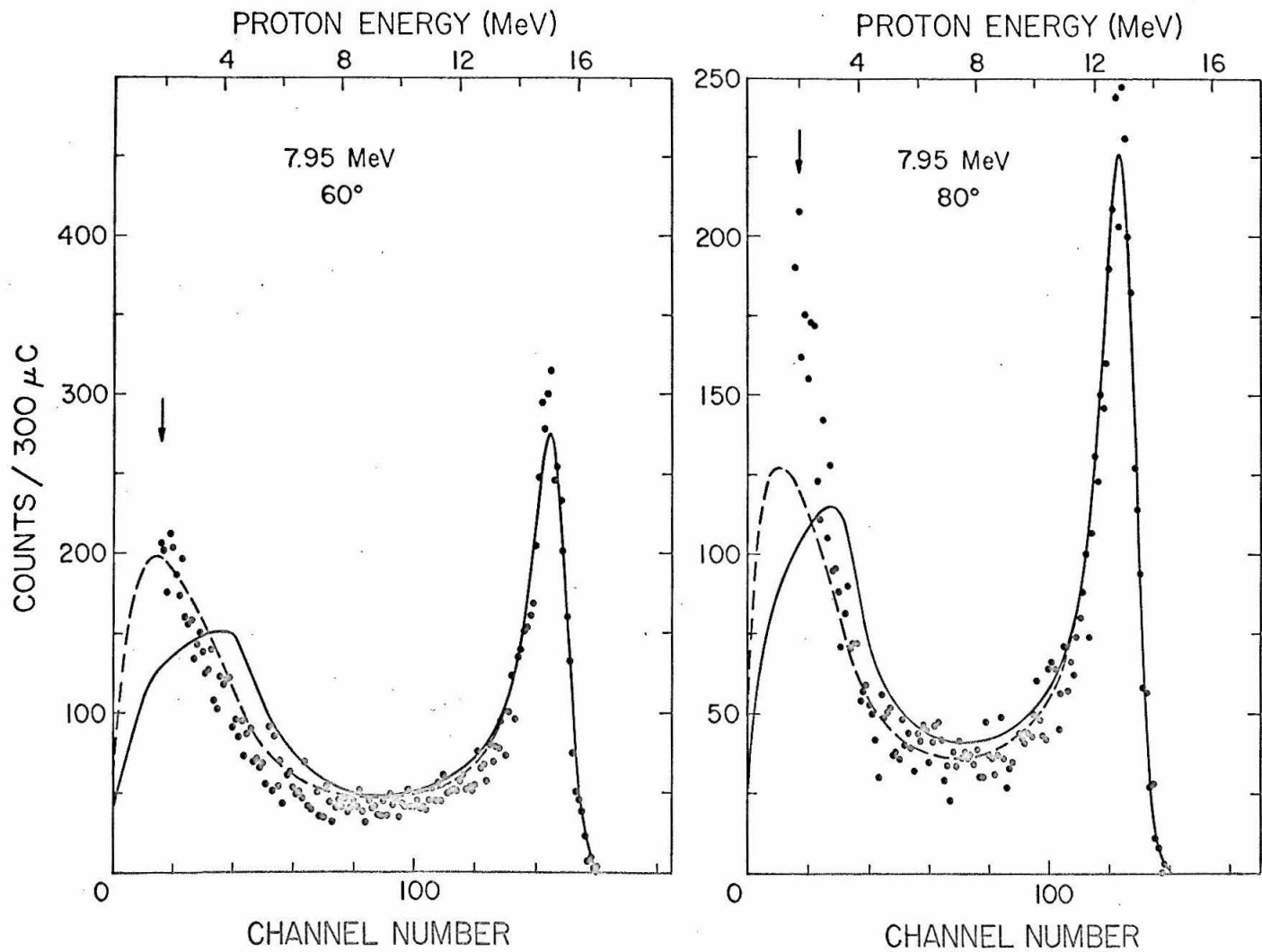


FIGURE 14
8 MeV Spectra, 100° and 120°

Proton spectra and the fitted spectral shapes are shown for 7.95 MeV at 100° and 120° . As in Figure 12 the solid curve is for an isotropic breakup of the recoiling Li^5 . The dashed curve is for a breakup $(1 - 0.875 \cos \theta_R)$. See the caption for Figure 12 and pages 25, 36 and 37.

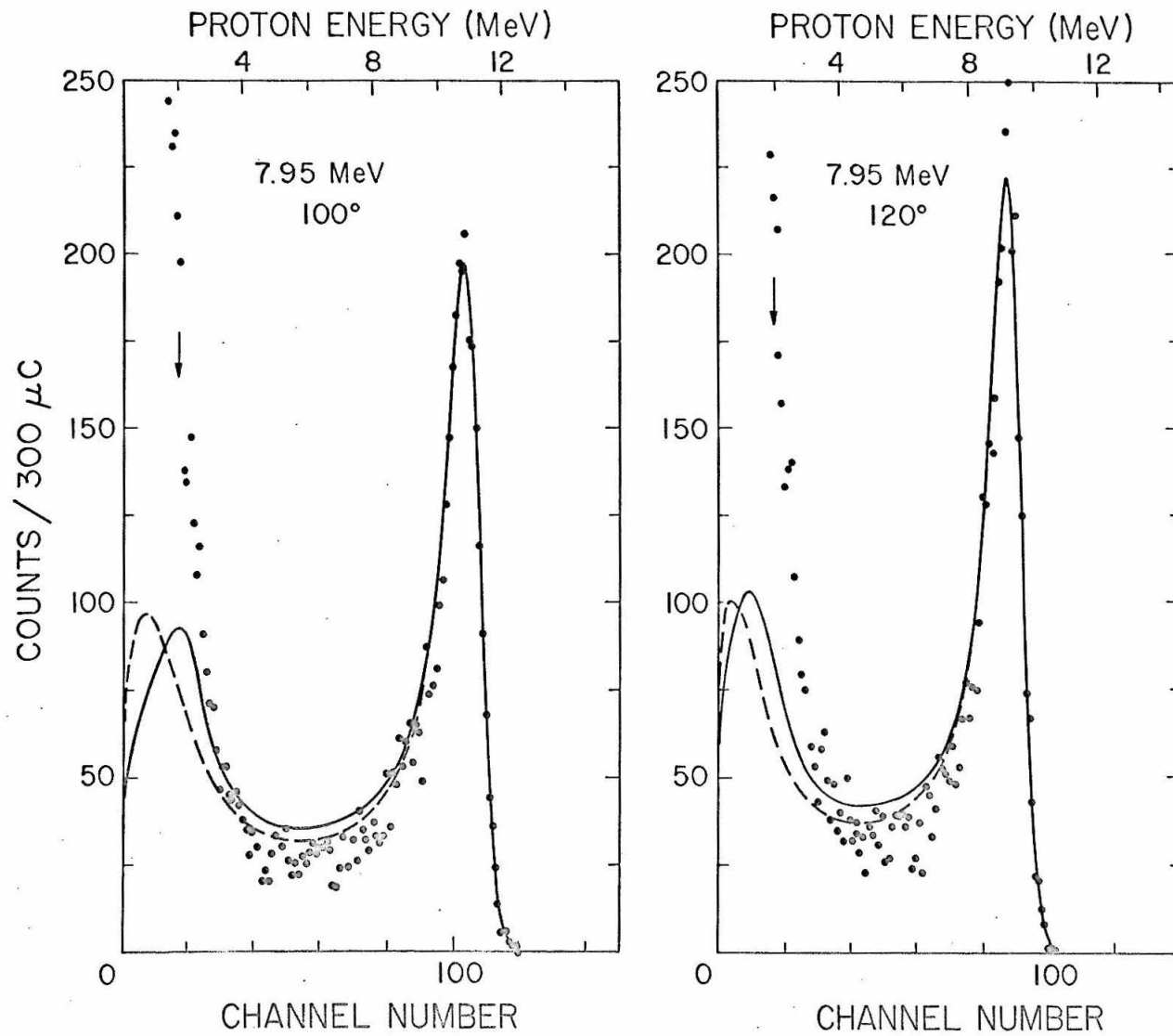
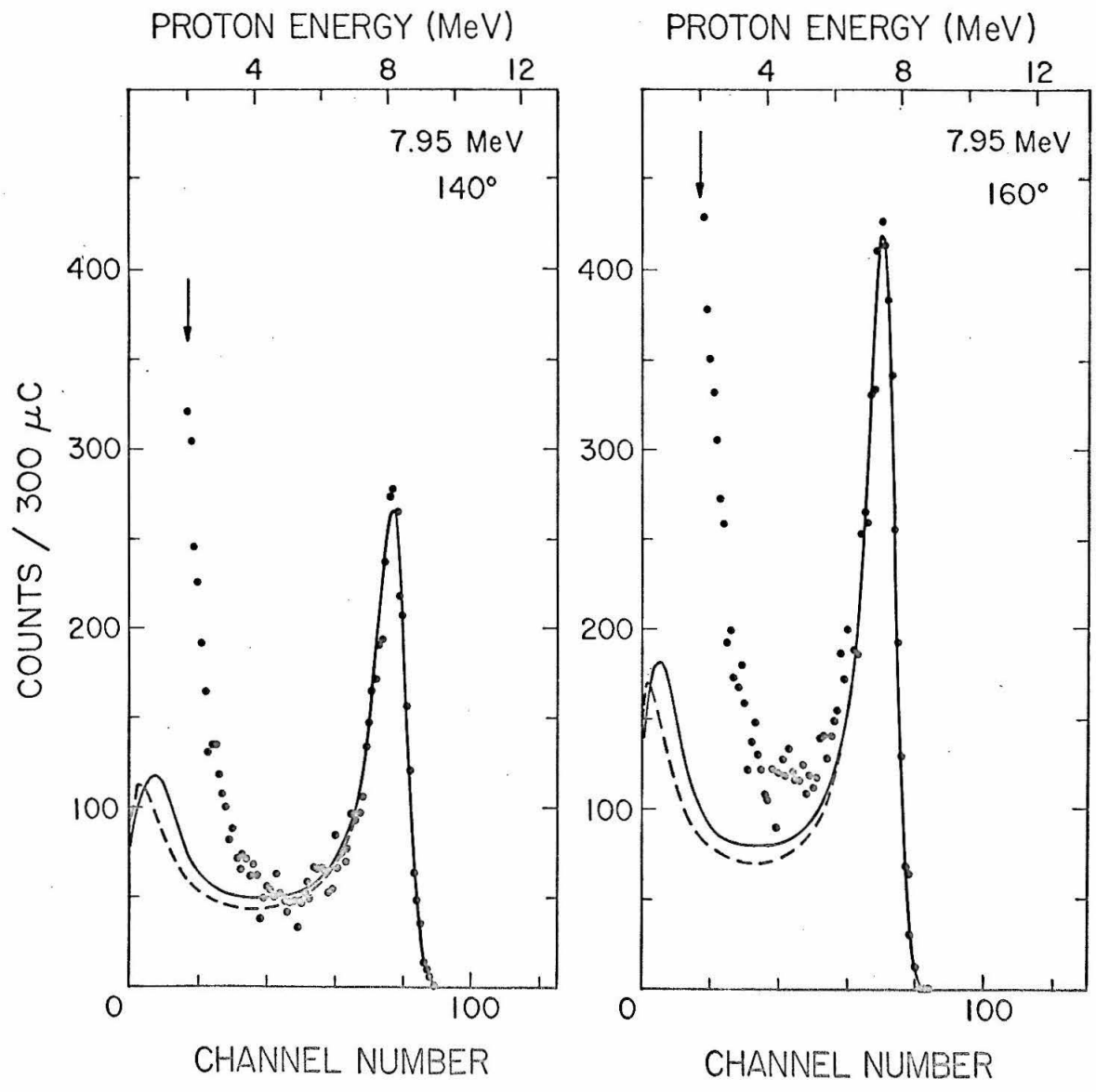


FIGURE 15
8 MeV Spectra, 140° and 160°

Proton spectra and the fitted spectral shapes are shown for 7.95 MeV at 140° and 160° . As in Figure 12 the solid curve is for an isotropic breakup of the recoiling Li^5 . The dashed curve is for a breakup $(1 - 0.875 \cos \theta_R)$. See the caption for Figure 12 and pages 25, 36 and 37.



124
FIGURE 15

FIGURE 16
3 MeV Spectra, 40° and 90°

Proton spectra and the fitted spectral shapes are shown for 2.81 MeV (the lowest separated angular distribution) at 40° and 90° . As in Figure 12 the solid curve is for an isotropic breakup of the recoiling Li^5 . The dashed curve is for a breakup $(1 - 0.875 \cos\theta_R)$. See caption for Figure 12 and pages 25, 37 and 61.

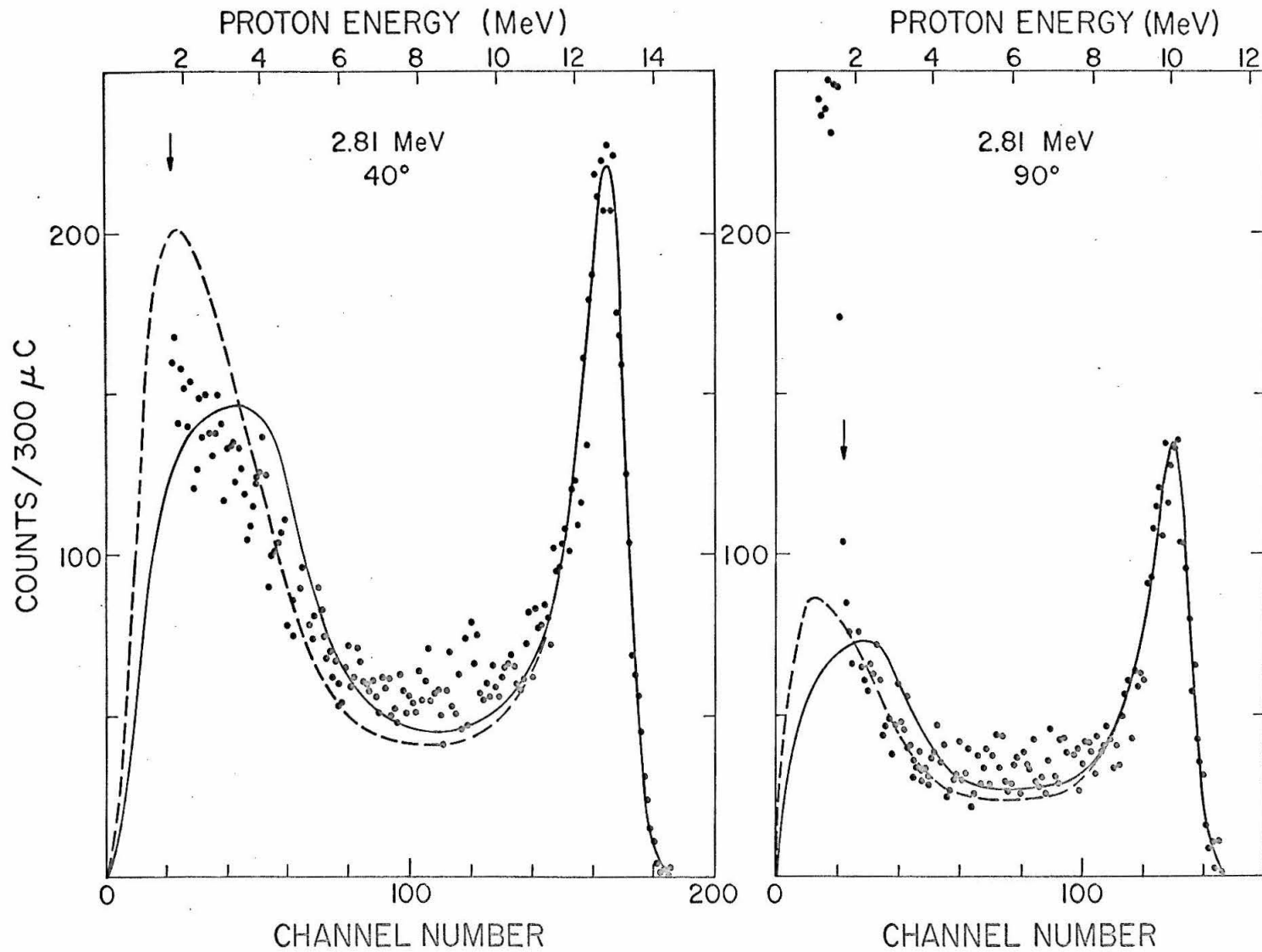


FIGURE 17
18 MeV Spectrum, 20°

The spectrum of charge 1 particles is shown for 18.01 MeV with the counter telescope at 20° . As in Figure 12 the fitted spectral shapes are given. The solid curve is for an isotropic breakup of the recoiling Li^5 and the dashed curve is for a breakup $(1 - 0.5 \cos \theta_R)$.

Note the extreme non-linearity of the energy scale that accentuates the height of the high energy proton group. The arrows bracketing the additional structure at low energy indicate that these peaks might be due to a) protons and deuterons from the mechanism in which deuterons leave an interacting $(p + \text{He}^3)$ system and b) protons from the reaction mode $\text{He}^4 + 2p$ (singlet p - p interaction). The narrow peak at 12 MeV on the back side of the higher group is due to recoil protons from a slight hydrogen contaminant in the target (probably in the form of water vapor).

For further discussion see pages 25, 38, 43, 52 and 54.

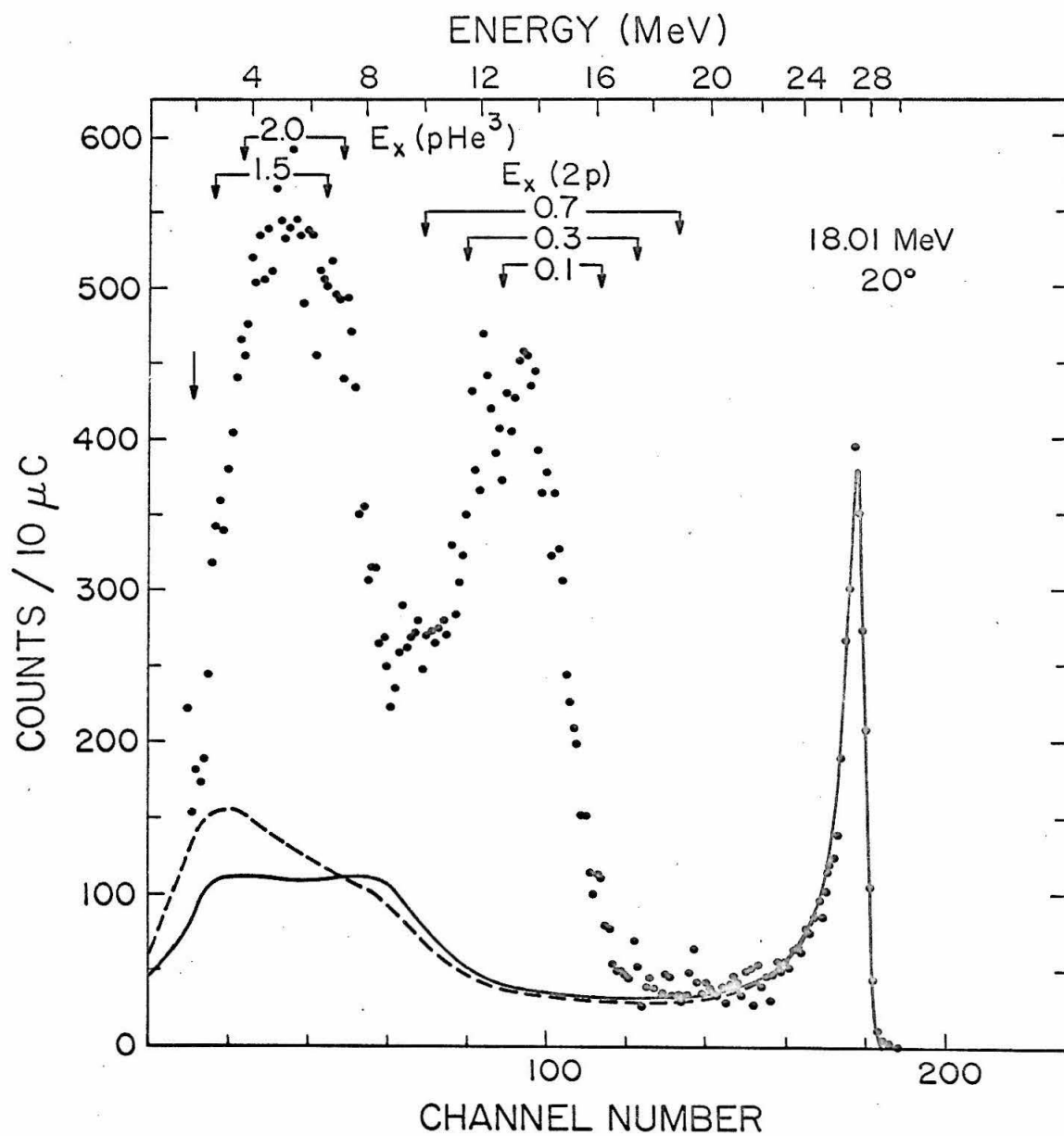


FIGURE 18

Angular Distributions in the Laboratory System

A comparison is presented of the angular distributions in the laboratory system for the Li^5 ground state transition at the four lowest bombarding energies. Unless indicated specifically the size of the points represents the approximate relative error for that angular distribution. Uncertainties in the absolute normalization ($\sim 5\%$) and in the spectrum calculation ($\sim 10\%$) have not been included here. The smooth curves serve only to connect points in the same angular distribution. The peaking at forward angles for the higher bombarding energies is predominantly due to the increased center-of-mass motion.

For further discussion see page 39.

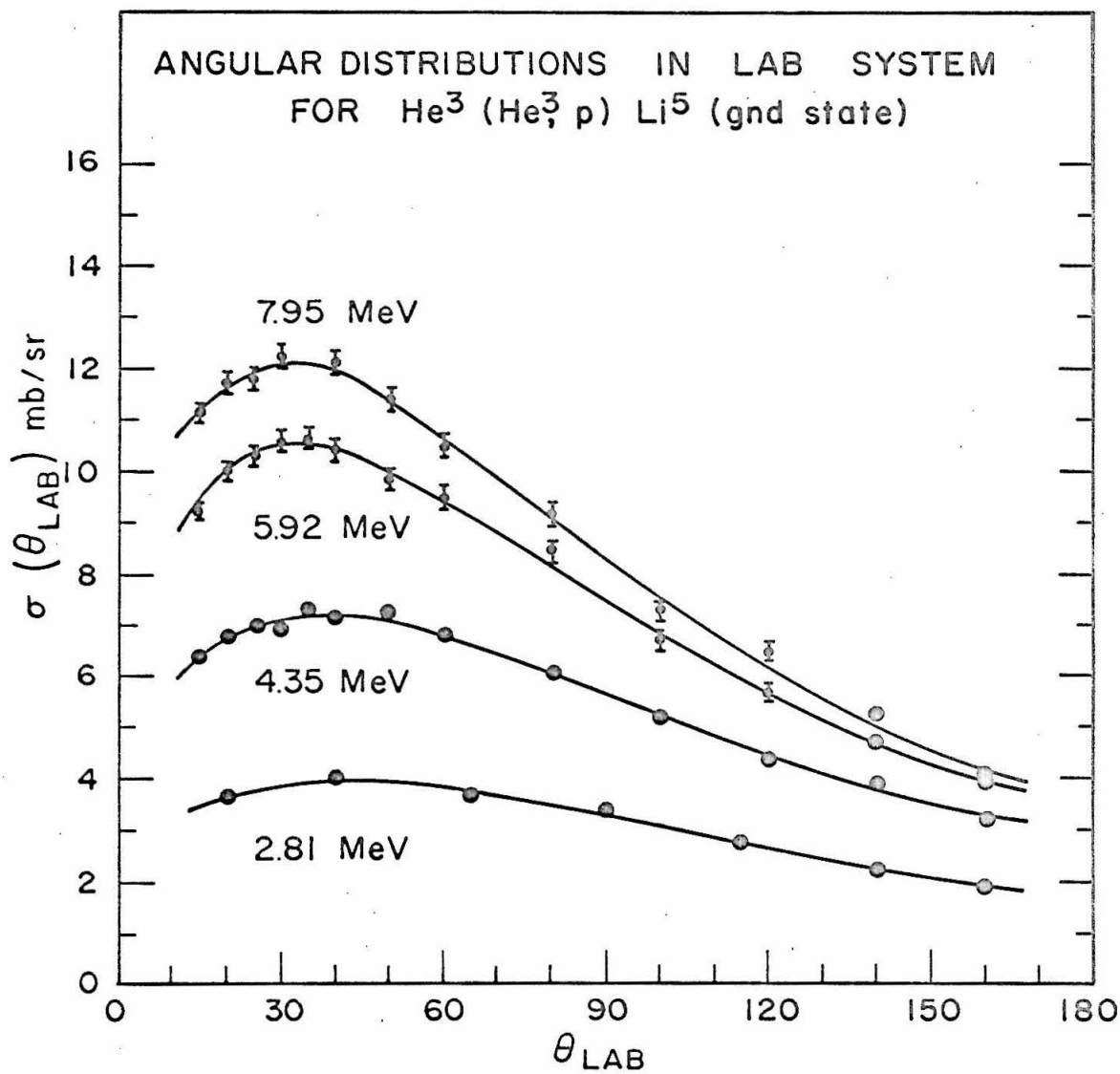


FIGURE 19
Angular Distributions for Li^5 Ground State

Angular distributions resulting from the spectral fits to the high energy proton peak are given in the laboratory system and in the center-of-mass system for He^3 bombarding energies of 2.81 MeV and 4.35 MeV. Typical relative errors are indicated. The center-of-mass cross sections were obtained from measurements at the corresponding laboratory angles by assuming a two-body transformation. The smooth curve represents a least-squares fitting of the function $a_0 + a_2 P_2(\cos \tilde{\theta})$ to the center-of-mass results for $\tilde{\theta} \geq 90^\circ$.

For further discussion see pages 40 and 41.

ANGULAR DISTRIBUTIONS FOR $\text{He}^3(\text{He}^3, p)\text{Li}^5(\text{gnd state})$

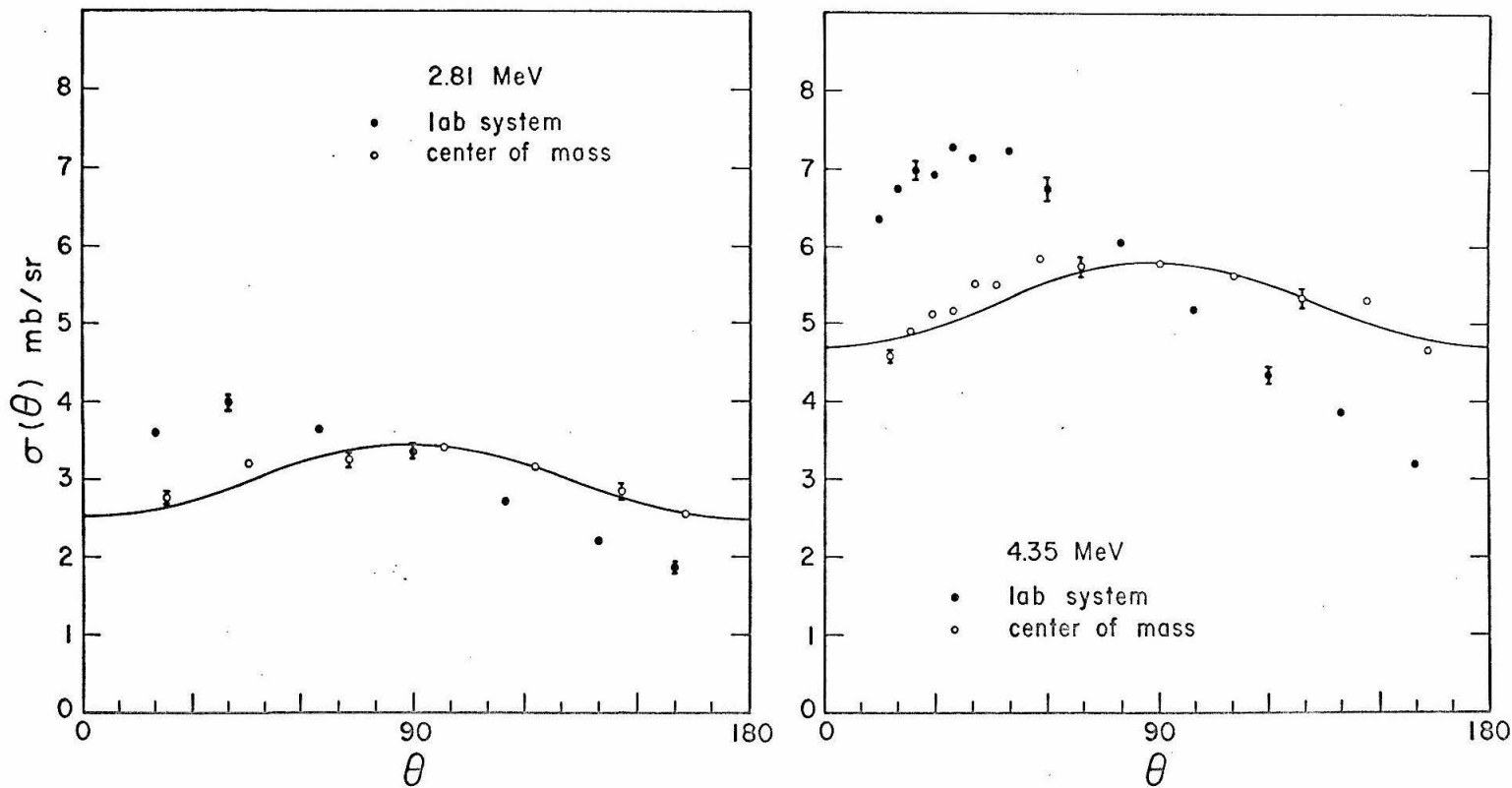


FIGURE 20
Angular Distributions for Li^5 Ground State

The angular distributions for the Li^5 ground state mechanism are shown for 5.92 MeV and 7.95 MeV. As in Figure 19 the smooth curves represent a least-squares fitting of the function $a_0 + a_2 P_2(\cos \tilde{\theta})$ to the center-of-mass results for $\tilde{\theta} \geq 90^\circ$. For further discussion see pages 40, and 41.

ANGULAR DISTRIBUTIONS FOR $\text{He}^3 (\text{He}^3, p) \text{Li}^5(\text{gnd state})$

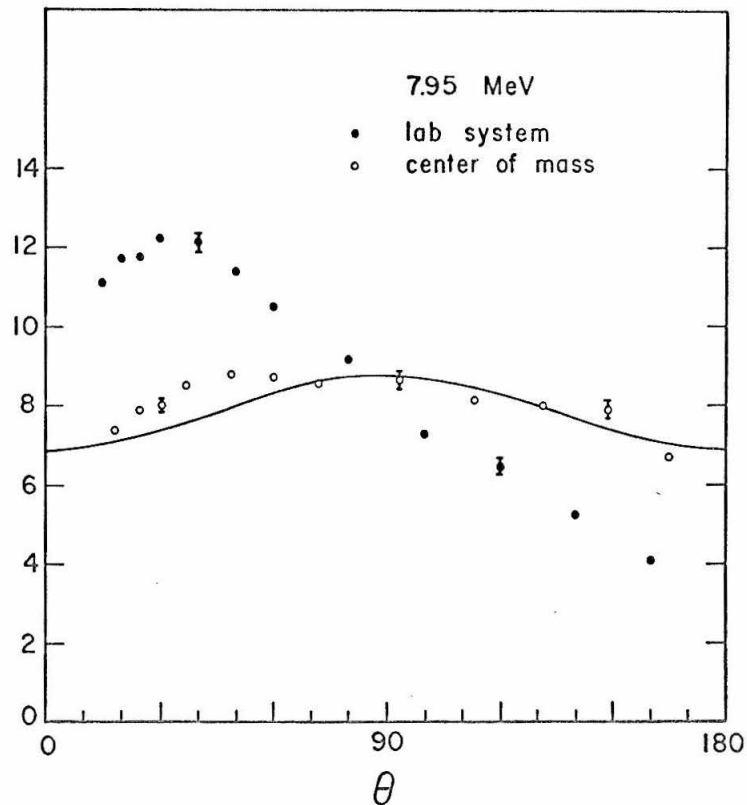
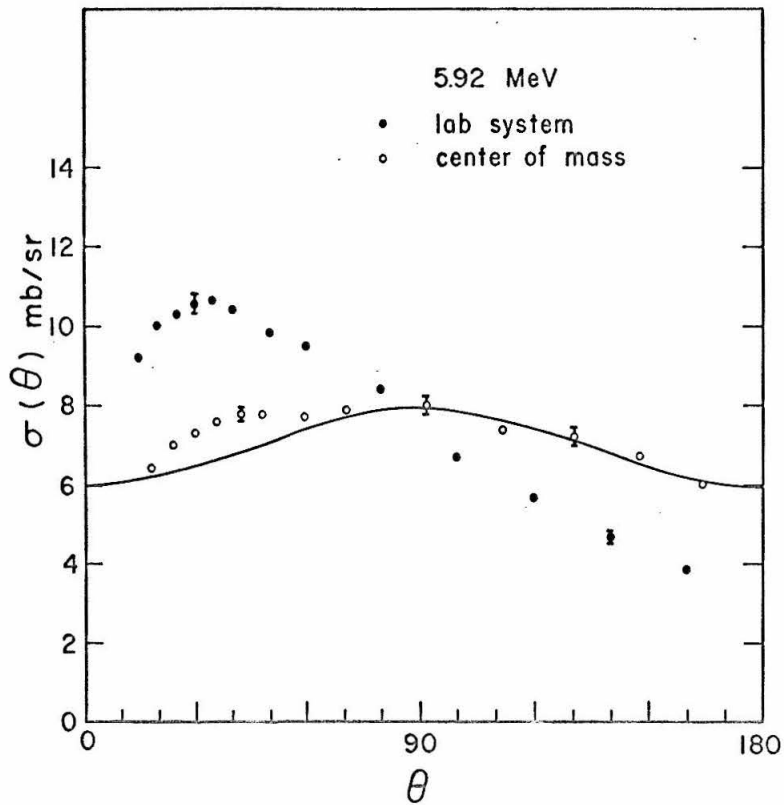


FIGURE 21
Angular Distributions for Li^5 Ground State

The angular distributions for the Li^5 ground state mechanism are shown for 9.94 MeV and 11.93 MeV. As in Figure 19 the smooth curves represent a least-squares fitting of the function $a_0 + a_2 P_2(\cos \tilde{\theta})$ to the center-of-mass results for $\tilde{\theta} \geq 90^\circ$. At these higher bombarding energies this simple form is clearly inadequate. For further discussion see pages 40 and 41.

ANGULAR DISTRIBUTIONS FOR $\text{He}^3 (\text{He}^3, p) \text{Li}^5(\text{gnd state})$

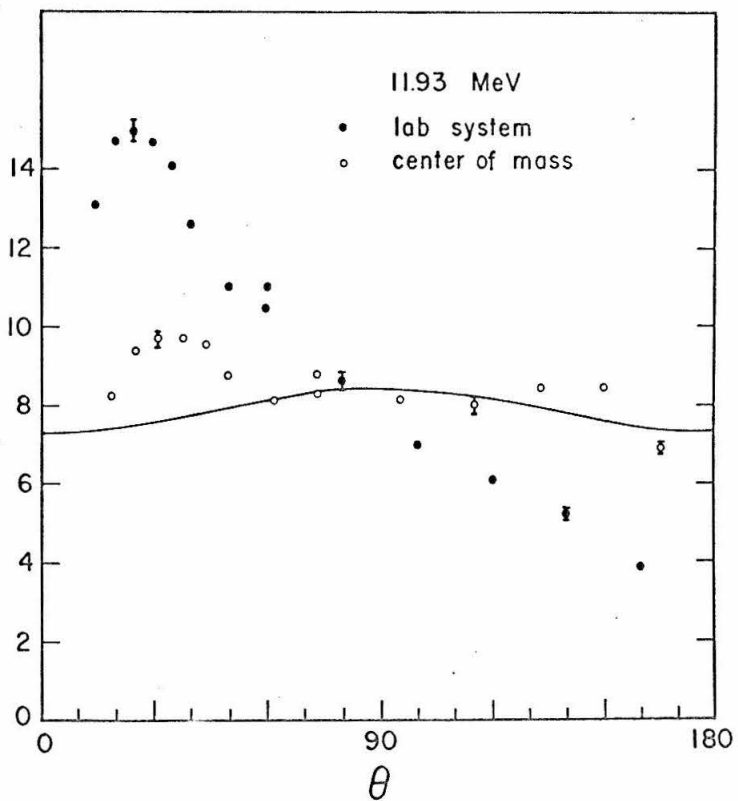
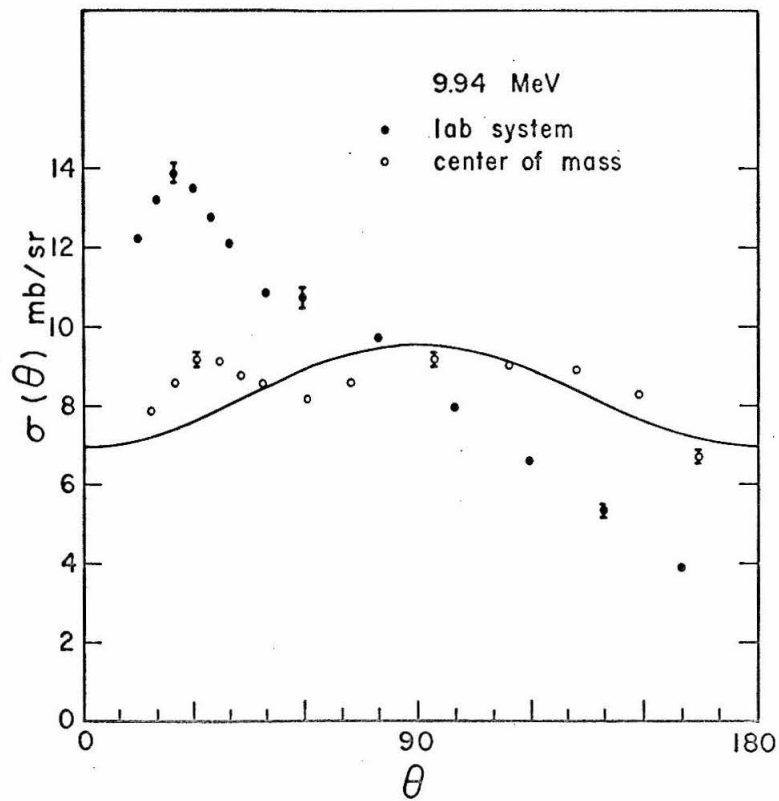
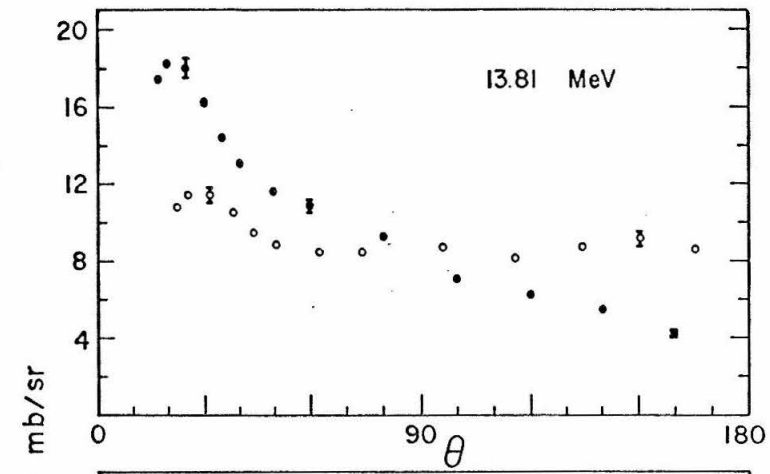


FIGURE 22

Angular Distributions for Li^5 Ground State

The angular distributions for the Li^5 ground state mechanism are shown for the high pressure gas cell measurements at 13.81, 15.55 and 18.01 MeV. Their shape at the backward angles appears to change as one approaches the region of excitation in Be^6 where a broad anomaly has been observed in the $\text{He}^3 + \text{He}^3$ elastic scattering (Bacher and Tombrello, 1965). For further discussion see pages 40 and 41.



ANGULAR DISTRIBUTIONS FOR
 $\text{He}^3 (\text{He}^3, p) \text{Li}^5 (\text{gnd state})$

• lab system
 ○ center of mass

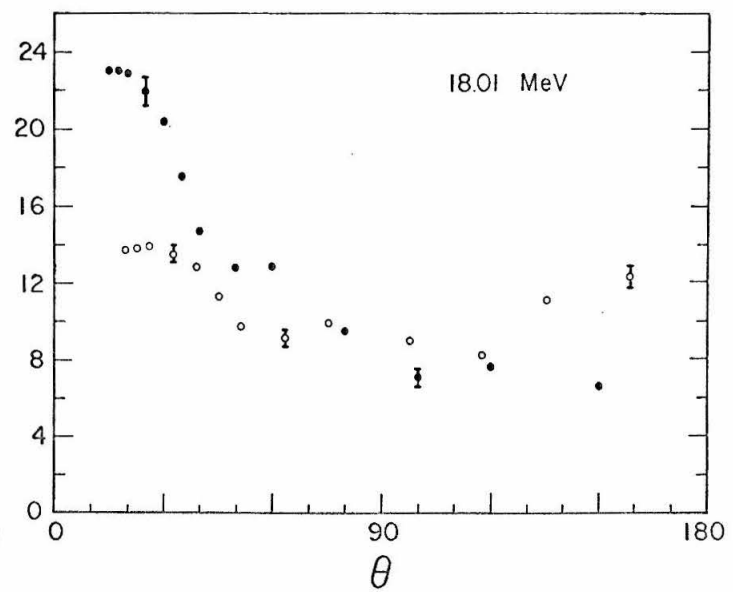
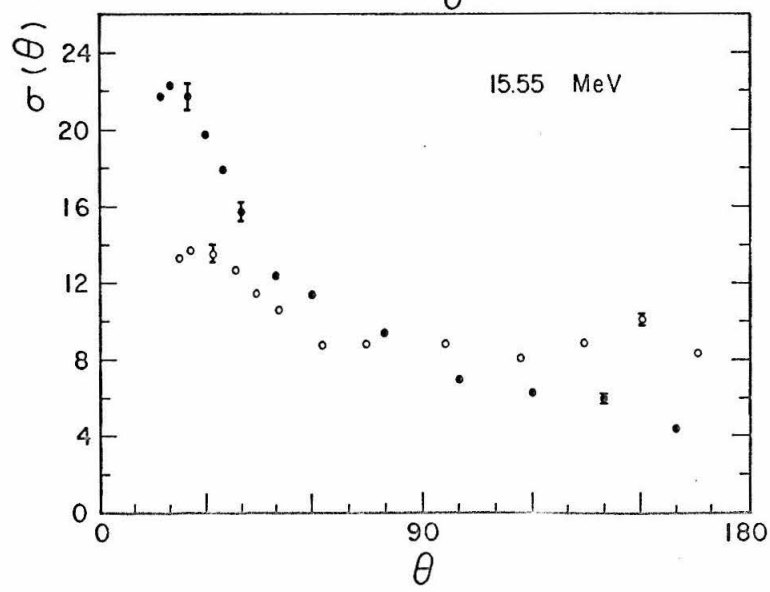


FIGURE 23

Ratio of Legendre Polynomial Coefficients

The ratio of the Legendre polynomial coefficients a_2/a_0 is shown as a function of He^3 bombarding energy. These are the results of a least squares fitting of the functions $a_0 + a_2 P_2(\cos \tilde{\theta})$ to the center-of-mass angular distributions for $\tilde{\theta} \geq 90^\circ$. The errors indicated are due to the relative errors assigned to the measurements for each angular distribution. Below 10 MeV there is reasonable scatter about the value $\overline{(a_2/a_0)} = -0.175$. Above 12 MeV the effects of the opening of another reaction channel and the presence of broad structure in the compound nucleus Be^6 are evident. The values of a_2/a_0 are tabulated in Table III. For further discussion see pages 40 and 41.

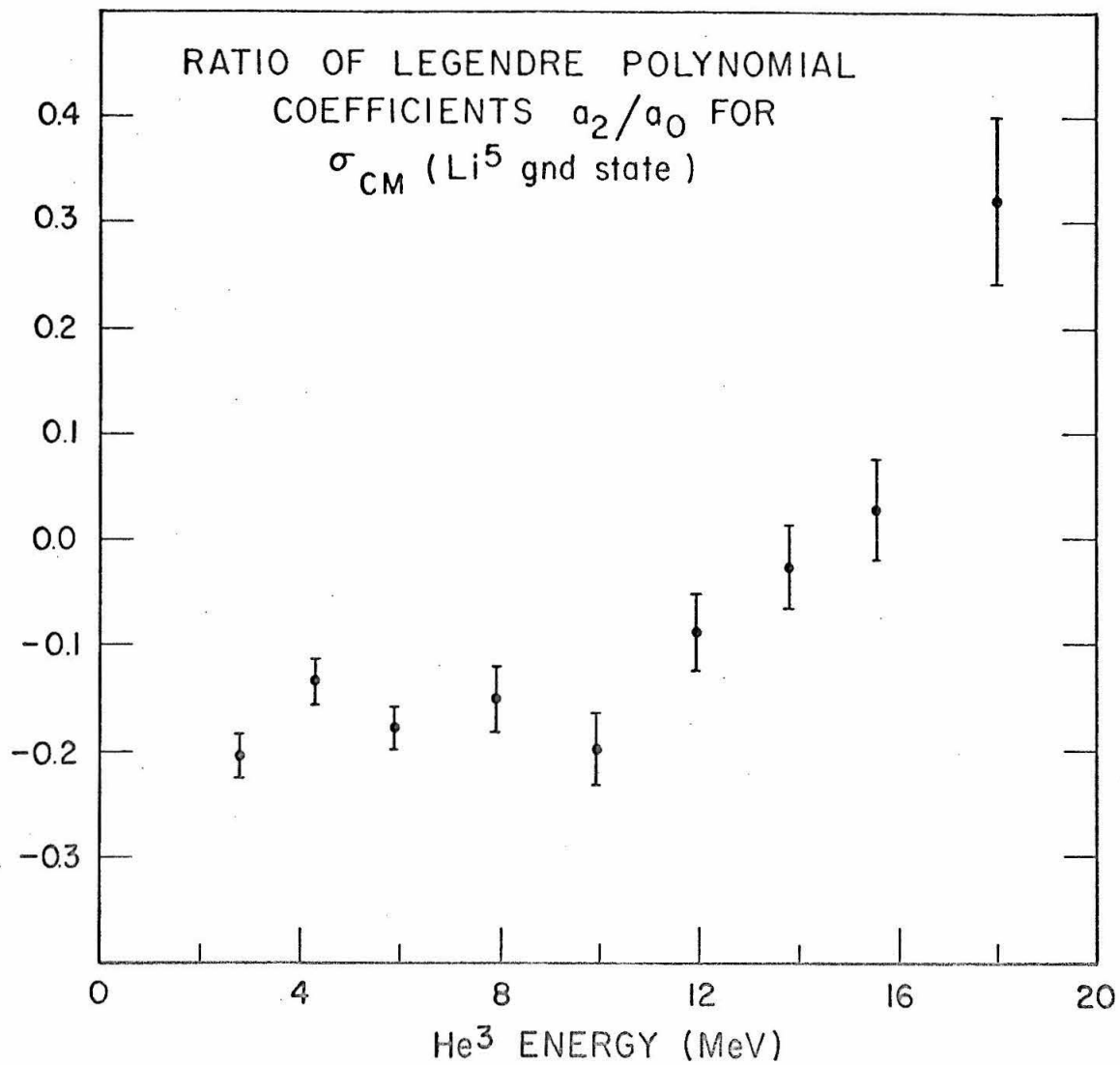


FIGURE 24
Total Cross Section for Li^5 Ground State

This figure presents the total cross sections for that part of the reaction which proceeds sequentially through the Li^5 ground state. These were obtained by determining the area under curves fitted to all angles of the measured angular distributions. The dots represent the results of fitting spectrum shapes to separated proton spectra. The triangles represent the results of similar fits to spectra without charge separation. The errors indicated include only the relative errors for the points in each angular distribution. The values of these total cross sections are given in Table IV. For further details see pages 41 and 42.

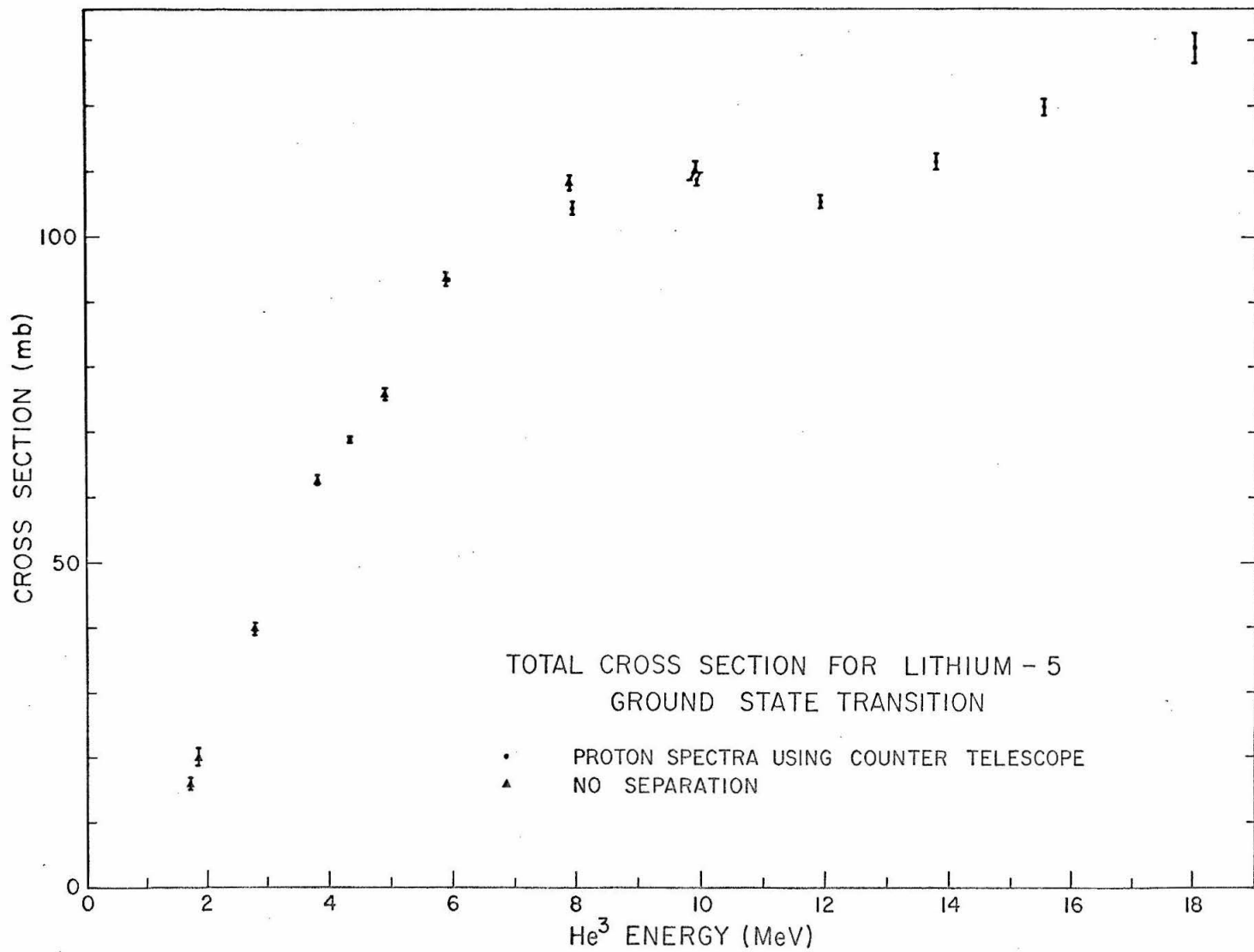


FIGURE 25
Low Energy Extrapolations

This figure illustrates the technique used to extract the total yield of charge 1 particles at each laboratory angle. The data at 2.81 MeV and 4.35 MeV appear to have less background down to the routing threshold of the counter telescope (indicated by arrows in each spectrum) and were therefore used as guides to determine the ratio h_B/h_P at each laboratory angle for the extrapolation of the observed spectrum to zero energy.

In (a) the spectrum for 4.35 MeV and 100° indicates how the shape of the spectrum was assumed to be flat below the lowest separated point. This extrapolation determined the total number of observed counts. The error assigned to this yield was one half of the extrapolated counts (as indicated by the shaded area). In (b) the extrapolation and the assigned error are indicated for one of the higher energy spectra, 9.93 MeV and 100° . The rapid increase of the separated spectrum well above the routing threshold illustrates the possibility of a low energy background and indicates how the present technique reduces its contribution to the total charge 1 yield.

For further discussion see pages 42 and 43.

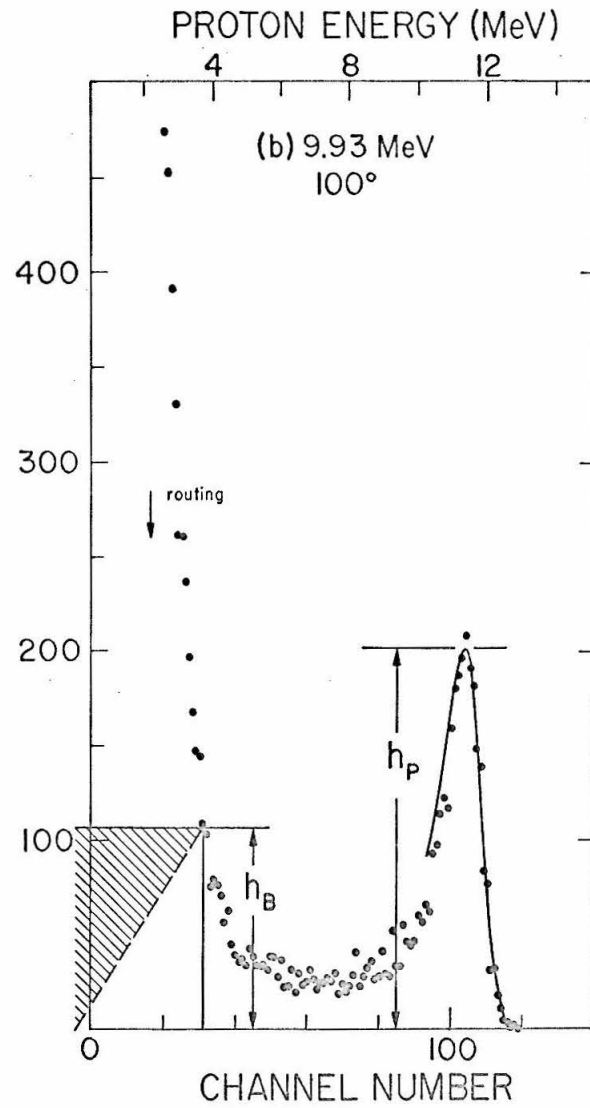
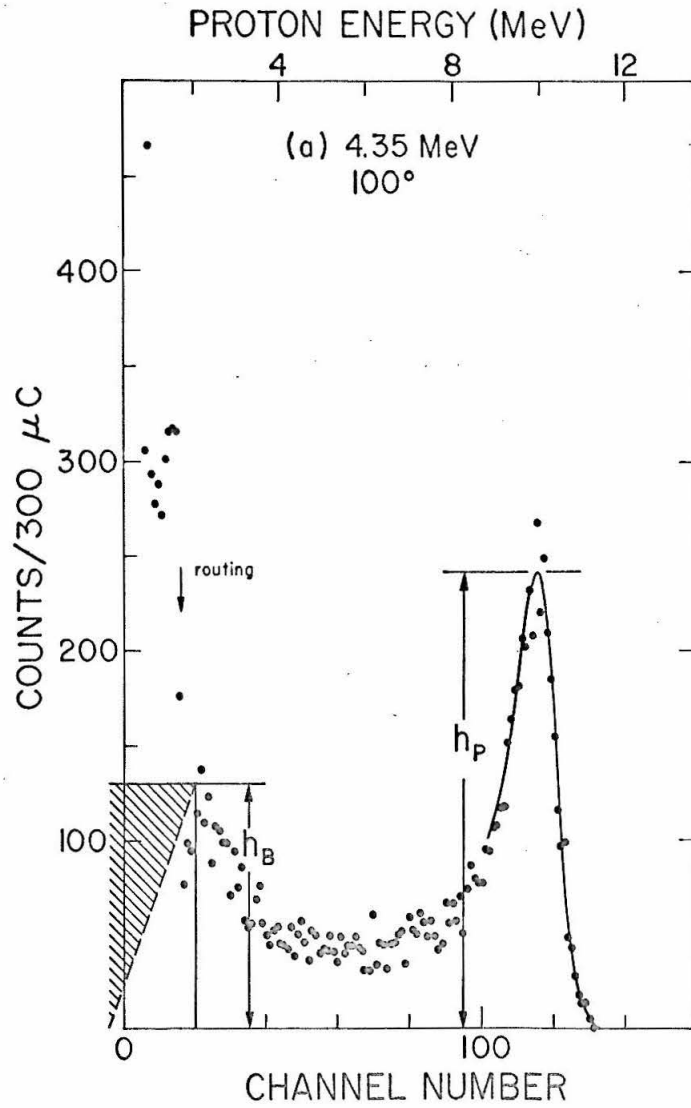


FIGURE 26

Angular Distributions for Charge 1 Yield

Angular distributions based on the yield of particles with charge 1 are shown for 2.81, 4.35 and 5.92 MeV. The indicated errors are determined mainly by the uncertainty in the low energy extrapolation. See the caption for Figure 25 and pages 42 and 43.

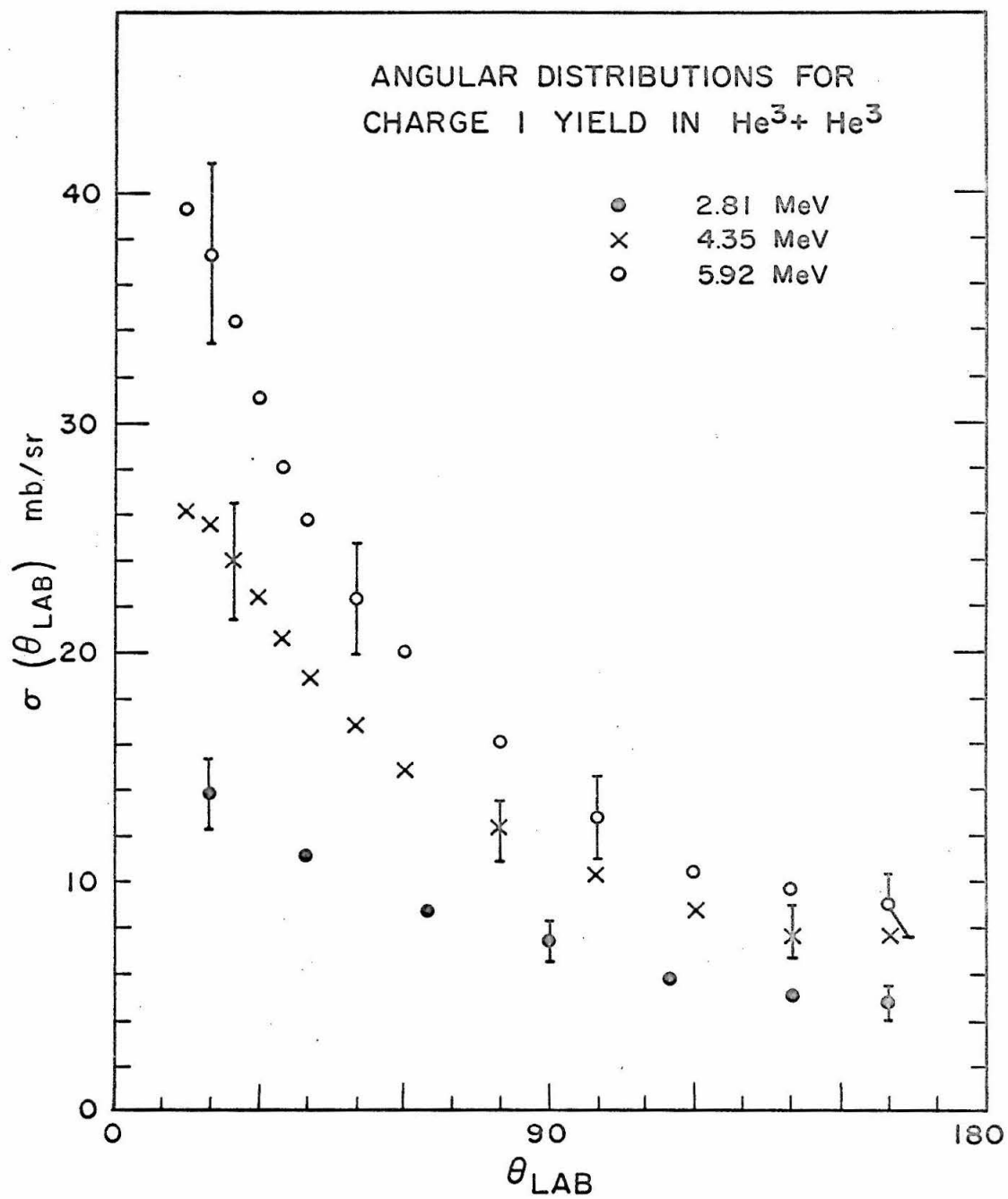


FIGURE 27

Angular Distribution for Charge 1 Yield

Angular distributions of the charge 1 yield are shown for 7.95, 9.94 and 11.93 MeV. There is a vertical offset of 10 mb/sr and 20 mb/sr respectively for the latter two energies. The indicated errors are determined mainly by the uncertainty in the low energy extrapolation. See the caption for Figure 25 and pages 42 and 43.

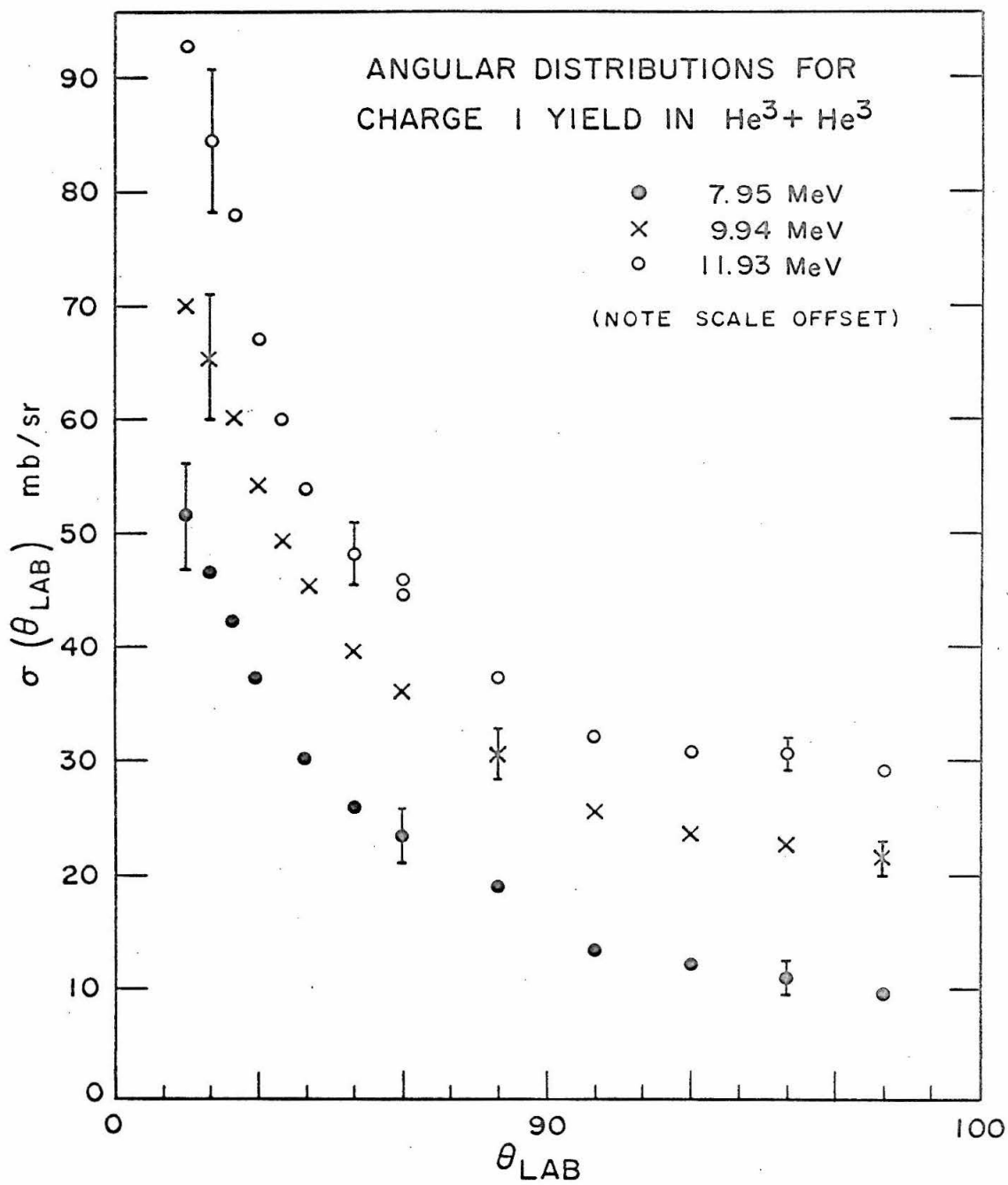


FIGURE 28

Angular Distribution for Charge 1 Yield

Angular distributions of the charge 1 yield are shown for the high pressure gas cell measurements at 13.81, 15.55 and 18.01 MeV. There is a vertical offset of 10 mb/sr and 20 mb/sr respectively for the latter two energies. As before, the indicated errors are determined mainly by the uncertainty in the low energy extrapolation. The effect of other reaction mechanisms on the yield is particularly evident in the sharp increase of the differential cross section at forward angles. See the caption for Figure 25 and pages 42 and 43.

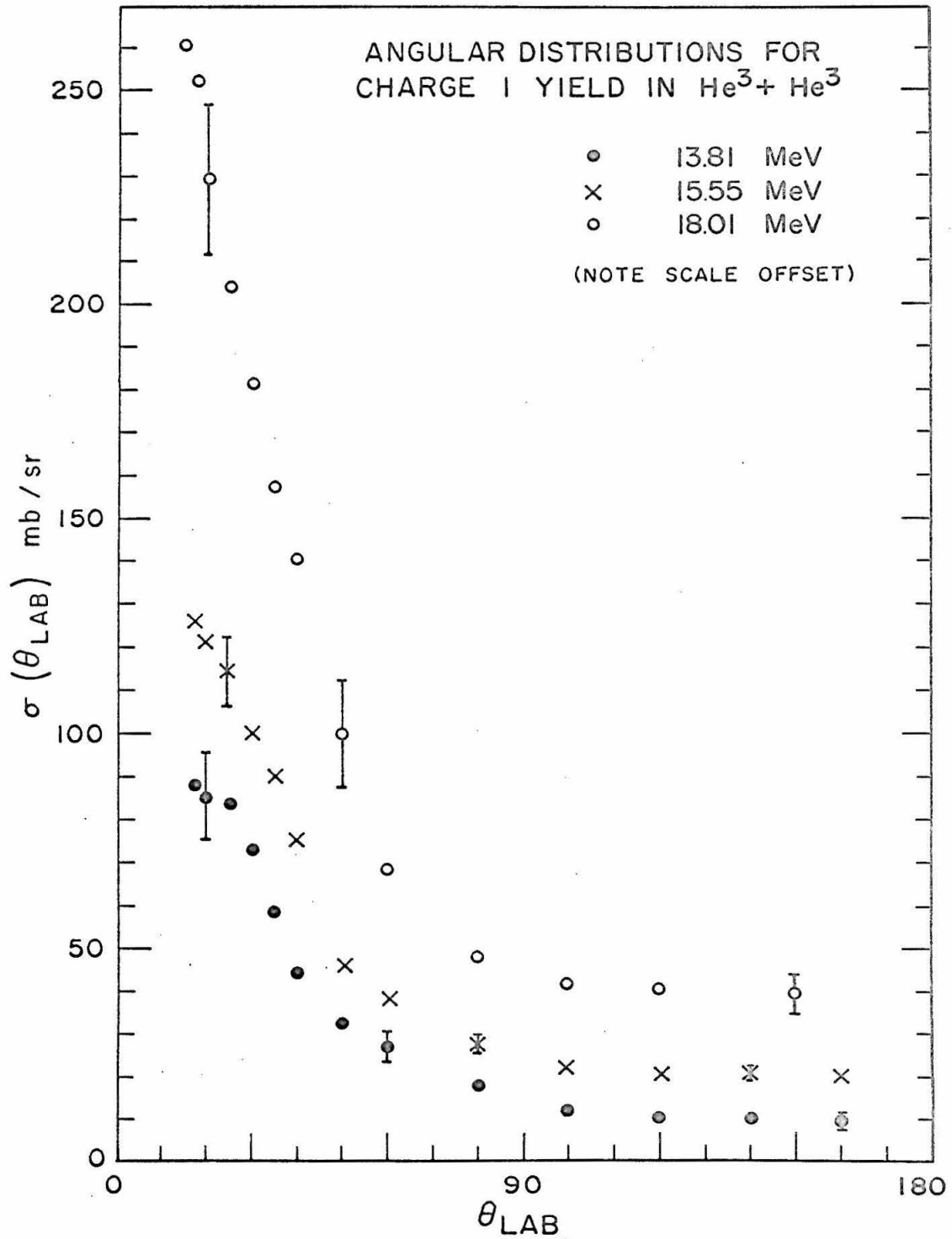


FIGURE 29
Total Cross Section for Charge 1 Particles

This figure gives the total cross section (note the log scale) for charge 1 particles as a function of the He^3 bombarding energy. These were obtained by determining the area under curves fitted to the measured angular distribution and then dividing by 2 (the number of charge 1 particles produced in the final state for each reaction). The errors indicated are derived from the relative errors assigned to each point of the angular distributions. They are determined mainly by the uncertainty in extrapolating each of the spectra to zero energy. The values of these total cross sections are given in Table IV.

The threshold for the production of deuterons in the reaction $\text{He}^3(\text{He}^3, d)\text{pHe}^3$ is indicated at 10.98 MeV. Below this point the only reaction channel open is $\text{He}^3(\text{He}^3, 2\text{p})\text{He}^4$. For further details see pages 42, 43 and 44.

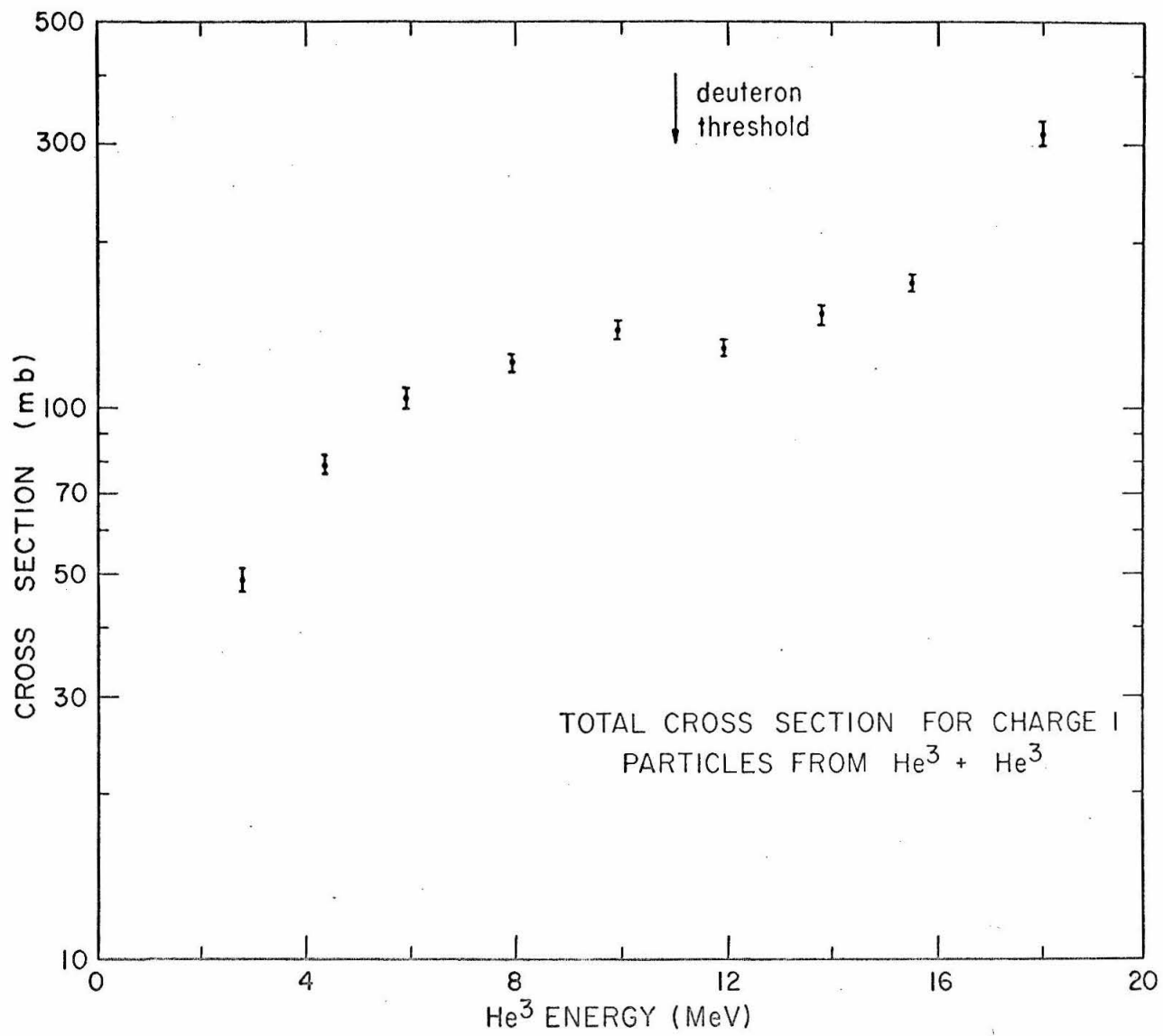


FIGURE 30
Total Cross Section Ratios

The ratio of the total cross section for the production of charge 1 particles to the cross section derived from the Li^5 ground state model is plotted as a function of He^3 bombarding energy. For the points below 12 MeV this ratio is consistent with the average value 1.19. The departure of this ratio from unity could be accounted for by systematic errors in the low energy extrapolations and in the calculations of the spectral shapes. Above 12 MeV the presence of other reaction channels and mechanisms producing particles with charge 1 in the final state is evident. The values of these ratios are given in Table V. For further discussion see pages 44, 45 and 52.

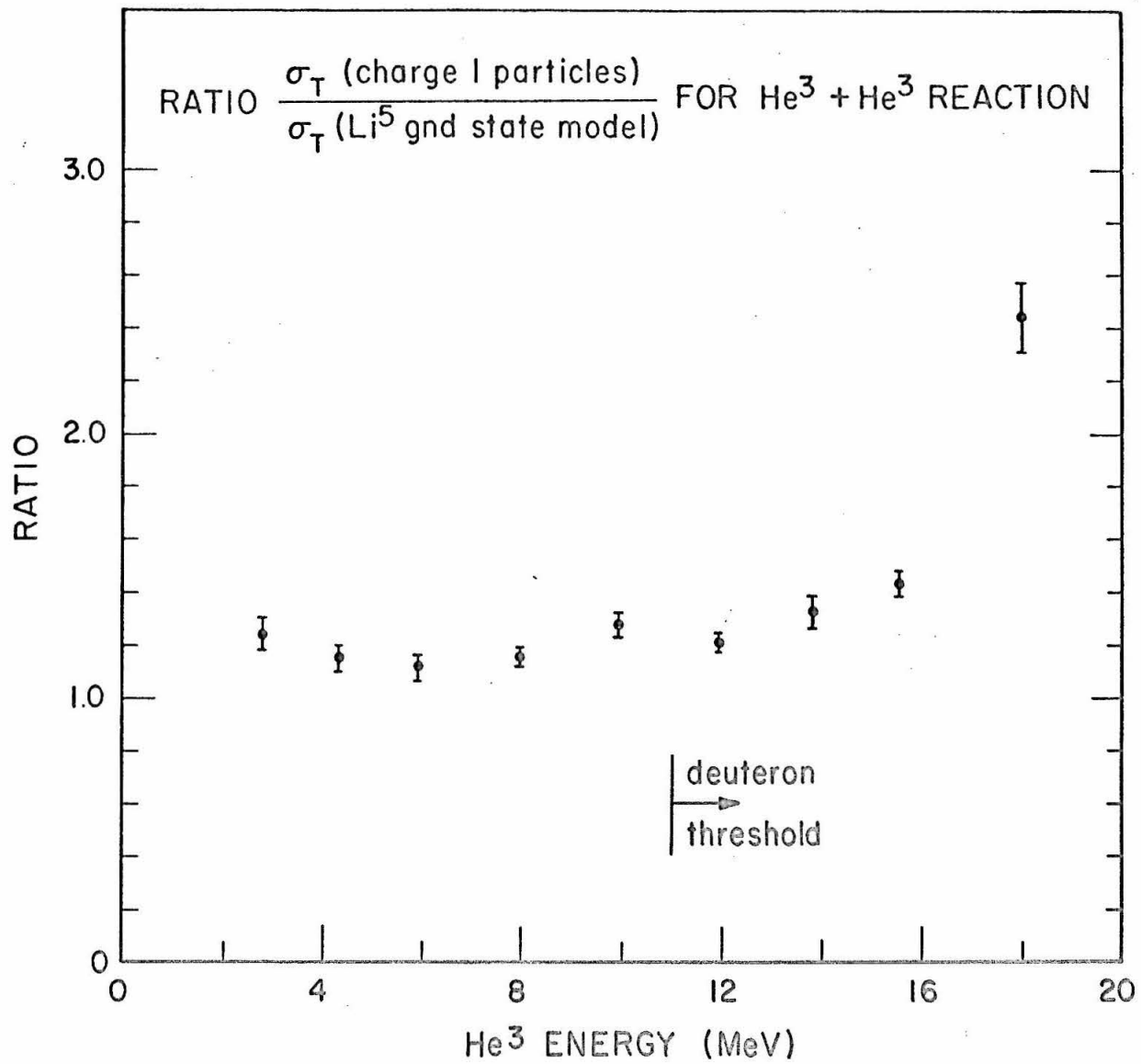


FIGURE 31

Comparison of Angular Distributions at 2.81 MeV

This figure gives a direct comparison of the shapes of the angular distributions at a He^3 bombarding energy of 2.81 MeV for the total proton cross section (protons are the only charge 1 particle produced at this energy) and the Li^5 ground state transition. The differential cross section in the laboratory system is plotted here as a function of $\cos \theta_{\text{LAB}}$ to show that the physical region is adequately covered by the angular distributions. Note the inset on the abscissa for the values of (+1) and (-1). For further discussion see page 45.

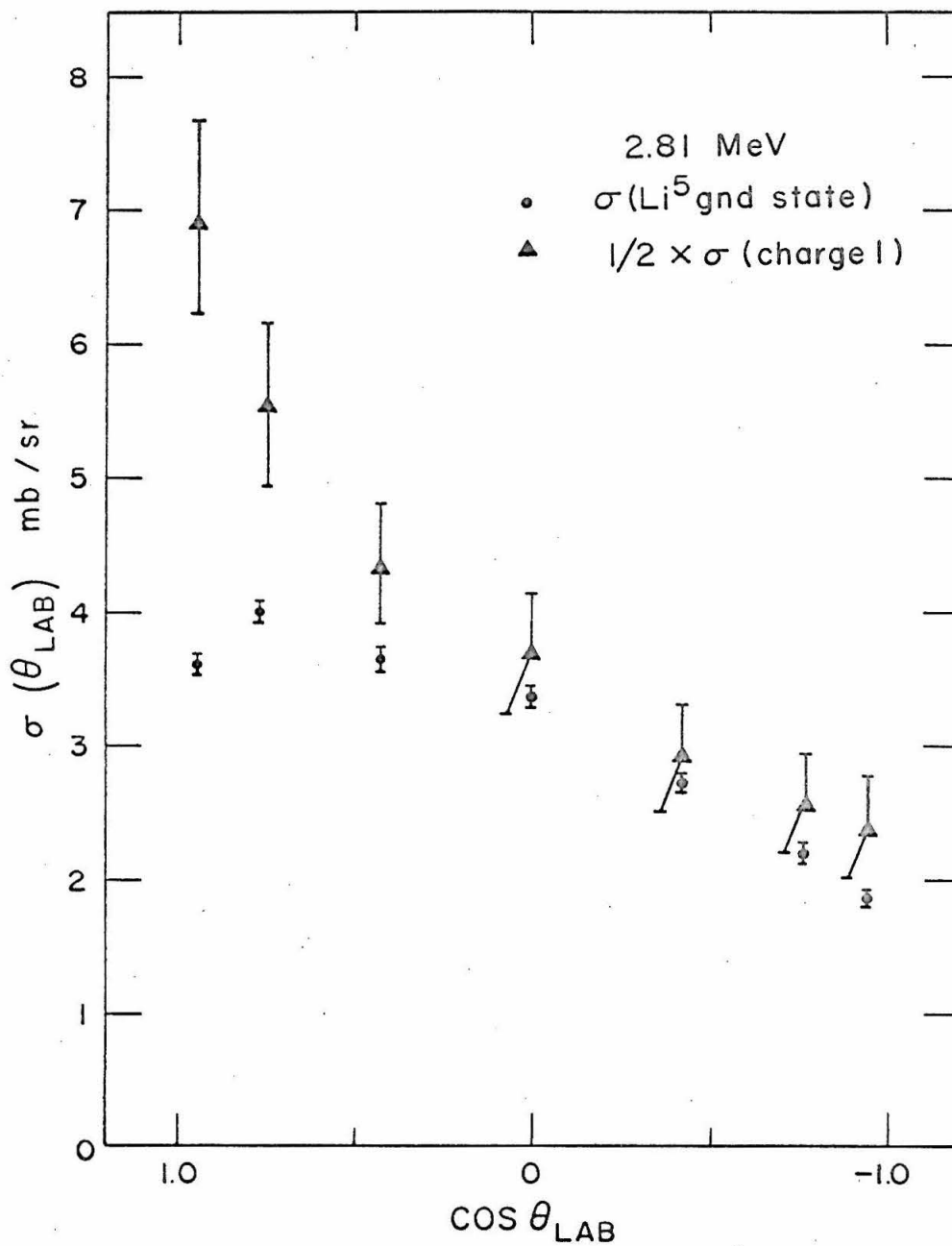
ANGULAR DISTRIBUTIONS FOR TOTAL PROTON
CROSS SECTION AND Li^5 GROUND STATE MECHANISM

FIGURE 32

Alpha-Particle Spectrum at 12 MeV, 10^0

The momentum spectrum of alpha particles is plotted as a function of the NMR frequency (proportional to the particle momentum) of the 61-cm magnetic spectrometer for 11.96 MeV and 10^0 . The entrance slits of the magnet defined a θ -resolution of $\pm 1.0^0$ and particles were detected with a sixteen-counter array positioned along the focal plane. The energy scale at the top of the figure gives the corresponding alpha-particle energy at the center of the gas target. Some typical statistical errors are indicated.

The sharp peak at high frequency (41 Mc/sec) is due primarily to the singlet p-p final state interaction and the smooth curve represents a preliminary fitting with the Watson-Migdal sequential-decay formalism. The excitation energy in the 2p system is indicated in MeV. The broad peak around 37 Mc/sec is due to the p-He⁴ final state interaction (i. e., the ground state of Li⁵). The arrow indicates the maximum alpha-particle energy expected if this state were sharp.

The three sharp peaks are due to slight contaminants in the He³ target gas. Peak (2) corresponds to recoil alphas from an 0.4% He⁴ contaminant. Peaks (3) and (1) are due to $O^{16}(\text{He}^3, \alpha)O^{15}$ reactions to the ground state and 6.16 MeV state of O^{15} , respectively.

For further details see pages 47, 48 and 78.

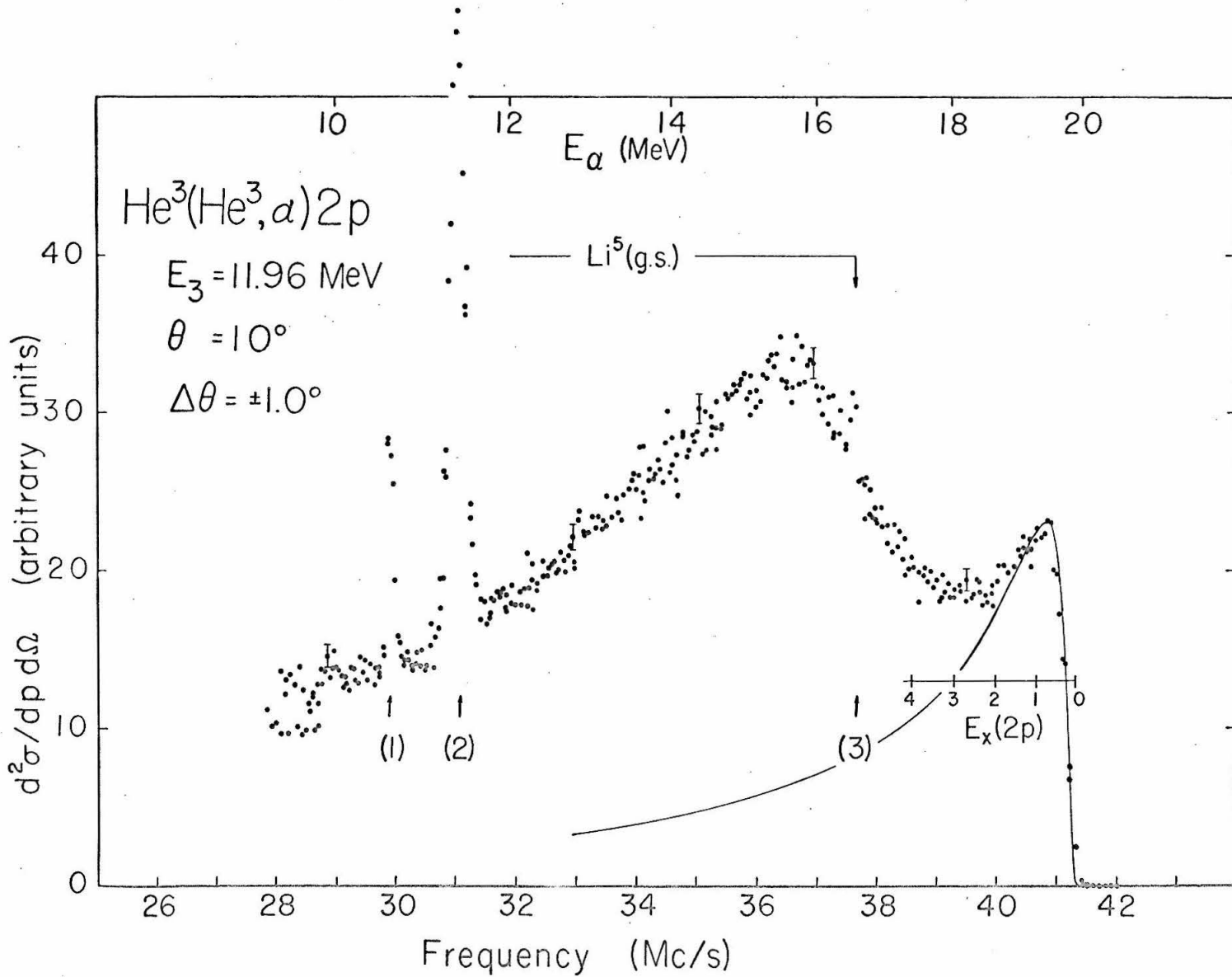


FIGURE 33

Alpha-Particle Spectrum at 12 MeV, 15°

The momentum spectrum of alpha particles is plotted as a function of the NMR frequency for 11.96 MeV and 15° . As in Figure 32 the energy scale gives the alpha-particle energy corrected to that at the center of the gas target. The peaks labeled (1) and (2) are due respectively to the $O^{16}(He^3, \alpha)O^{15}$ reaction to the 6.16 MeV state in O^{15} and to recoil alphas from a slight He^4 contaminant.

The singlet p-p final state interaction is again evident near 40 Mc/sec and the broad peak around 35 Mc/sec is due to alpha particles from the Li^5 ground state.

For further discussion see pages 47, 48 and 78.

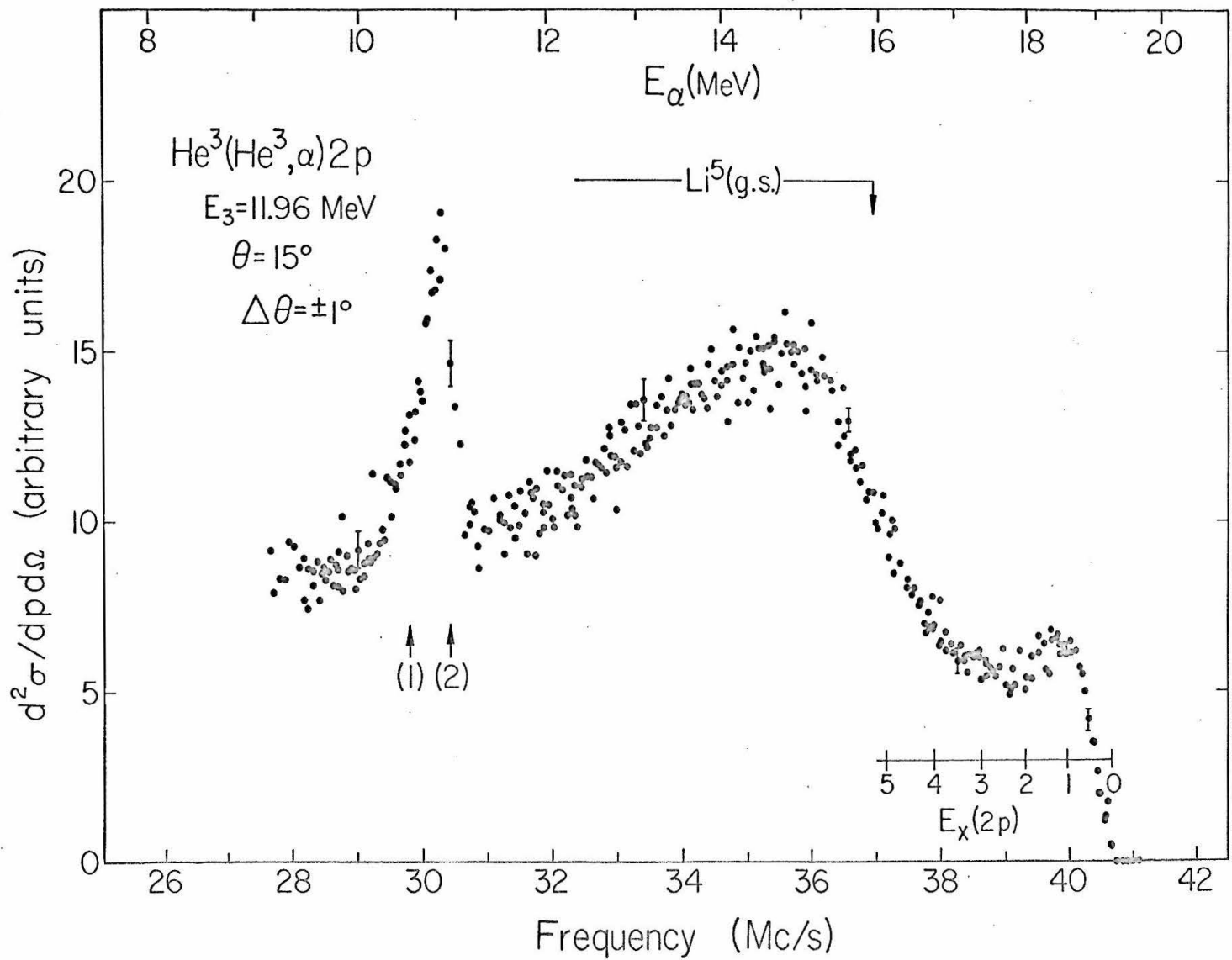


FIGURE 34

Alpha-Particle Spectrum at 12 MeV, 30°

The momentum spectrum of alpha particles is plotted as a function of the NMR frequency for 11.96 MeV and 30° . As in Figure 32 the energy scale gives the alpha-particle energy corrected to that at the center of the gas target. Peaks corresponding to the contaminant reactions are no longer visible.

In this case the smooth curve is intended as a guide to the general trend of the data points. The peaking at the high frequency end of the spectrum due to the singlet p-p interaction is barely discernible. The broad structure corresponds to alpha particles from the Li^5 ground state.

For further discussion see pages 47, 48 and 78.

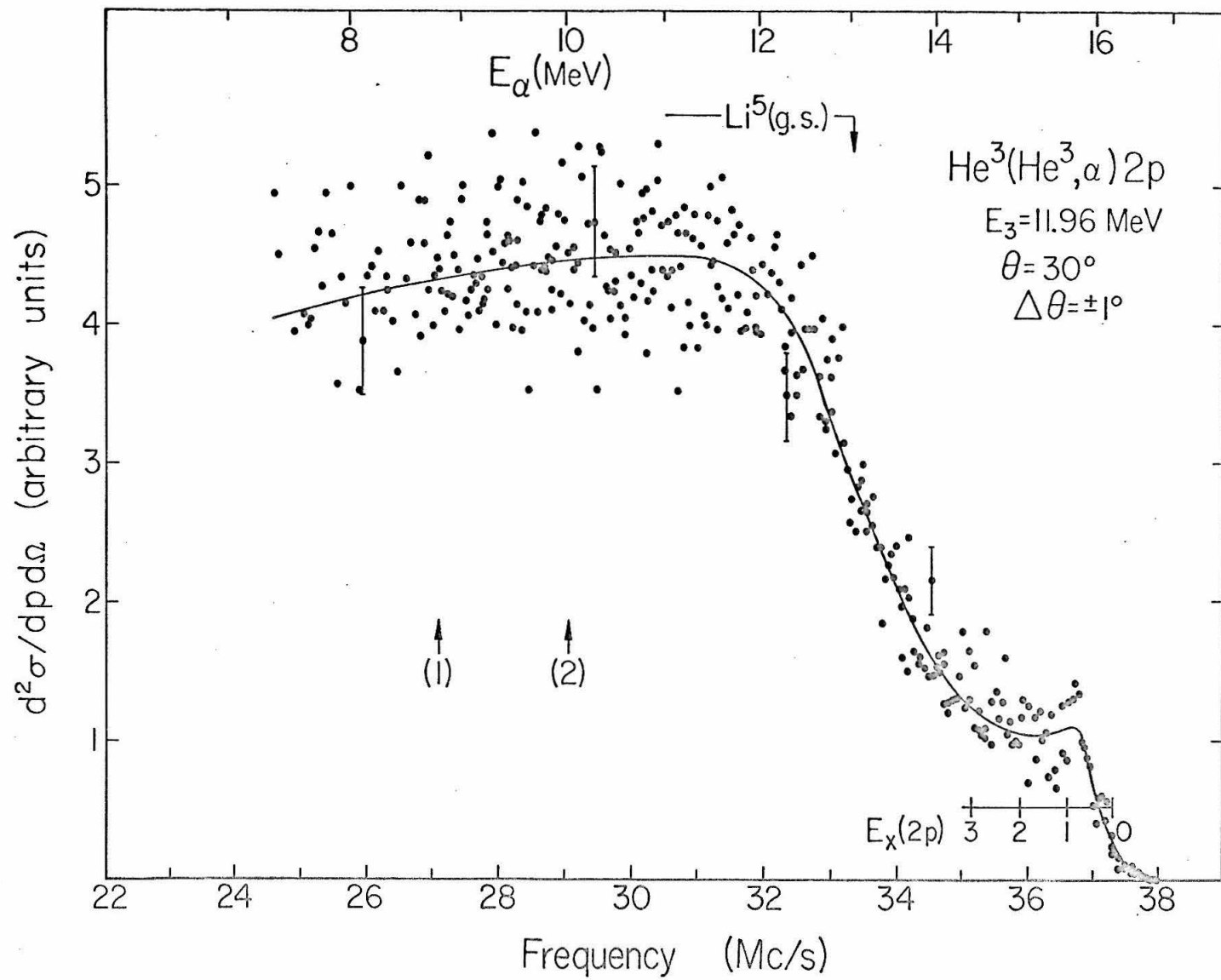


FIGURE 35

Energy Spectra of Alpha Particles at 12 MeV

The energy spectra of alpha particles for the laboratory angles 10° , 15° and 30° at 11.96 MeV are plotted together for comparison as a function of alpha-particle energy at the center of the gas target. The curves were obtained from smooth curves drawn through the original momentum spectra (see Figures 32-34). The error bars correspond to the statistical errors of individual points of the momentum spectra and therefore are considerably larger than the deviations expected in the averaged smooth curve. The relative normalization of the three curves has been adjusted for the different target thicknesses seen at each angle. For further discussion see pages 47, 48 and 78.

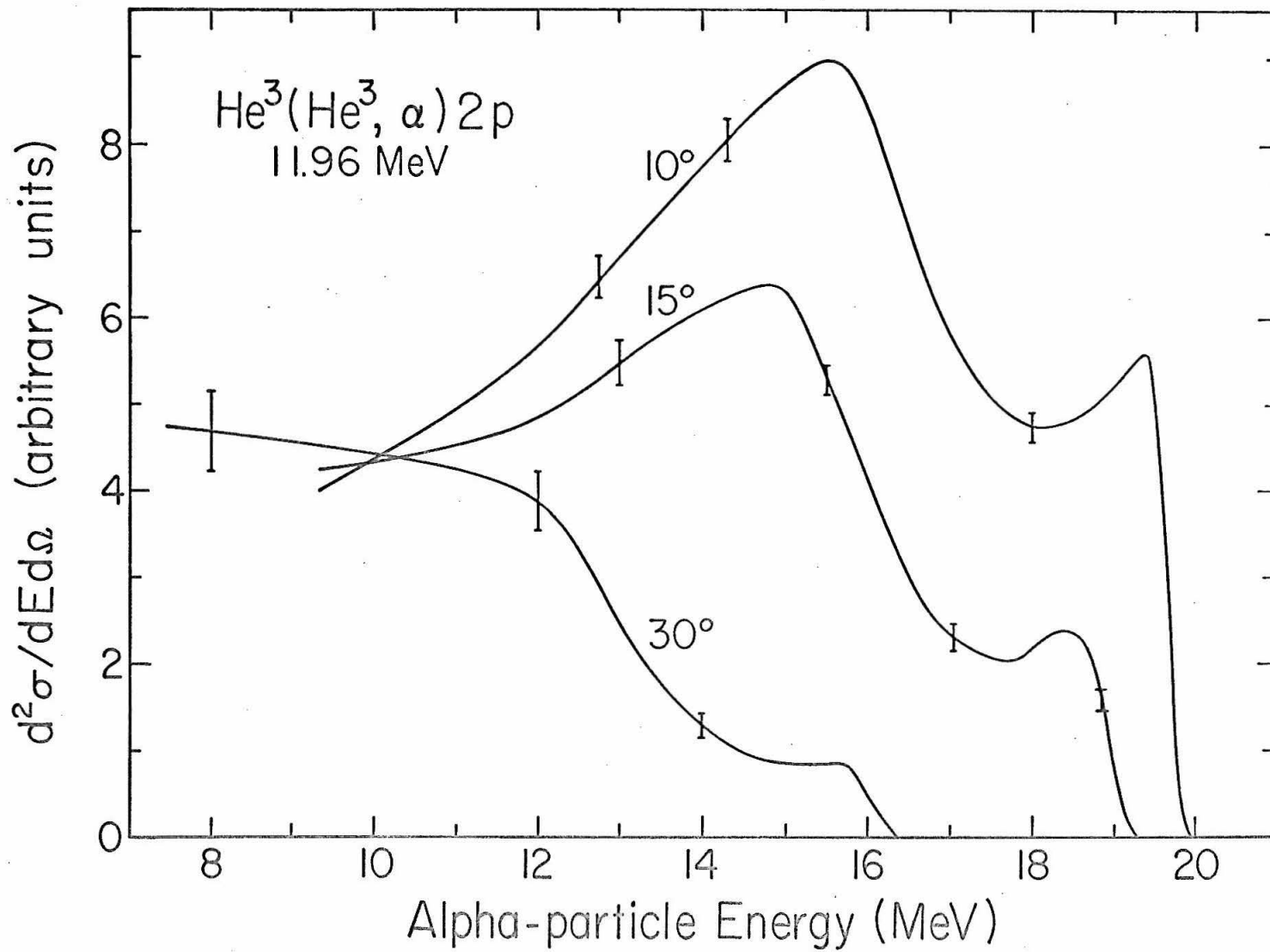


FIGURE 36

Alpha-Particle Spectrum at 18 MeV, 6°

The momentum spectrum of alpha particles is plotted as a function of the NMR frequency for 17.87 MeV and 6° . Particles were detected with the sixteen-counter array down to 34 Mc/sec, the frequency corresponding to the He^3 beam energy. Below this frequency points were taken at wider intervals with a single detector. The energy scale at the top of the spectrum gives the alpha-particle energy corrected to the center of the gas target. The peaks labeled (1) and (2) are due to the $\text{O}^{16}(\text{He}^3, \alpha)\text{O}^{15}$ reaction to the 6.16 MeV state in O^{15} and to recoil alphas from a slight He^4 contaminant.

The singlet p-p interaction dominates the high frequency end of the spectrum and at this extreme forward angle of 6° it is higher than the broad peak near 42 Mc/s due to the p- He^4 interaction (Li^5 ground state).

For further discussion see pages 47, 48 and 78.

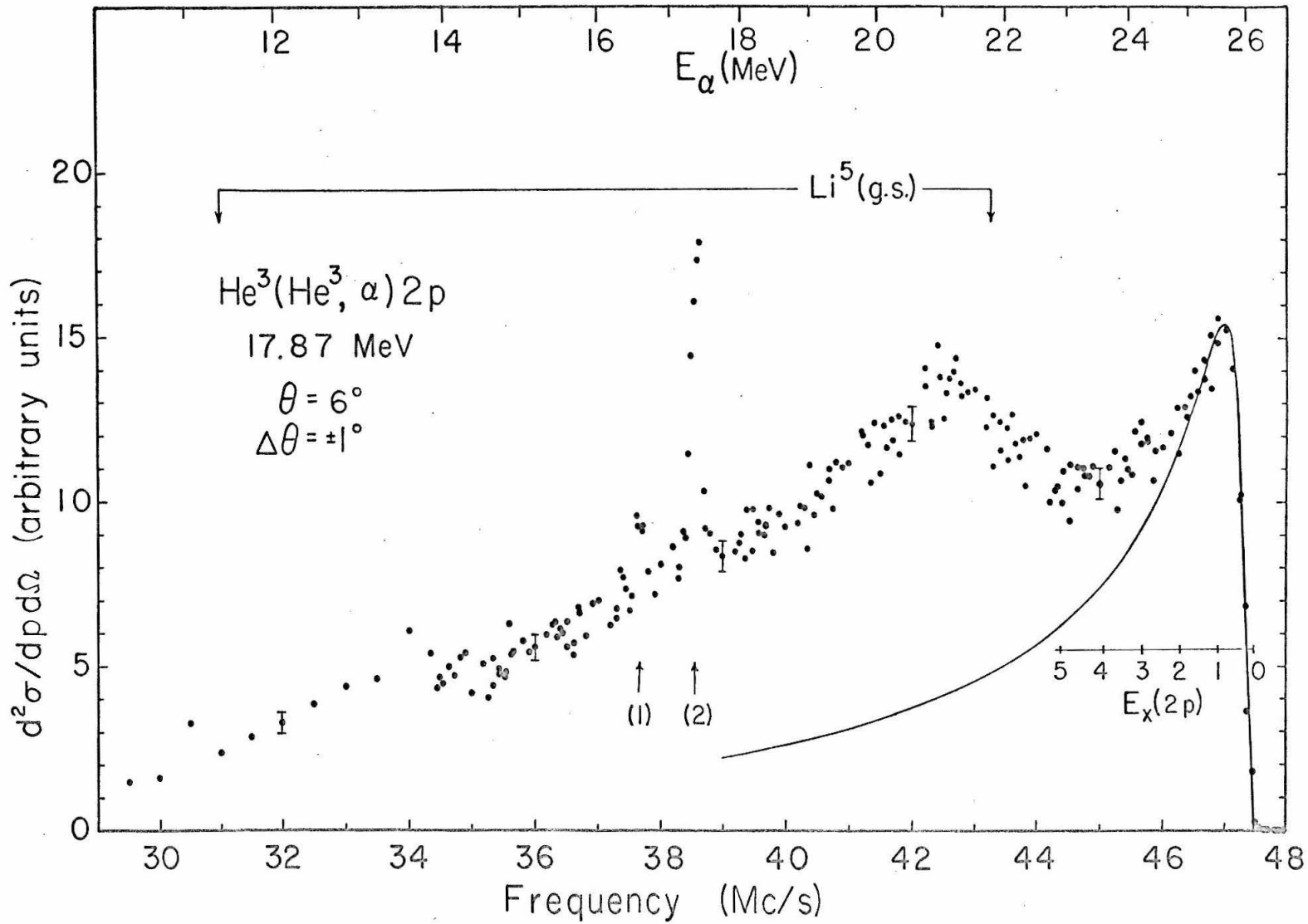


FIGURE 37

Recoil Spectrum Calculations at 12 MeV, 10^0

This figure indicates the results of a calculation of the recoil alpha-particle spectrum at 11.96 MeV and 10^0 based on a simple sequential decay model. The alpha spectrum is assumed to consist of two parts which have been added incoherently; alpha particles from the breakup of the Li^5 ground state and alpha particles from the singlet p-p interaction.

The light solid line represents the calculated spectrum; the two constituents of this spectrum are also indicated. This was normalized to the heavier line representing the experimental distribution by requiring the mixture of the individual components (as labeled) that would match the observed spectrum at the two peaks (15.5 and 19.35 MeV).

An additional variable in the p + Li^5 (ground state) component is the angular distribution of the breakup of the Li^5 in its own center-of-mass system. In order to fit the sharp trailing edge of the observed spectrum, a distribution for the alpha particles of $(1 + 0.875 \cos \theta_R)$ with respect to the recoil axis was required. The dashed curves show how the trailing edge is affected by taking the coefficient of $\cos \theta_R$ equal to 0.75 and 1.0. Above the peak at 15.5 MeV the three curves merge.

For further discussion see pages 36, 49, 50 and 78.

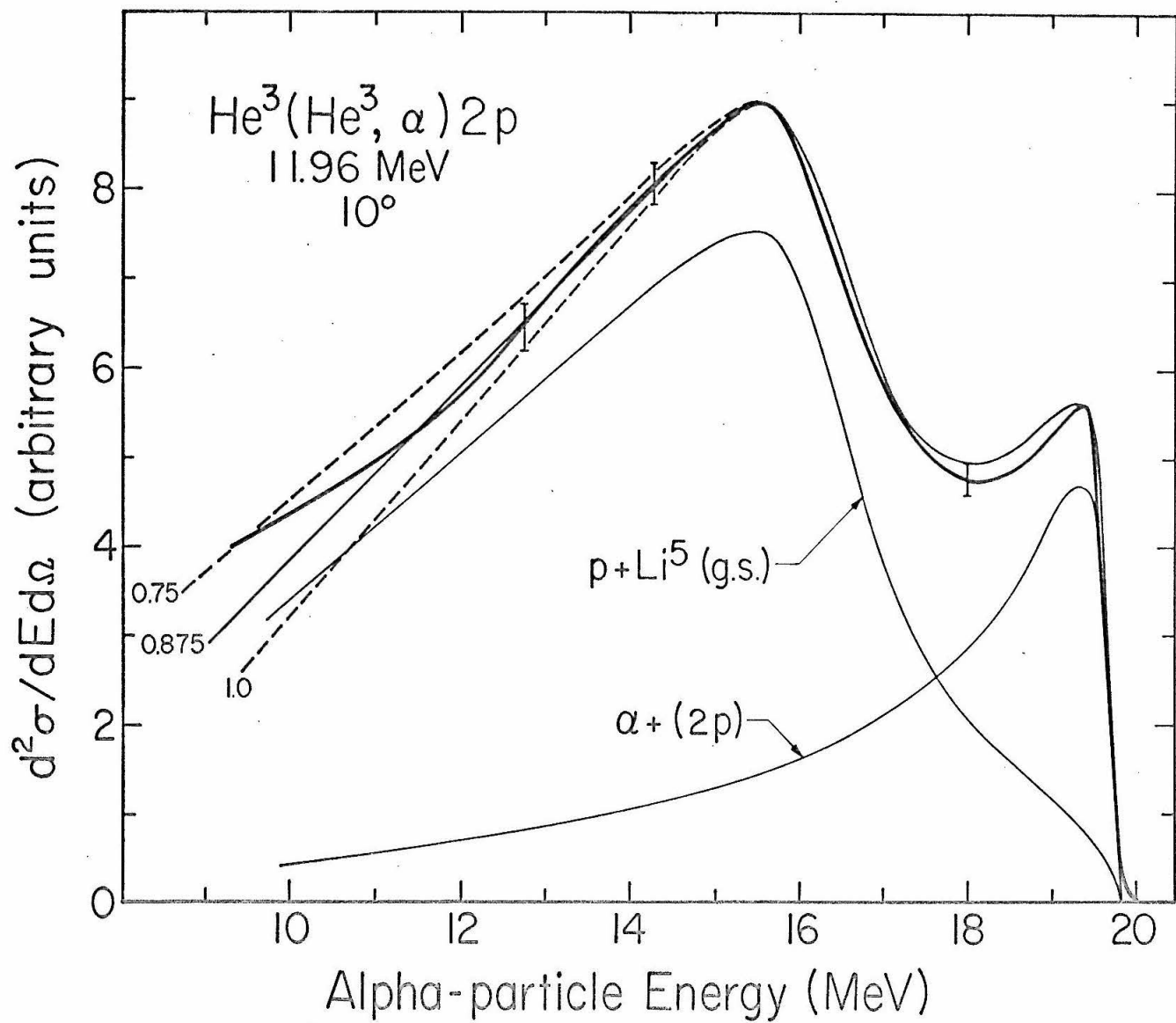


FIGURE 38

Recoil Spectrum Calculations at 12 MeV, 15° and 30°

Calculations of the alpha-particle spectra are compared with the observed distributions at 11.96 MeV for 15° and 30° . As in Figure 37 the heavy solid lines represent the experimental distributions and the lighter solid and dashed curves represent the calculated spectra.

In the 15° spectrum calculations are shown for coefficients of $\cos\theta_R$ of 0.625, 0.75 and 0.875. The light curve indicates the contribution of the singlet p-p mechanism which is independent of this breakup parameter.

In the 30° spectrum the shape of the experimental distribution has changed considerably and it appears to correspond more closely to an almost isotropic breakup of the Li^5 . The predicted shape for a breakup of $(1 + 0.875 \cos\theta_R)$ is also shown for comparison.

For further discussion see pages 36, 49-51 and 78.

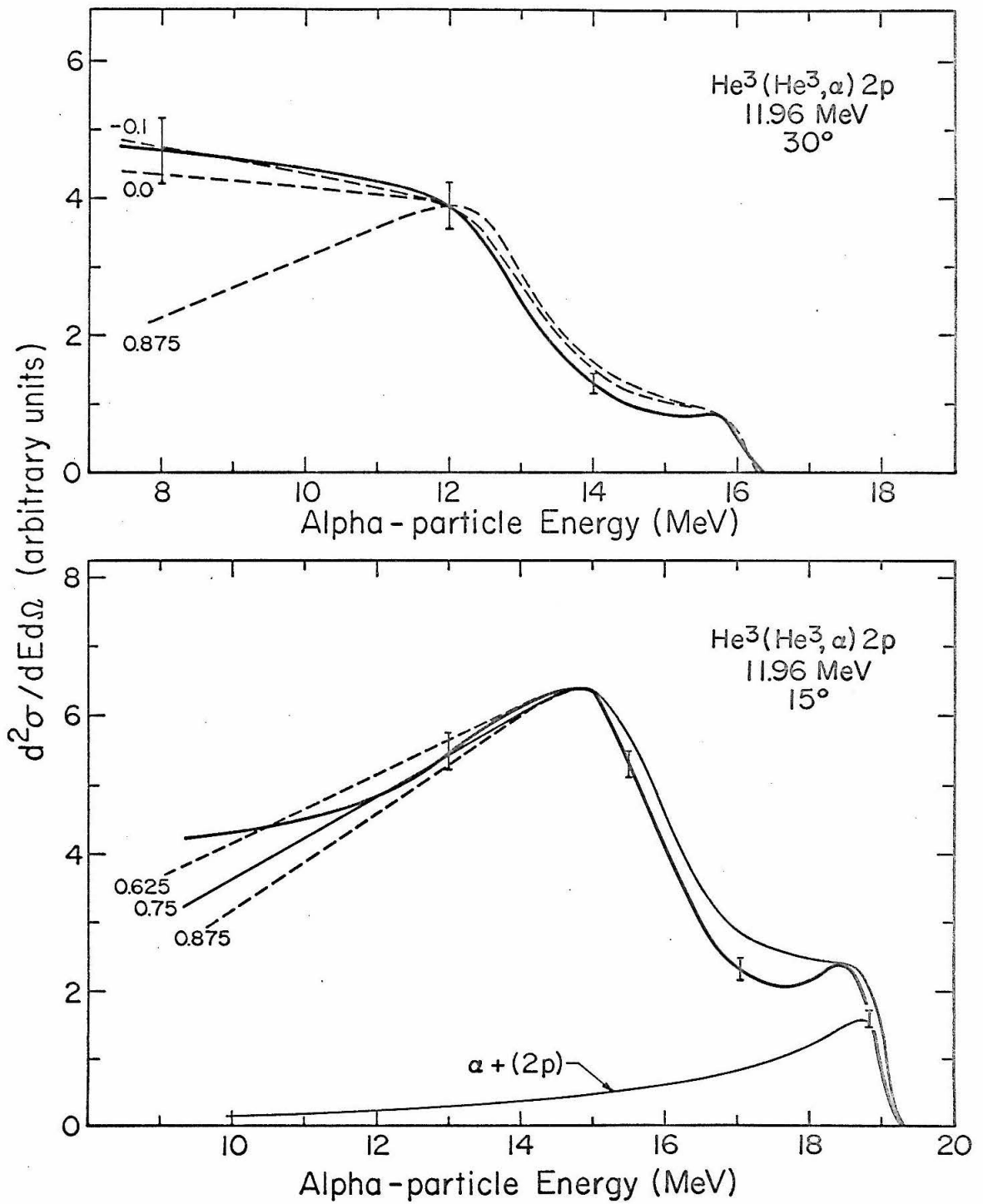


FIGURE 39

Recoil Spectrum Calculations at 18 MeV, 6° and 15°

The energy spectra of alpha particles are shown for the two angles 6° and 15° at a He^3 bombarding energy of 17.87 MeV. The heavy lines represent the experimental distributions at each angle and the dashed lines indicate the calculated spectra. These have been normalized to fit the data at the peaks due to the p-p interaction and the Li^5 ground state.

The curvature in the trailing edge of the 6° spectrum can be reproduced by including a small amount of $\cos^2\theta_R$ in the recoil breakup. The calculated spectrum shape includes a breakup of $(1 + 0.875 \cos\theta_R + 0.3 \cos^2\theta_R)$ in that part of the spectrum due to the Li^5 reaction mode.

In the 15° spectrum the presence of the p-p interaction is barely perceptible in the high energy shoulder. The calculated spectrum includes a breakup distribution of $(1 + 0.2 \cos\theta_R)$ in the Li^5 portion.

For further details see pages 49 and 51.

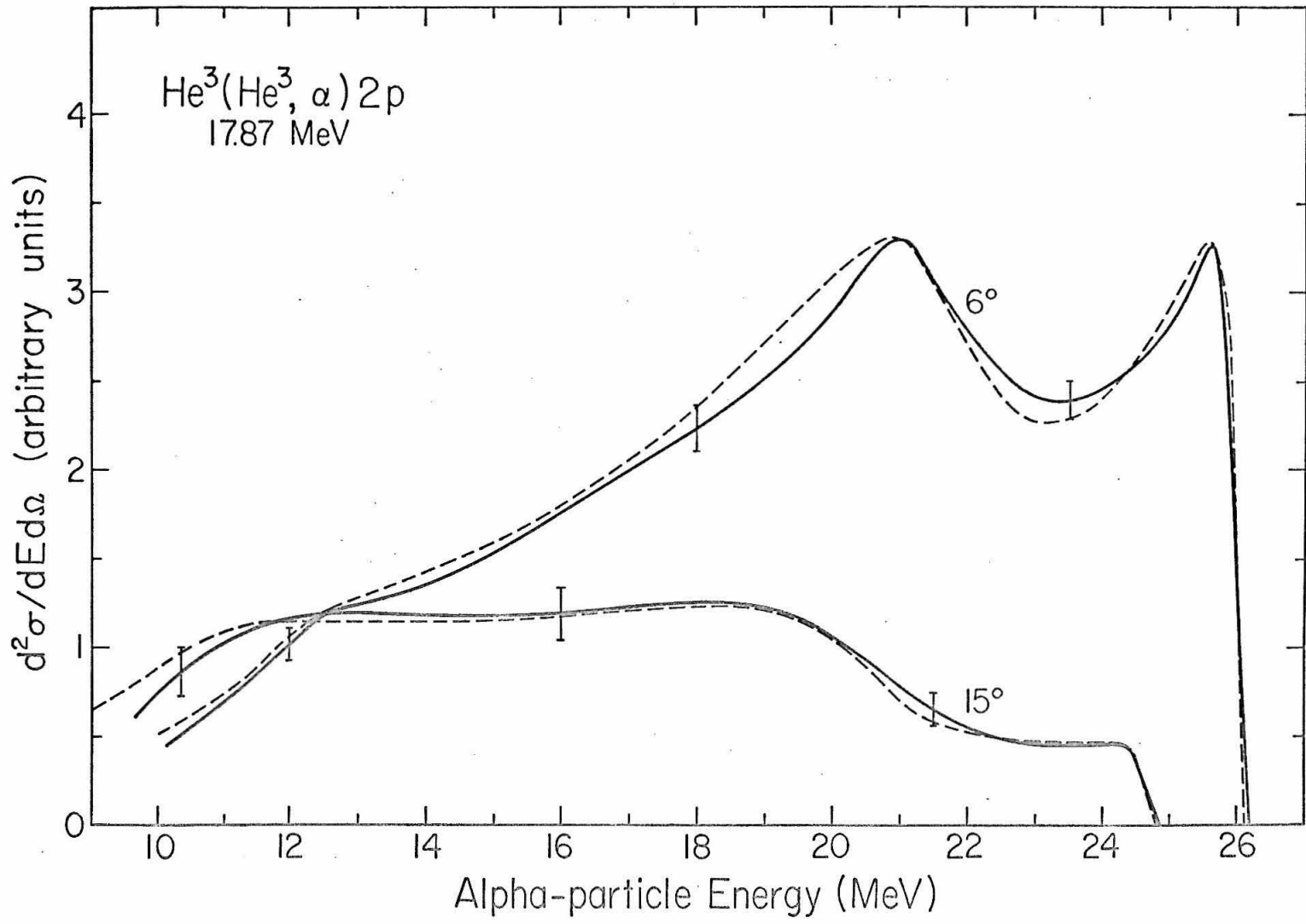


FIGURE 40

Ratio of (2p) and Li^5 Mechanisms

This figure indicates the relative importance of the $\text{He}^4 + 2\text{p}$ and $\text{Li}^5 + \text{p}$ reaction mechanisms as determined by calculations of the alpha-particle spectra at forward angles. The spectrum calculations construct the laboratory energy spectrum, $h(E, \theta)$, from the calculated energy spectra for the Li^5 mechanism, $f(E, \theta)$, and the 2p mechanism, $g(E, \theta)$. The calculated spectrum for each lab angle θ is normalized to the experimental distribution at the positions of the two peaks E_{Li^5} (produced by the Li^5 mechanism) and $E_{2\text{p}}$ (produced by the 2p mechanism). The alpha spectrum is taken to be

$$h(E, \theta) = A(\theta)f(E, \theta) + B(\theta)g(E, \theta)$$

and no attempt has been made to allow for interference between the two reaction mechanisms.

Part (a) of the figure indicates the ratio of the two processes at their corresponding peak positions,

$$R_a = B(\theta) g(E_{2\text{p}}, \theta) / A(\theta) f(E_{\text{Li}^5}, \theta),$$

as a function of the laboratory angle.

Part (b) of the figure indicates the ratio of the numbers of observed alpha particles at each laboratory angle that can be attributed to each mechanism on the basis of the sequential decay model.

$$R_b = B(\theta) \int g(E, \theta) dE / A(\theta) \int f(E, \theta) dE .$$

It is important to note that neither of these ratios applies to the total number of reactions proceeding through each mechanism since each spectral shape at a given laboratory angle involves contributions from a wide range of center-of-mass angles. For further discussion see pages 51 and 52.

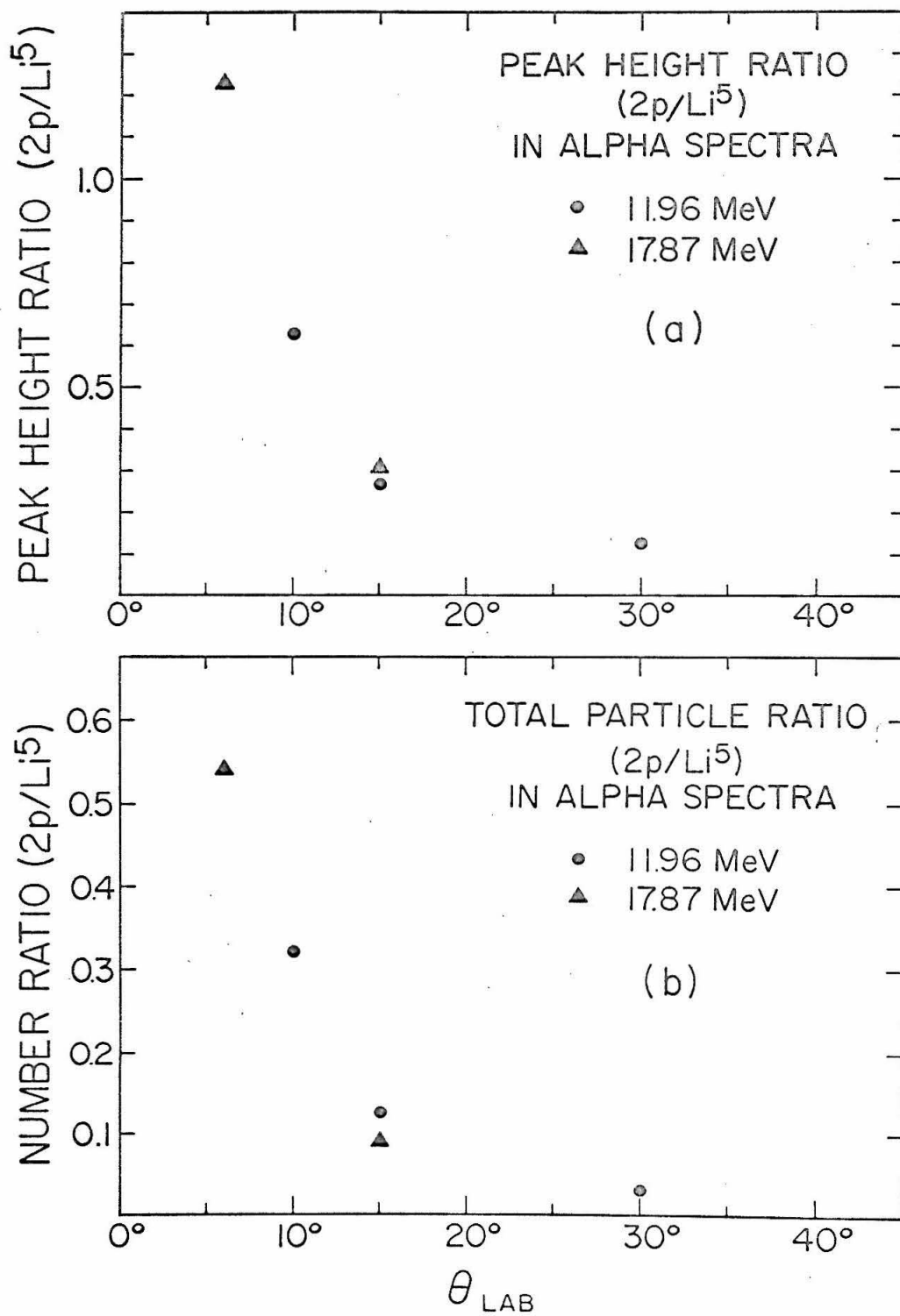


FIGURE 41

Deuteron Spectrum at 18 MeV, 6° and 15°

The momentum spectrum of deuterons from the reaction $\text{He}^3(\text{He}^3, \text{d})\text{p} + \text{He}^3$ is plotted as a function of NMR frequency for a bombarding energy of 17.87 MeV and laboratory angles of 6° (solid dots) and 15° (open circles). The deuteron energy corrected to the center of the gas target is given along the top. The 15° data have been reduced by 1/4 to enable it to be included on the same figure.

Several other items are given which refer only to the 6° measurements. For this data a scale indicates the excitation in the $\text{p} + \text{He}^3$ (or Li^4) system. The arrow indicates the maximum deuteron energy possible at 6° for deuterons produced by a sequential decay leading through the 16.64 MeV state in Li^5 ; that is, $\text{He}^3(\text{He}^3, \text{p})\text{Li}^{5*}(\text{d})\text{He}^3$. The dashed line represents the three-particle phase-space prediction. The solid line gives the prediction of a Watson-Migdal sequential decay model using the unsplit, p-wave, proton- He^3 scattering phase shift (Tombrello, 1962). The dash-dot line shows how one can improve on this latter fit by including (for example) an additional $\ell_3 = 2$ interaction between the deuteron and the p-He^3 system.

For further details see pages 38, 53, 54, 75 and 78.

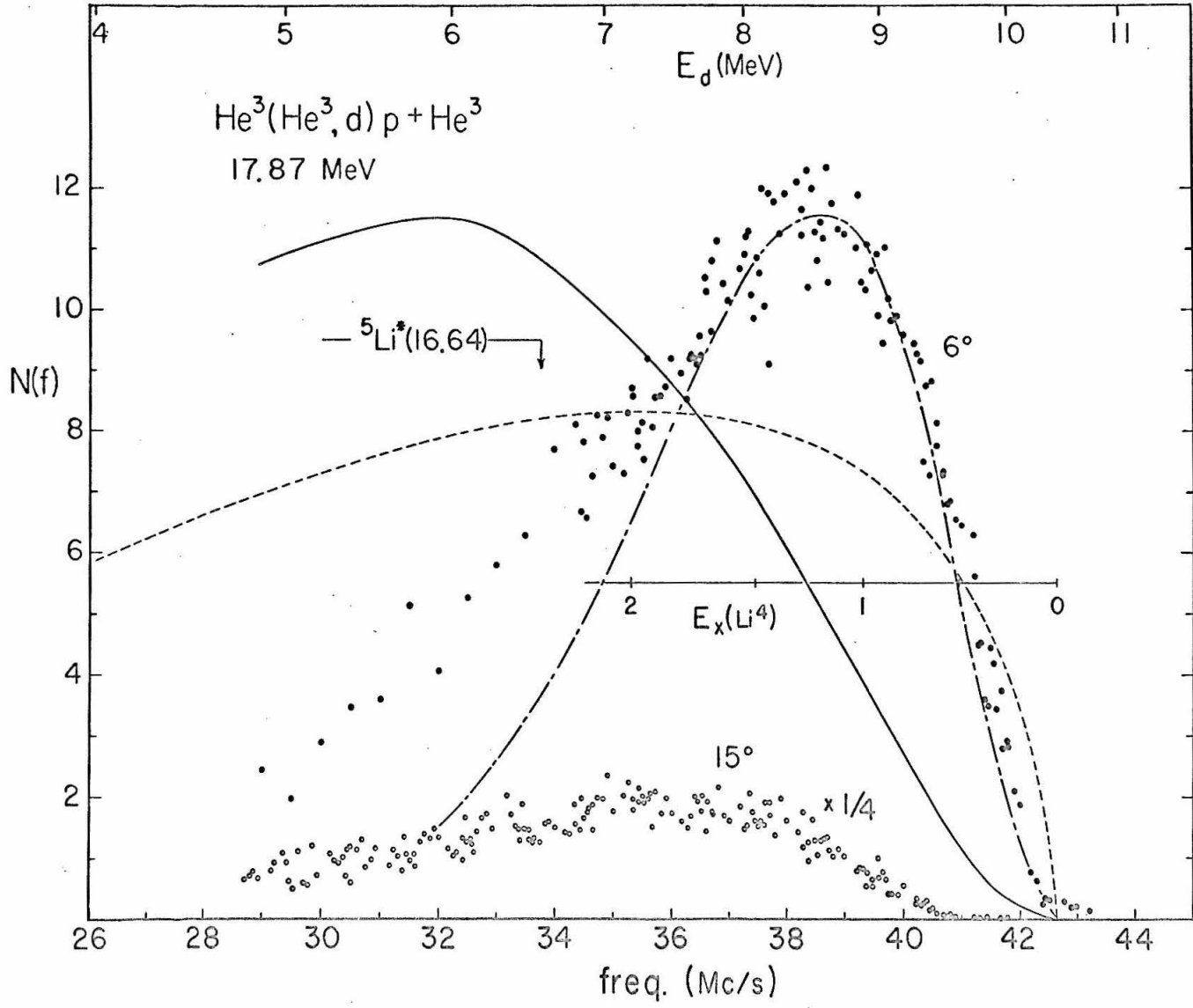


FIGURE 42

Triton Spectrum at 19.60 MeV, 4^0

Above the threshold energy of 13.9 MeV, tritons can be produced in the reaction $\text{He}^3(\text{He}^3, t)3p$. This figure shows the triton energy spectrum obtained at 19.60 MeV and 4^0 . The error bars represent the statistical uncertainty in each point. The data have been shown twice to facilitate a comparison with several theoretical predictions. A scale indicates the excitation in the $3p$ system, and the arrows indicate the maximum triton energies possible for tritons produced by sequential decay through excited states of He^4 at 20.0 and 21.2 MeV.

In the top figure the dashed curve represents the four-body phase-space distribution. The bottom figure shows the results of two sequential decay calculations in which He^4 is formed in its excited state at 20 MeV and then allowed to decay in flight into $t + p$. The dashed curve weights the $\text{He}^{4*}(20.0)$ recoil velocity by the three-body phase space. The solid curve weights it according to the 1S_0 p-p interaction. There does not appear to be any enhancement attributable to an interaction of three protons in the final state.

For further details see pages 55, 56, 75 and Appendix A.3.

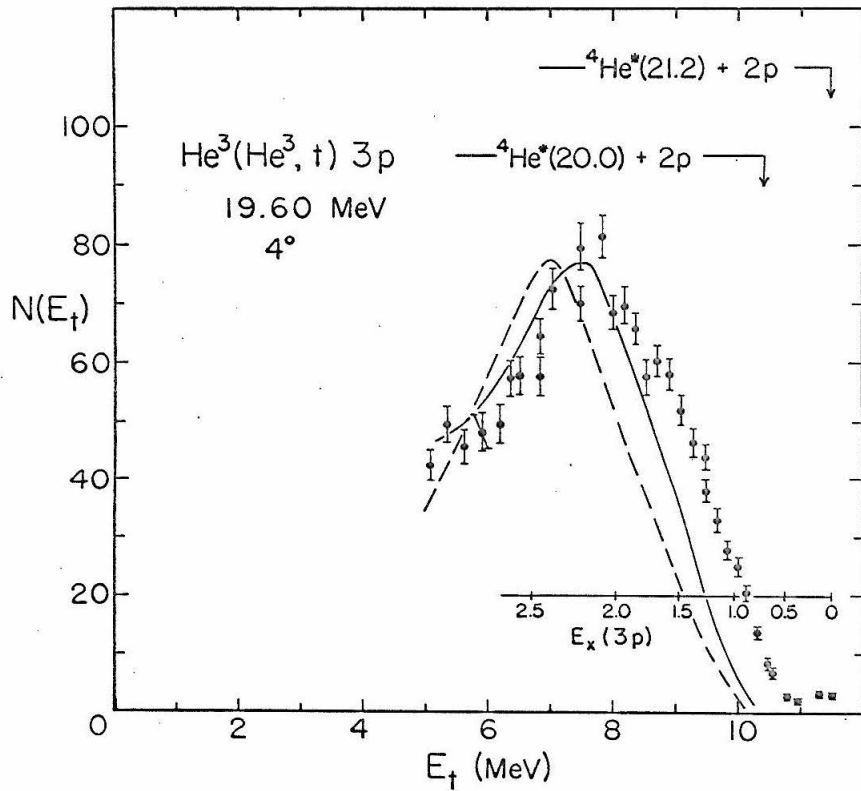
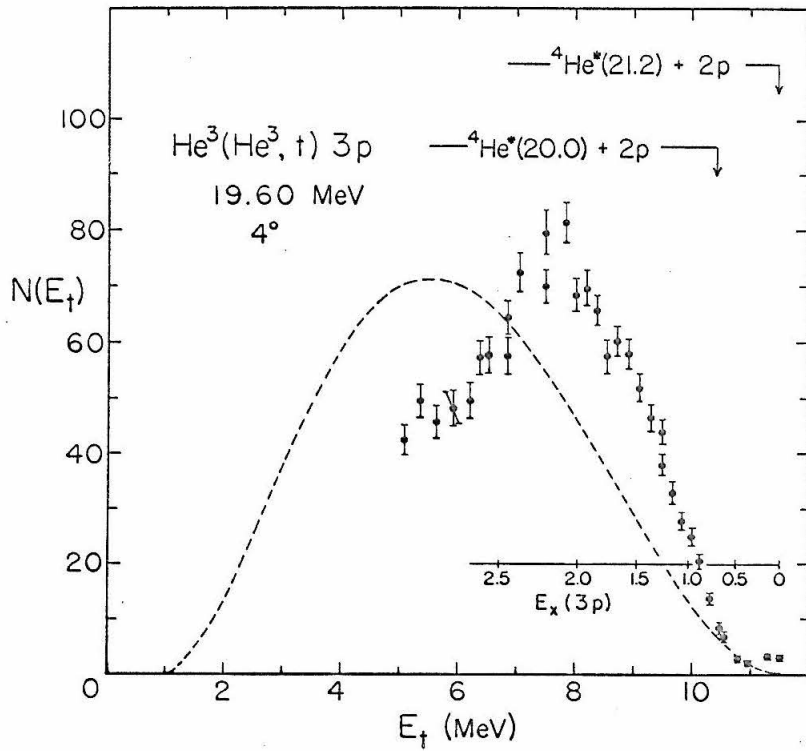


FIGURE 43

Kinematics of Coincidence Detection

In the case of a three-particle final state five independent variables remain after applying the conservation of energy and momentum. Measuring two particles in coincidence fixes three angles, hence the remaining two independent variables determine a curve of kinematically allowed events in the (E_3, E_4) plane. This figure shows the allowed curve (solid line) for a bombarding energy of 10 MeV with the detectors positioned to measure coincidences between alpha particles at -30° and protons at $+100^\circ$ (on opposite sides of the beam line). The calculations include the energy loss of the particles in the exit foil. The dotted curves indicate the spread introduced by the angular resolution of the detectors ($\pm 4^\circ$).

Points along the solid curve are characterized by a relative energy between any two particles in the final state. The two arrows represent points on the curve at which the p-He⁴ relative energy corresponds to the position of the Li⁵ ground state.

For further details see pages 57 and 58.

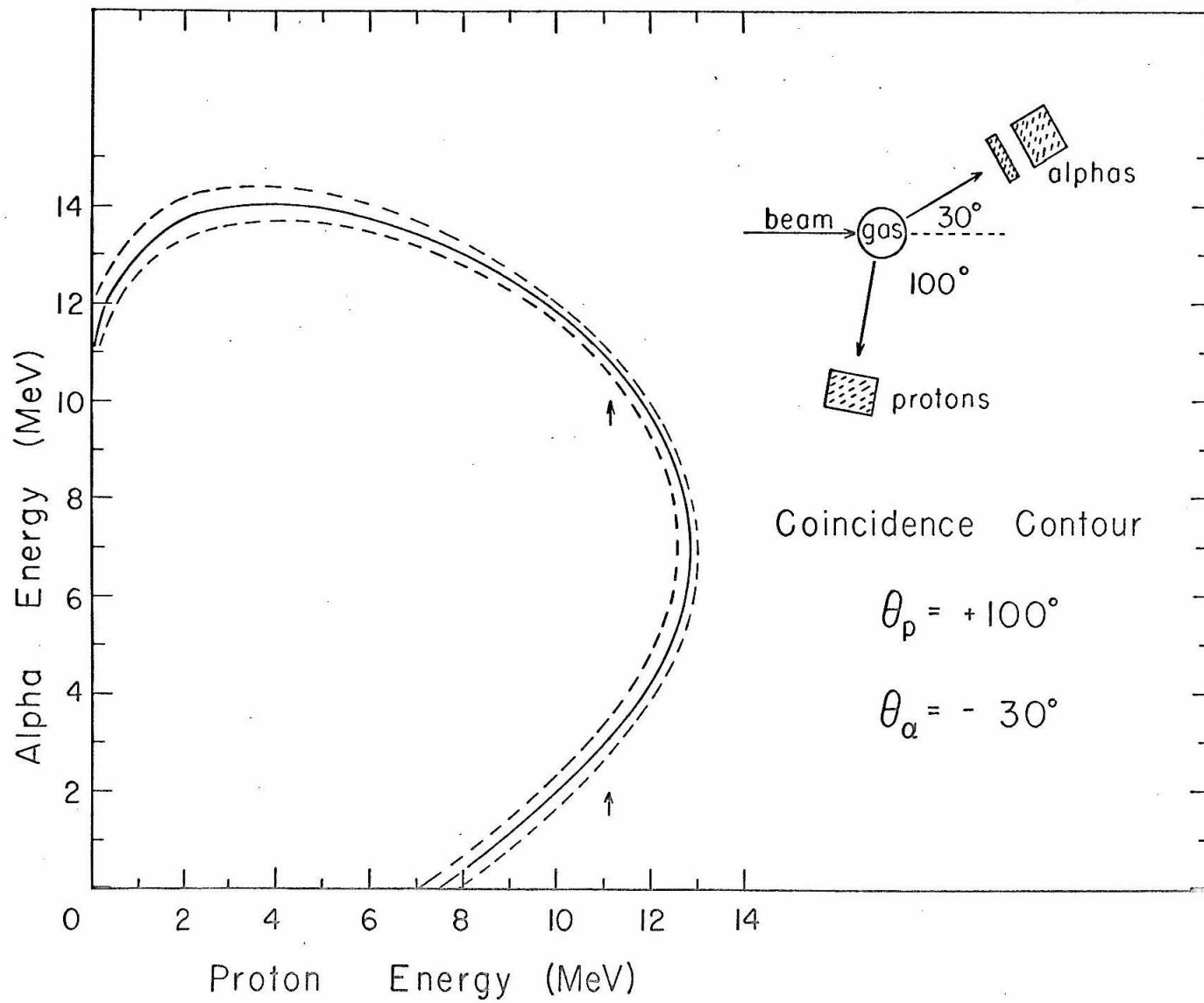


FIGURE 44

p-He⁴ Coincidence Spectrum for +100°, -30°

Proton and alpha-particle coincidences are shown at a He³ bombarding energy of 9.87 MeV for a proton angle of +100° and an alpha-particle angle of -30°. The solid curve represents the kinematically allowed energies. The points shown are the raw data including several random lines (see arrows) parallel to the proton energy axis. In the sum spectra projected on each axis the random counts (which were measured in a separate run) have been subtracted.

This particular set of angles was selected because it produced a high coincidence counting rate for the Li⁵ ground state mechanism. This is evident both in the spectrum at $E_p = 11$ MeV and $E_\alpha = 4$ MeV and 10 MeV (as was indicated in Figure 43) and in the sum spectrum for the proton yield. A large portion of the lower curve is cut off because of the energy loss of alpha particles in the gas cell foil and the inability of the telescope to distinguish between alpha particles and protons below 2 MeV.

The isolated group of coincidence counts at $E_p = 15$ MeV and $E_\alpha = 13$ MeV is due to the reaction $D(\text{He}^3, p)\text{He}^4$ from a slight deuterium contaminant in the target gas. This aided in the determination of the energy scales.

For further details see pages 58 and 59.

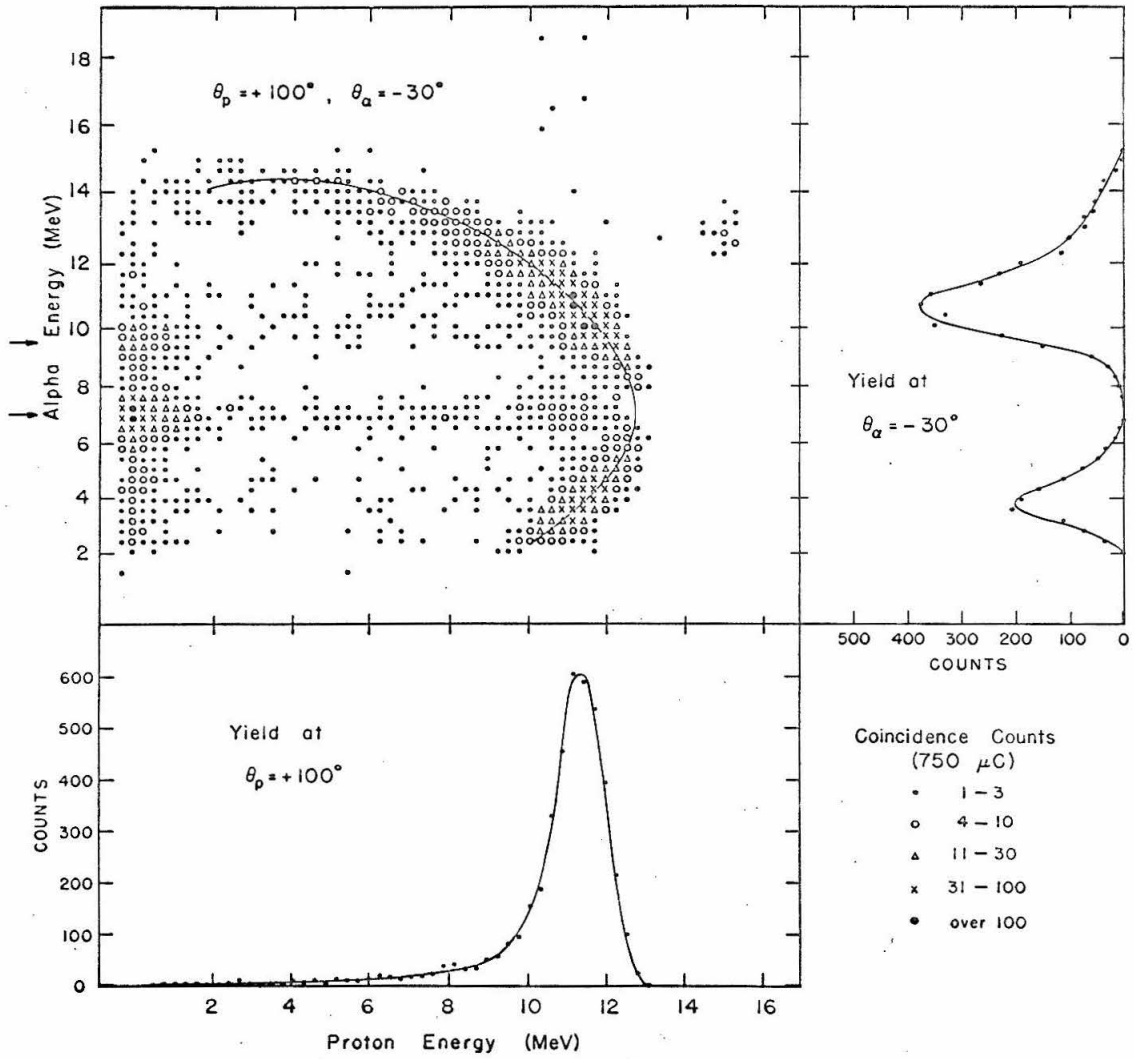


FIGURE 45

p-He⁴ Coincidence Spectrum for +90°, -40°

Proton and alpha-particle coincidences are shown at a He³ bombarding energy of 9.87 MeV for a proton angle of +90° and an alpha-particle angle of -40°. As in Figure 44 the solid line represents the locus of kinematically allowed events. The Li⁵ ground state again shows up prominently. The region near $E_p = 5$ MeV and $E_\alpha = 12$ MeV corresponds to a very low p-p relative energy - down to a few keV. The absence of counts as indicated by the dip in the proton yield is not unexpected. The p-p relative energy passes through 800 keV (corresponding to the alpha spectra peak at forward angles) at proton energies of 2.4 and 8.0 MeV and the suggestion of a rise in the proton yield at these points might indicate the presence of a slight p-p interaction even at this rather backward alpha-particle angle. The extra peak that appears in the alpha-particle yield shows the misleading effects that can be produced when one sums across a region where the allowed curve becomes perpendicular to one axis.

For further discussion see pages 59 and 60.

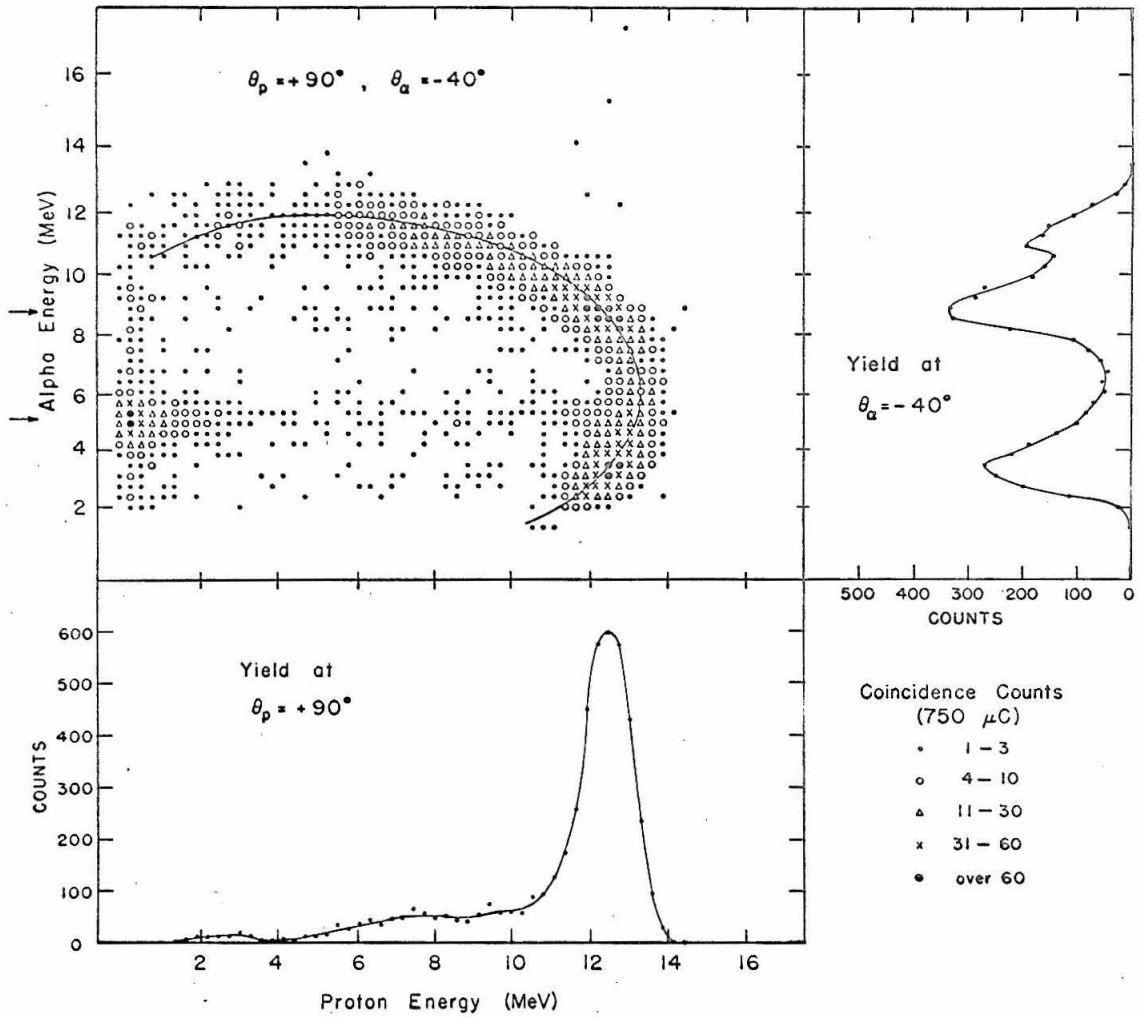


FIGURE 46

p-p Coincidence Spectrum for $+45^{\circ}$, -45°

Proton-proton coincidences are shown at a He^3 bombarding energy of 9.87 MeV for the symmetric proton angles of $+45^{\circ}$ and -45° . An additional p- He^4 curve is seen because one counter did not distinguish between protons and alpha-particles. The peaking of counts at the two ends of the p-p curve (at 4, 17 and 17, 4) corresponds to the Li^5 ground state transition. Along the entire p-p curve the p-p relative energy remains near 11 MeV so that effects due to the p-p interaction are not enhanced for this pair of angles. The p- He^4 curve also shows an indication of the Li^5 ground state transition at (4, 17) that has been shifted slightly off the p-p curve by the greater energy loss of the alpha particles in the exit foil of the gas target. For further details see pages 59 and 60.

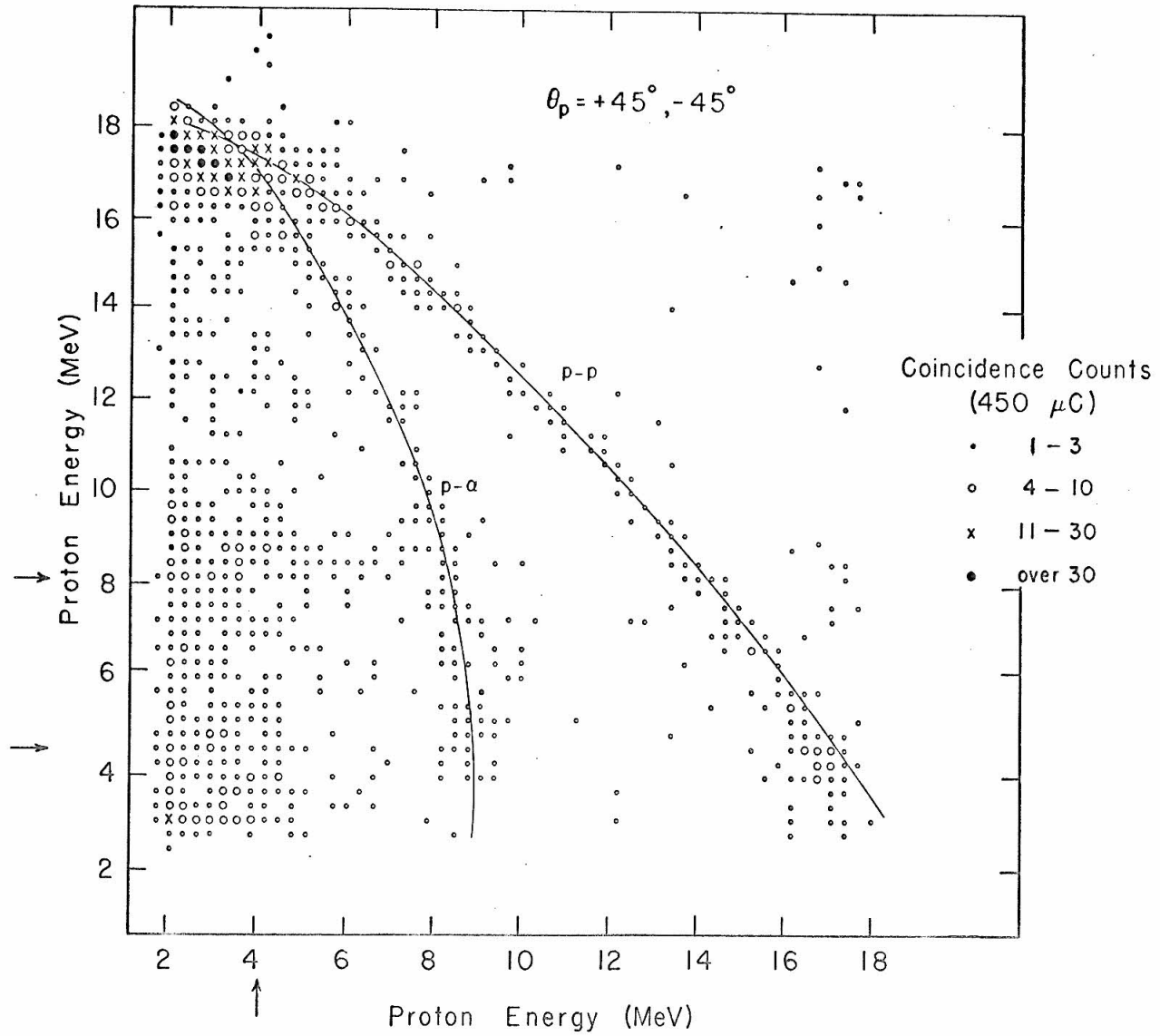


FIGURE 47

Low Energy Results for 0.98 MeV, 90°

This figure shows the unseparated energy spectrum obtained at 90° for a He³ bombarding energy of 0.98 MeV. An energy scale is given along the top of the figure. The high energy proton peak from the Li⁵ ground state mode is still evident near channel 120. Also seen are protons and alpha particles from the reaction D(He³, p)He⁴ due to a slight contaminant in the target gas. The windows shown give the total width expected for each group including the large angular resolution of the detector collimator (~ 13° fwhm). Windows are also shown for the protons and alpha particles expected from the Li⁵ recoil breakup.

Although alpha particles from the contaminant reaction wash out the lower end of the spectrum, it is clear that there is a considerable departure in the mid-energy range from the spectrum shapes that have been fitted to the high energy peak. The solid line is for an isotropic Li⁵ breakup and the dashed line for an oriented breakup ($1 - 0.875 \cos\theta_R$). Compare with the spectrum fit obtained at 2.81 MeV and 90° in Figure 15.

For further details see pages 61 and 62.

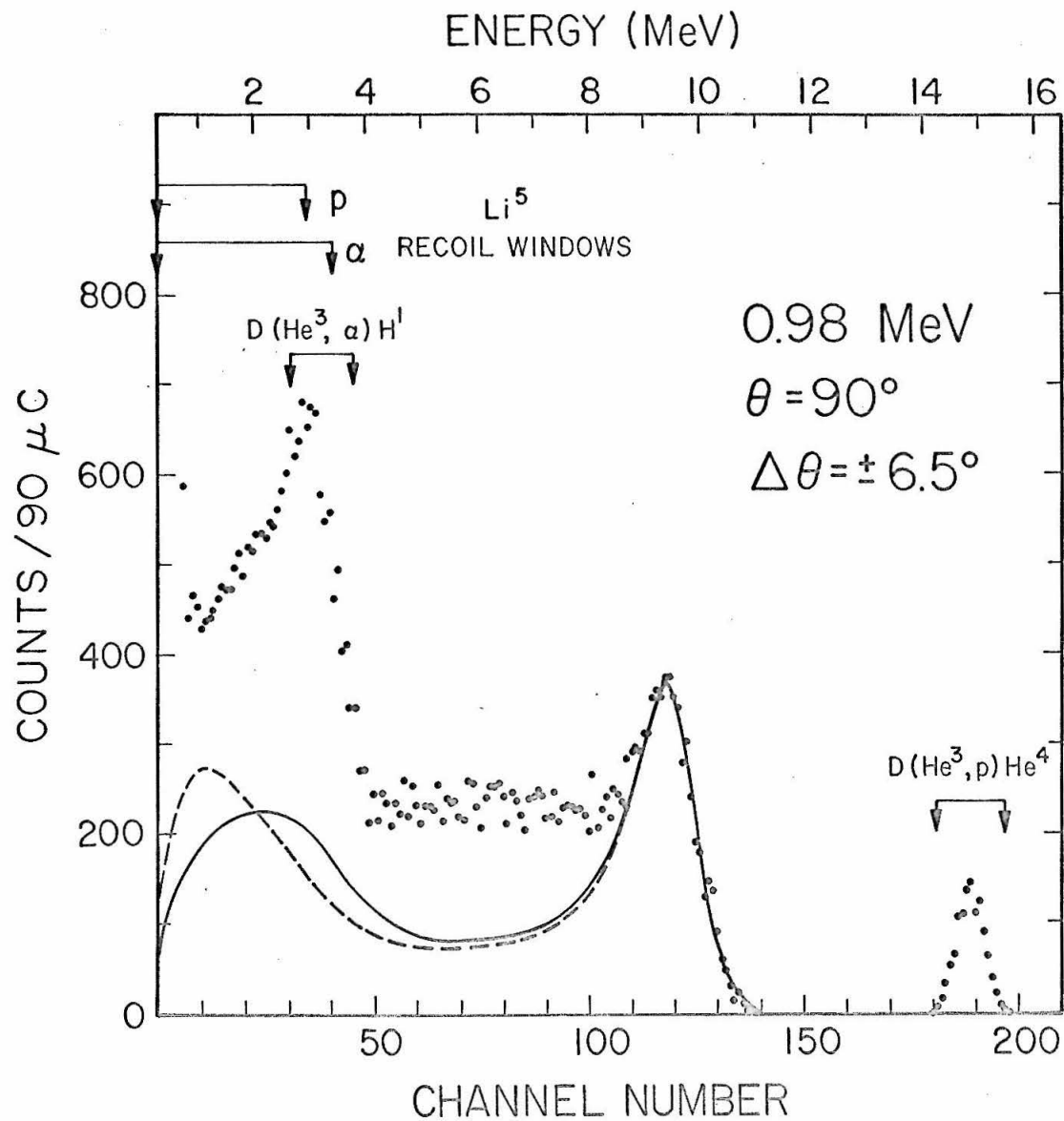


FIGURE 48
Deviation of Low Energy Spectra at 90°

This figure makes more quantitative the deviation of the calculated spectrum shape from the data at the mid-spectrum point, as seen in the previous figure. The ratio of the observed mid-spectrum height to the calculated spectrum height is plotted as a function of the He^3 bombarding energy for the isotropic Li^5 breakup (x's) and the oriented breakup (o's), where the breakup orientation is given by $(1 + \mu \cos \theta_R)$.

The oriented breakup gives the best fit at higher energies and a smooth curve has been drawn through these points. The deviation from the calculated spectra increases rapidly at the lower bombarding energies to a ratio of 3.7 at 0.64 MeV. This apparent change in the dominant reaction mechanism at low energy presumably reflects the presence of another mechanism (perhaps the $\text{He}^4 + 2p$ mode) which is not as sensitive to the various penetration effects present in the incoming $\text{He}^3 + \text{He}^3$ channel.

For further discussion see pages 61 and 62.

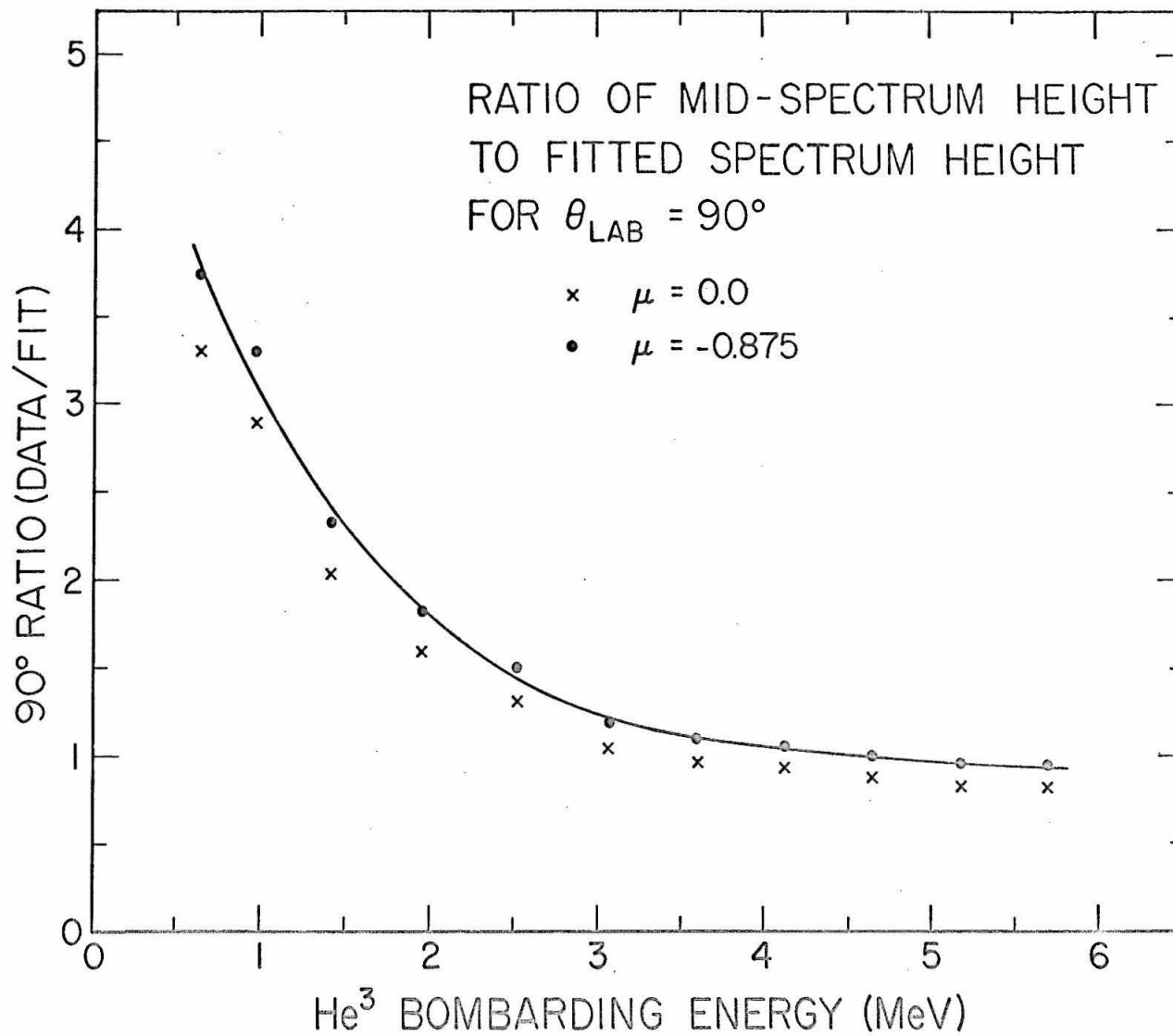


FIGURE 49
S Values for (3 + 3) Reactions

This figure shows the values of the cross-section factor, $S(E)$, for the present measurements plotted as a function of the He^3 center-of-mass energy. These are compared with the results of earlier measurements of $\text{He}^3 + \text{He}^3$ at lower energies by Good et al., (1954) and with measurements of the related reactions $\text{He}^3 + \text{T}$ by Youn et al., (1961) and $\text{T} + \text{T}$ by Jarmie and Allen (1958) and Govorov et al., (1962).

For the present work, the curve drawn through the solid dots represents values of $S(E)$, in units of MeV-barns, determined from the Li^5 spectrum fits. At energies where separated proton spectra were obtained, total cross sections were determined and the corresponding $S(E)$ values are indicated by solid triangles and a dashed curve. Above a center-of-mass energy of 1.5 MeV this involves an increase in the value of $S(E)$ of roughly 20% (see Figure 30). However, as indicated in Figure 48, below this energy the correction increases rapidly. The correction for the total yield at 90° is not as large as the mid-spectrum height deviation, but at 0.32 MeV ($E_{\text{He}^3} = 0.64 \text{ MeV}$) it is $\sim 70\%$.

For further discussion see pages 3 and 63-65.

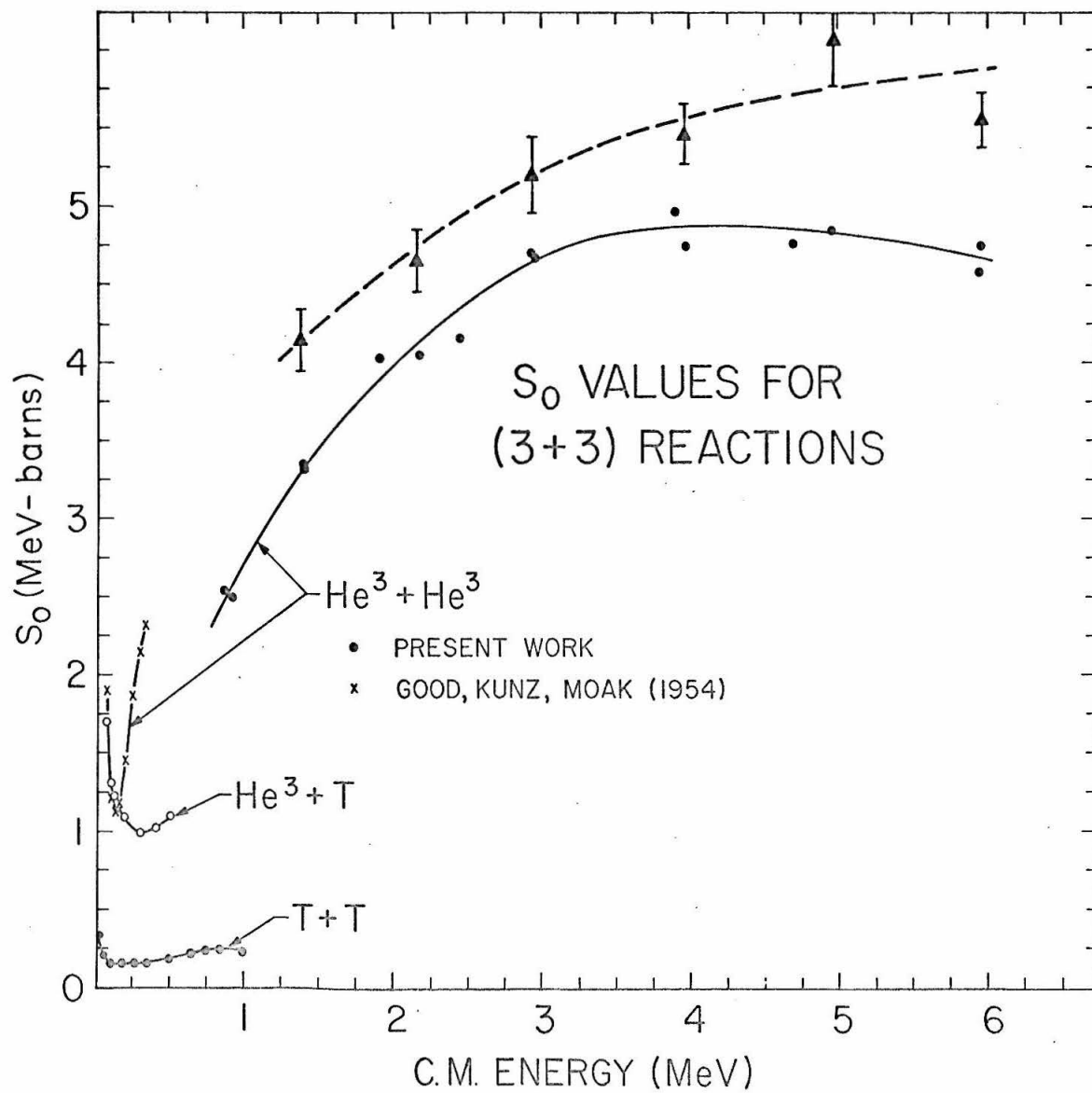


FIGURE 50

Recoil Spectrum Calculation

The top portion of this figure illustrates the velocity vector diagram used in the calculation of the secondary particle spectrum resulting from a two-stage process (see Appendix A. 3). In this case the velocity of the second proton in the laboratory system is given by the vector sum:

$$\vec{V}_L = \vec{V}_{CM} + \vec{V}_{Li^5}(Q_1) + \vec{V}_{p_2}(Q_2)$$

where \vec{V}_{CM} is the velocity of the center of mass, $\vec{V}_{Li^5}(Q_1)$ is the recoil velocity of the Li^5 , and $\vec{V}_{p_2}(Q_2)$ is the velocity of the second proton resulting from the recoil breakup. As indicated, \vec{V}_{Li^5} is a function of Q_1 , the Q-value for the first stage, and \vec{V}_{p_2} is a function of Q_2 , the excitation in the intermediate system.

The bottom portion of the figure shows the recoil proton spectrum obtained for 7.95 MeV and 20° . The two cases shown both use the spectral measure function weighting factor. The solid line includes a Coulomb interaction with $\ell_3 = 1$ between the first proton and the recoiling Li^5 , while the dashed line does not include any interaction between the first particle and the recoiling system. The horizontal lines are labeled by a number corresponding to an excitation in MeV in the $(p + He^4)$ system. They indicate the range of proton energies that are produced at $\theta_L = 20^\circ$ by the breakup in flight of the recoiling system at that excitation. The heavier line shows the region covered by the central excitation of the Li^5 ground state.

For further details see Appendix A. 3.

